Cosmology and Astrophysics from Relaxed Galaxy Clusters I: Sample Selection

Adam B. Mantz,[1,2*] Steven W. Allen,[3,4,5] R. Glenn Morris,[3,5] Robert W. Schmidt,[6]
Anja von der Linden,[3,4,7] Ondrej Urban[3,4]

[1] Department of Astronomy and Astrophysics, University of Chicago, 5640 South Ellis Avenue, Chicago, IL 60637, USA
[2] Kavli Institute for Cosmological Physics, University of Chicago, 5640 South Ellis Avenue, Chicago, IL 60637, USA
[3] Kavli Institute for Particle Astrophysics and Cosmology, Stanford University, 452 Lomita Mall, Stanford, CA 94305, USA
[4] Department of Physics, Stanford University, 382 Via Pueblo Mall, Stanford, CA 94305, USA
[5] SLAC National Accelerator Laboratory, 2575 Sand Hill Road, Menlo Park, CA 94025, USA
[6] Astronomisches Rechen-Institut, Zentrum für Astronomie der Universität Heidelberg, Mönchhofstrasse 12-14, D-69120 Heidelberg, Germany
[7] Dark Cosmology Centre, Niels Bohr Institute, University of Copenhagen, Juliane Maries Vej 30, 2100 Copenhagen, Denmark

Abstract

This is the first in a series of papers studying the astrophysics and cosmology of massive, dynamically relaxed galaxy clusters. Here we present a new, automated method for identifying relaxed clusters based on their morphologies in X-ray imaging data. While broadly similar to others in the literature, the morphological quantities that we measure are specifically designed to provide a fair basis for comparison across a range of data quality and cluster redshifts, to be robust against missing data due to point-source masks and gaps between detectors, and to avoid strong assumptions about the cosmological background and cluster masses. Based on three morphological indicators – Symmetry, Peakiness and Alignment – we develop the SPA criterion for relaxation. This analysis was applied to a large sample of cluster observations from the *Chandra* and ROSAT archives. Of the 361 clusters which received the SPA treatment, 57 (16 per cent) were subsequently found to be relaxed according to our criterion. We compare our measurements to similar estimators in the literature, as well as projected ellipticity and other image measures, and comment on trends in the relaxed cluster fraction with redshift, temperature, and survey selection method. Code implementing our morphological analysis will be made available on the web.[1]

1 Introduction

Dynamically relaxed clusters of galaxies play a special role in investigations of cluster astrophysics and cosmology. While a variety of non-equilibrium processes taking place in the intracluster medium (ICM) are of astrophysical interest, it is only in the most regular systems that the large-scale, three-dimensional properties of the ICM can be studied in detail with minimal systematic uncertainties due to projection. In addition, the masses of relaxed clusters can be estimated with high precision and minimal bias. As a result, relaxed clusters have featured in a number of prominent studies of cluster astrophysics, scaling relations and cosmology (Allen et al. 2001, 2002, 2004, 2008, Schmidt et al. 2004, Rapetti et al. 2005, 2008, Vikhlinin et al. 2005, 2006, 2009a,b, Arnaud et al. 2007, Schmidt & Allen 2007, Mantz et al. 2010a,b).

High-resolution X-ray imaging data provide a powerful tool to assess the dynamical state of the ICM. The X-rays produced by hot clusters are primarily a combination of bremsstrahlung and line emission. Because the ICM is optically thin, X-ray data carry information about the gas at all radii, albeit in projection. Furthermore, the two-body nature of bremsstrahlung emission results in local density fluctuations producing an exaggerated contrast in surface brightness. This property has enabled studies of a variety of astrophysical features in the regions of clusters where the gas density is relatively high, including shocks and cold fronts (e.g. Markevitch et al. 2000, 2002, 2005, Vikhlinin et al. 2001; see Markevitch & Vikhlinin 2007 for a review), gas sloshing (e.g. Ascasibar & Markevitch 2006, Roediger et al. 2011, ZuHone et al. 2011, Johnson et al. 2012, Simionescu et al. 2012, Paterno-Mahler et al. 2013), cavities (e.g. Fabian et al. 2000, 2003, 2006, McNamara et al. 2000, Forman et al. 2005, 2007, Hlavacek-Larrondo et al. 2012; see also reviews by McNamara et al. 2000 and Fabian 2012), and the cool, dense cores found in some clusters (e.g. Fabian et al. 1994, White et al. 1997, Peres et al. 1998, Peterson & Fabian 2006). In cluster outskirts, gas clumping (unresolved inhomogeneities) is implicated by excess X-ray brightness observed by ROSAT and *Suzaku*,

---

although the very low density and emissivity of the gas at large radii makes these observations comparably difficult (e.g. Simionescu et al. 2011, Urban et al. 2011, 2014, Walker et al. 2012a,b).

The increase in surface brightness provided by cool cores significantly biases X-ray searches in favor of finding relaxed clusters. While this is an advantage in some sense, the redshift-dependent selection bias imposed by an X-ray flux limit complicates efforts to estimate the degree of relaxation of the cluster population as a whole, and particularly its evolution with time (e.g. Vikhlinin et al. 2007, Santos et al. 2010). At redshifts $z \gtrsim 0.5$, the bulk of high-resolution X-ray observations of clusters currently target systems discovered through the Sunyaev-Zel'dovich (SZ) effect or other means (e.g. association with a quasar). Within these data sets, some clusters with cool cores have been identified (Allen et al. 2001, Siemiginowska et al. 2010, McDonald et al. 2012, Semler et al. 2012), but constructing a complete picture of relaxed systems within the evolving cluster population remains challenging.

While a number of studies have identified relaxed clusters "by eye," others have proposed quantitative measurements of image features to assess dynamical state. These generally fall into two categories: those which attempt to measure bulk asymmetry on intermediate scales (e.g. Mohr et al. 1993, Buote & Tsai 1995, Jeltema et al. 2005, Nurgaliev et al. 2013, Rasia et al. 2013), and those which attempt to assess the presence or development of a cool core (e.g. Vikhlinin et al. 2007, Santos et al. 2008, Mantz 2009, Böhringer et al. 2010).[2] Automated algorithms based on such simple measurements are inevitably limited compared to visual classification, but their reproducibility, objectivity and particularly their straightforward applicability to data sets from large follow-up programs make them appealing.

This series of papers explores what can be learned by exploiting the most massive, relaxed galaxy clusters. Subsequent papers focus on cosmological constraints from measurements of the gas mass fraction in relaxed clusters (Paper II, Mantz et al. 2014), thermodynamic profiles and scaling relations of the ICM (Paper III, Mantz et al., in prep), and the calibration of X-ray hydrostatic mass estimates using weak gravitational lensing (Paper IV, Applegate et al., in prep). Here we present a new, automatic method for identifying relaxed clusters based on X-ray imaging data, and apply it in a comprehensive search of the *Chandra* archive, in order to produce a suitable sample for this work. Our approach broadly follows others in the literature, but with particular emphasis on wide applicability (across a range in redshift and image depth), robustness against missing data (point source masks and unexposed parts of the focal plane), and independence from cosmological assumptions. For example, these considerations lead us to forgo measurements in the literature which explicitly assume the angular diameter distance to a cluster (i.e. the conversion of angle to metric distance) or the cluster mass (or a radius linked to the mass), or which involve centroids (highly dependent on the treatment of missing data).

In Section 2, we describe in detail the reduction of the *Chandra* and ROSAT X-ray data, which are also used in our subsequent papers. Section 3 provides a broad overview of our approach to measuring the X-ray morphologies of clusters, and Section 4 presents the procedure in detail. We discuss the resulting measurements, compare them to other work in the literature, and devise a criterion for relaxation in Section 5. Section 6 summarizes our findings. Where cosmological calculations are necessary, we adopt a flat ΛCDM model with Hubble parameter $H_0 = 70\,\mathrm{km\,s^{-1}\,Mpc^{-1}}$ and matter density with respect to critical $\Omega_\mathrm{m} = 0.3$.

2   Data

For this work, we analyzed data for a large sample of galaxy clusters which have archival *Chandra* observations (as of 1 February, 2013). Clusters were selected from the following sources:

1. The ROSAT Brightest Cluster Sample (BCS; Ebeling et al. 1998), with a minimum 0.1–2.4 keV luminosity of $2.5 \times 10^{44}\,\mathrm{erg\,s^{-1}}$.

2. The ROSAT-ESO Flux Limited X-ray (REFLEX) cluster sample (Böhringer et al. 2004), with the same luminosity threshold.

3. The Clusters In the Zone of Avoidance (CIZA) sample (Ebeling et al. 2002, Kocevski et al. 2007), with the same luminosity threshold.

4. The MAssive Cluster Survey (Ebeling et al. 2001, 2007, 2010).

5. The 400 Square Degree ROSAT survey (400d; Burenin et al. 2007).

6. The South Pole Telescope (SPT) SZ cluster survey (Bleem et al. 2015).

7. The cluster sample of Allen et al. (2008, hereafter A08).

---

[2]Cool cores are generally thought to correlate strongly with relaxation, although there exist notable examples of merging clusters containing remnant cool cores of gas, for example Abell 115 (Forman et al. 1981), Cygnus A (Arnaud et al. 1984), and the Bullet Cluster, 1E 0657−56 (Markevitch et al. 2002).

Our reduction of the *Chandra* data is described below in Section 2.1. The imaged field of view prohibits the use of *Chandra* data alone for morphological studies of very nearby clusters (redshifts $z \lesssim 0.05$, in practice). For a small number of clusters at low redshifts, we have therefore analyzed ROSAT Positional Sensitive Proportional Counter (PSPC) data, as described in Section 2.2. Due to the low resolution of PSPC, additional caveats apply to these results, as discussed in Section 5.6. In total, we reduced and analyzed data for 361 clusters. Tables 2 and 3 list the clusters and observations employed here.

2.1 Reduction of *Chandra* Data

We used version 4.4 of the *Chandra* software analysis suite, CIAO,[3] and version 4.4.10 of the *Chandra* calibration database, CALDB,[4] throughout this work. Subsequent changes to the calibration are not expected to significantly influence the imaging analysis presented here.

In order to ensure a uniform data reduction, and to obtain the benefits of calibration updates, all data were re-reduced to create new events files. Starting from the data products in the *Chandra* archive, the data were processed using the method outlined in the "ACIS [Advanced CCD Imaging Spectrometer] Data Preparation" *Chandra* analysis guide.[5]

The regenerated level-2 events files were screened for periods of high background by filtering their light curves using the LC_CLEAN tool. In detail, we begin by selecting a CCD to use for cleaning. Normally, this is the S1 chip for ACIS-S exposures, and the I0 or I2 chip for ACIS-I exposures. There are, however, many exceptions to this, dependent on the specific configuration of each observation. In some ACIS-S exposures the S1 chip is not active, and in these cases we use a relatively source-free area of the S3 chip where possible. For some ACIS-I exposures of low-redshift clusters, where the cluster fills some or all of the detector, we use the S2 chip.

We visually inspect the chip and mask out any sources of astrophysical emission (point sources, cluster emission, etc.), and any bad pixels, cosmic rays etc. that were not removed during the reduction phase. We then produce a light curve, using the same parameters as were used to make the *Chandra* blank-sky background data sets,[6] i.e. for front-illuminated (FI) CCDs the energy range 0.3–12 keV, and a time bin of 259.28 s; and for back-illuminated (BI) CCDs the energy range 2.5–6 keV (S1 chip) or 2.5–7 keV (S3 chip), and a time bin of 1037.12 s. (The different sets of parameters are motivated by the different sensitivities of the FI and BI chips to background flaring.)

We then apply the LC_CLEAN tool with default settings: initial mean calculated using 3σ clipping, followed by removal of intervals where the count rate is more than a factor of 1.2 different from the mean. In all cases, we visually inspected the resulting light-curves and checked that they were reasonable. The automatic clipping algorithm is sometimes misled by periods of exceptionally high background flaring. In cases like these, we manually exclude the time period corresponding to the flare, and/or manually set the initial mean to the correct quiescent level.

For every exposure, we carry out this process for at least two CCDs, and check that they give consistent results. If both FI and BI chips are active, we always examine at least one of each type. Since the BI chips have a higher sensitivity to flares, the BI good-time interval (GTI) is generally applicable to the FI chips as well, but in a few cases we use separate GTIs for the FI and BI chips. As a final safety precaution, we check that the mean level of the light curve after filtering is reasonable, since there are sometimes extended periods of high background which are difficult to detect in short exposures. These values are shown in the left panel of Figure 1, as a function of the date of the observation. Values are per-CCD, corrected for any fraction of the chip area that was excluded.

The overall trend as a function of time (high at the start of the mission, before ∼2001, then fairly flat from 2001–2003, then rising until ∼2010, then declining again) is representative of the evolution of the *Chandra* background, which is influenced by the solar cycle. In addition to this overall shape, FAINT-mode exposures tend to have a higher rate than VFAINT-mode exposures from the same epoch.

For some very extended, low-redshift clusters where there is essentially no region of the detector free from cluster emission, the rates are somewhat elevated due to cluster contamination (these are excluded from the figure). In these cases, all we can do is check that the light curve looks reasonable, and that excluding larger fractions of the chip in the direction of the cluster center reduces the normalized rate.

On the basis of these checks, we exclude a minority of obsids from further analysis, generally because they are either extensively flared or suspected to be affected by flares, and only represent a small fraction of the data that exist for the target in question (these are noted in Table 2). Finally, any non-cluster sources in the analyzed fields were masked out by visual inspection of the cleaned events files.

To account for possible variations between the blank-sky background exposures and the science exposures, we normalized the blank-sky files using the high-energy count rates, which should measure the overall level of the particle background. Specifically, we apply a multiplicative factor derived from the ratio of the 9.5–12 keV count rates in the

---

[3]`http://cxc.harvard.edu/ciao/`
[4]`http://cxc.harvard.edu/caldb/`
[5]`http://cxc.harvard.edu/ciao/guides/acis_data.html`
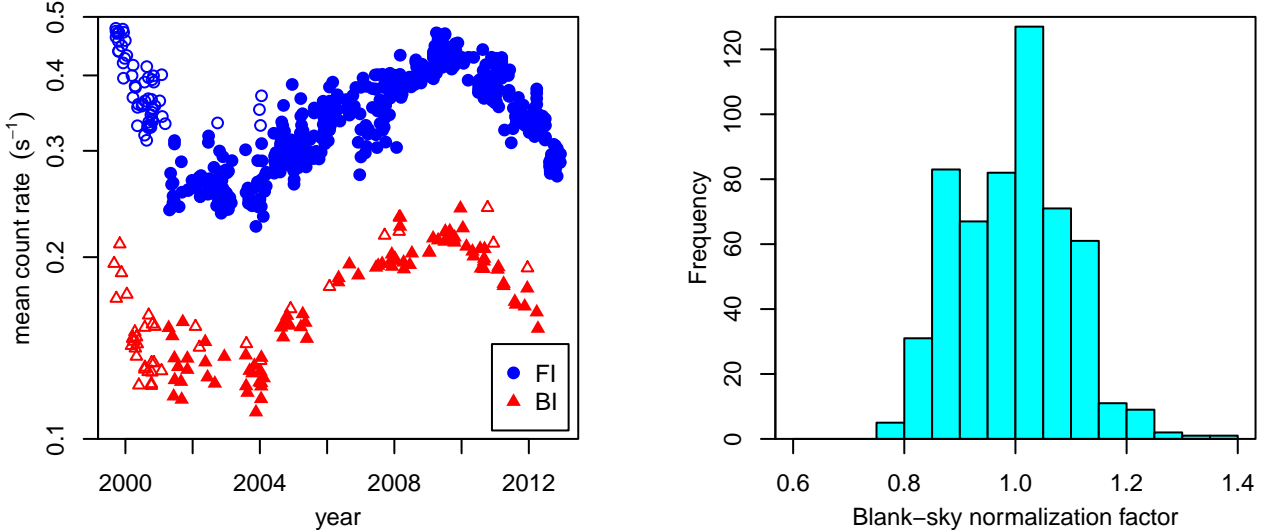[6]`http://cxc.cfa.harvard.edu/ciao/threads/acisbackground/`

Figure 1: Left: Mean background count rates after light-curve filtering for the front-illuminated (FI) and back-illuminated (BI) ACIS CCDs, in the energy bands given in the text. Filled and open symbols respectively denote observations taken in VFAINT and FAINT modes. Observations where significant cluster emission is present on all active CCDs are excluded from the plot. Assuming that source-free regions of the detector exist, strong deviations from these trends (which are dominated by the solar cycle) would indicate extended periods of high background, allowing such observations to be excluded from the analysis. Right: Histogram of blank-sky scaling factors. These factors are the ratio of the 9.5–12 keV count rates for the science events file relative to that in the blank-sky events file. There is some chip-to-chip variation in the factor; those plotted here are from S3 for ACIS-S exposures, and I0–3 for ACIS-I exposures.

science and blank-sky files. (Note that in background period A, and in a small number of science exposures, only events up to 10 keV were telemetered.) These scaling factors typically lie in the range 0.8–1.2, as shown in the right panel of Figure 1. We find some evidence for chip-to-chip, and indeed node-to-node, variations in the scaling factors, but there are no clear trends. For detailed spectral analysis in subsequent papers, we use per-CCD scaling factors; here, for our basic imaging analysis, we take the more straightforward approach of adopting a single mean scaling per observation for all FI or BI chips.

Note that in background epochs A–C, the blank-sky events files are in FAINT mode. In order to use these blank-sky files with science exposures, the science events files must also be processed in FAINT mode, i.e. the VFAINT correction cannot be applied even if available (resulting in somewhat noisier data than would otherwise be the case; see Figure 1). Such exposures are indicated by "V*" in Table 2.

2.2 Reduction of ROSAT Data

The ROSAT PSPC observations were reduced using the Extended Source Analysis Software package of Snowden et al. (1994). In short, we identify good time intervals using a master veto threshold of $170\,\mathrm{counts\,s^{-1}}$, to exclude times of anomalously high particle background rates, and a time delay of $15\,\mathrm{s}$, to remove the events at the beginning of each observation before the detector high voltage achieved its nominal level. We create light curves for each the seven standard ROSAT bands, and compute a list of nominal scattered solar X-ray (SSX) background count rates, under the assumption that the residual atmosphere along the line of sight is optically thin. The solar X-ray spectrum is modelled as a two temperature thermal plasma, with individual temperatures of $10^{5.7}\,\mathrm{K}$ and $10^{6.2}\,\mathrm{K}$. By inspecting the light curves of the SSX background count rates, we identify and exclude periods of intense SSX contamination. In the remaining time intervals, we model the X-ray background in the nominal energy bands of 0.7–0.9, 0.9–1.3 and 1.3–2.0 keV (standard ROSAT bands R5–R7), using the standard assumption that the background consists of a cosmic component, the calibrated particle background, a SSX component and a possible long-term enhancement (where required). These models are used to generate background count rate maps. Note that these background maps are not equivalent to the blank-sky maps available for *Chandra*, since they do not account for the astrophysical background; this leads to small differences in our analysis of the ROSAT images in Section 4.1.

4

3 General Approach

3.1 Preliminaries

Our procedure for characterizing the morphology of galaxy clusters, detailed in the next section, is guided by a few broad principles. (1) It should provide a fair basis to compare clusters spanning a wide range of redshift and mass, and using data of variable quality. Thus, very nearby clusters should not be penalized because we can discern detailed structure within them that would not be resolved at higher redshift. The most crucial step to achieving this is identifying comparable regions of different clusters, which is described in Section 3.2. Additionally, because the gaps between *Chandra* CCDs generally mask part of the cluster emission at redshifts $\lesssim 0.25$, we avoid the use of centroids and other quantities which assume complete images. (2) As much as possible, the algorithm should be insensitive to the prevalence of Poisson noise, to avoid unfairly penalizing clusters imaged with shallow exposures or located at high redshifts. Integral to meeting this requirement is the robust estimation of measurement uncertainties, which we address by bootstrapping the input photon images, as detailed in Section 4.1. (3) Since the main purpose of this work is to identify a relaxed cluster sample to use for cosmological studies, it is also advantageous to avoid strong assumptions about either the mass (or virial radii) of the clusters, or the background cosmology.

The particular quantities that we calculate from the cluster images are designed to measure the features on which subjective determinations of relaxation are generally based. In general terms, these are:

1. the sharpness of the peak in surface brightness.

2. the shifting of isophotes with respect to one another (i.e. the appearance of sloshing).

3. the distance between the center of symmetry on large scales (a low brightness isophote) and small scales (e.g. the cool core, if any).

Sections 4.3 and 4.4 provide more complete details of the measurements, which are carefully designed to respect the "fair comparison" requirement above. In practice, this suite of three relatively simple calculations performs well, and the close connection between the measurements and visible features aids their interpretation.

The particular thresholds for the measured values that we adopt to identify relaxed clusters are roughly placed with reference to prior, subjective decisions. Once in place, however, the thresholds are applied without regard to any subjective determinations. We assess the performance of the algorithm both by whether its decisions are subjectively reasonable, and, more pertinently, by comparing the measured intrinsic scatter of the gas mass fraction for the new relaxed sample with the subjectively identified sample of A08; this comparison was made only *after* the new sample was finalized. As described in Section 5.5, the algorithmically identified sample has a somewhat smaller intrinsic scatter than the A08 sample. Although it is beyond the scope of this work, testing our algorithm against mock X-ray images of simulated galaxy clusters can potentially provide further refinements.

3.2 Standardizing Cluster Surface Brightness

Outside of their central regions, the surface brightness profiles of galaxy clusters are approximately self-similar (e.g. Vikhlinin et al. 2006, Croston et al. 2008). This raises the possibility of identifying characteristic radii that are comparable across clusters via the surface brightness. To that end, we motivate a redshift- and temperature-dependent scaling of surface brightness based on the self-similar model of Kaiser (1986, see also Santos et al. 2008).

The average surface brightness within a circular aperture of angular radius θ, corresponding to physical radius $r = \theta \, d_{\mathrm{A}}(z)$, for a cluster with redshift z and angular diameter distance $d_{\mathrm{A}}(z)$, is

$$S = \frac{F}{\pi \theta^2} \propto \frac{K(z, T, N_{\mathrm{H}}) L}{(1+z)^4 r^2}, \tag{1}$$

where F and L are, respectively, the observer-frame flux and rest-frame bolometric luminosity of the cluster. Here the coefficient K accounts for the redshift- and temperature-dependent K-correction from bolometric flux to flux in the observed energy band, as well as any Galactic absorption (equivalent absorbing hydrogen column density, N_{H}). For self-similar profiles, this proportionality also holds for surface brightness at a given characteristic radius, r_Δ, defined in terms of the cluster mass and the critical density of the Universe; $M(< r_\Delta) = (4/3)\pi \Delta \rho_{\mathrm{cr}}(z) r_\Delta^3$. Using scalings from the Kaiser model,

$$
\begin{aligned}
L &\propto & T^2 E(z), \tag{2} \\
r_\Delta &\propto & \frac{T^{1/2}}{E(z)},
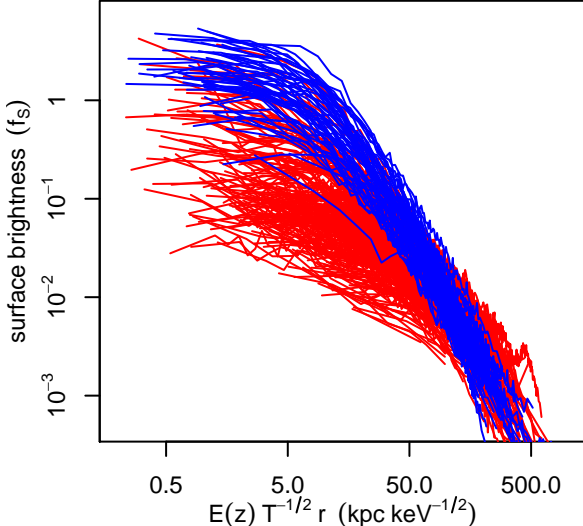\end{aligned}
$$

Figure 2: Scaled, background subtracted surface brightness profiles from our *Chandra* analysis. The scaling factors follow from the self-similar model and are given in Equations 2–3. Clusters that are ultimately categorized as relaxed in this work are shown in blue, and others in red. Measurement errors on the individual profiles are not shown (but see Figure 3).

where $E(z) = H(z)/H_0$ is the normalized Hubble parameter, we can eliminate L and r_Δ in favor of the ICM temperature, T. This yields the relation $S(r_\Delta) \propto f_S$, with

$$f_S \equiv K(z, T, N_{\mathrm{H}}) \frac{E(z)^3}{(1+z)^4} \left(\frac{kT}{\mathrm{keV}} \right) \; \mathrm{photons\,Ms^{-1}\,cm^{-2}\,(0.984\,arcsec)^{-2}}, \tag{3}$$

where we have assigned units which are convenient for the analysis of *Chandra* data (see Section 4.1). Following the argument above, surface brightness levels corresponding to constant multiples of f_S should correspond to approximately the same values of Δ across all clusters, provided they fall in the self-similar part of the profile.

With this rescaling, it becomes possible to identify approximately corresponding regions of clusters with different masses and redshifts, without explicitly assuming the angular diameter distance to each or a prescription for estimating some scale radius r_Δ (equivalently M_Δ). There is an implicit assumption of cosmological parameters necessary to evaluate $E(z)$, but this sensitivity is relatively mild. As input, we need only the redshifts of clusters, column densities for their positions on the sky, and rough temperature estimates for them.[7]

As an a posteriori check of how reasonable this scaling is, Figure 3.2 shows surface brightness profiles from our analysis of *Chandra* data (Section 4.2). The surface brightness values are background-subtracted and shown in units of f_S, and the radial coordinate is scaled by $E(z)/\sqrt{T}$ according to Equation 2.[8] The intrinsic scatter among profiles is significant at small radii, tightening to a self-similar profile at large radii. The clusters that are ultimately identified as relaxed in this work form a particularly tight locus.

4 Procedure

This section describes in detail our procedure for measuring morphological indicators and their uncertainties.

4.1 Data Preparation and Bootstrapping

For the *Chandra* observations, images in the 0.6–2.0 keV band are extracted from both the cleaned science and blank-sky event files, and are binned by a factor of two (obtaining ≈ 1 arcsec resolution). An appropriate exposure map is generated for the same energy range. Off-chip pixels and pixels contaminated by point sources are flagged in the science images. These files, along with the blank-sky normalization factor and its statistical error, serve as input to our morphological algorithm.

All the steps described below are performed on 1000 bootstrap realizations of each observation. We bootstrap the science and blank-sky images at the level of individual counts; that is, the pixel locations of each detected photon in the original image are listed (with repetition, as appropriate), and photons are added to pixels of the bootstrap image by sampling from this list with replacement. For each bootstrap iteration, we also sample a new value of the blank-sky normalization factor, based on its statistical uncertainty.

---

[7] Approximate temperatures are sufficient, since the product $K(z, T, N_{\mathrm{H}}) kT \approx T^{1/2}$ (for temperatures characteristic of the clusters in our data set, for which there is negligible line emission at soft energies) varies slowly with kT.

[8] Note that the conversion of angular to metric distance introduces an additional cosmology-dependent factor of $d_{\mathrm{A}}(z)$ in the radial coordinates.

To estimate statistical signal-to-noise throughout the analysis, we keep track of the variance in various quantities, beginning with the counts in the images. We assign the statistical variance $N+1$ to each pixel of the science and blank-sky images, where N is the number of counts in the corresponding pixel. This choice is motivated by the fact that the Bayesian posterior for the average number of counts in an equal-length exposure, based on the observed counts N, has variance $N+1$;[9] furthermore, it neatly avoids the pathological assignment of zero uncertainty to pixels with zero counts. Note that our final uncertainties are entirely characterized by the bootstrap procedure; the error maps described here only provide approximate signal-to-noise estimates for, e.g., the surface brightness profile fitting and adaptive smoothing steps below.

The blank-sky image is rescaled according to the normalization factor and subtracted from the science image (recall that each of these ingredients is bootstrapped), propagating the variance of the background-subtracted image straightforwardly. The result is divided by the exposure map, assuming no uncertainty in the latter, to create a flat-fielded image. At this stage, it is possible to straightforwardly combine images from multiple observations of a cluster by the same telescope. Finally, we convert the brightness images to intensity in units of photons $\text{Ms}^{-1}\,\text{cm}^{-2}\,(0.984\,\text{arcsec})^{-2}$.[10]

For ROSAT observations, our procedure differs in a few details. The ROSAT images cover the 0.7–2.0 keV energy band and have the native PSPC resolution of 14.9 arcsec. Since there are no blank-sky fields, we subtract the ROSAT particle background rate maps from the images after converting the latter to count rates but before flat fielding (since the particle background is not vignetted). A spatially constant residual background level, accounting for unresolved astrophysical sources, is fit and subtracted at a later stage (see Section 4.2).

4.2 Center Finding and Surface Brightness Profiling

A global center for each cluster is defined by computing the median photon location in an iteratively shrinking aperture. Beginning with the entire image, the center is defined as $(\tilde{x}, \tilde{y})$, where $\tilde{x}$ ($\tilde{y}$) is calculated by summing the image over columns (rows), shifting the resulting one-dimensional array to be non-negative, and computing the median of the resulting discrete function of x (y). A new image is extracted, centered on $(\tilde{x}, \tilde{y})$ but with dimensions smaller by a factor of 2/3 (or more if the edge of the image is encountered), and the procedure is repeated until a minimum aperture size of 40 pixels square has been reached and the center is static.

In practice, this median center compromises between two widely used alternatives, the brightest pixel and the centroid. In clusters having a cool core that is offset from the center of emission on larger scales, the median center tends to be located within the cool core, although not necessarily at its center or brightest point. Like the centroid, it does respond to a degree to the weight of emission in the fainter regions of the cluster. However, the median center is much less biased by the presence of masked regions than the centroid, to the extent that "filling in" masked regions and gaps between detectors is generally unnecessary. Compared to simply choosing the brightest pixel, the median procedure has the clear advantage that it is less susceptible to Poisson noise or mistakenly unmasked point-source emission.

An azimuthally averaged surface brightness profile about the median center is calculated in annuli which are adaptively chosen to provide a signal-to-noise ratio > 2 (with a single, signal-to-noise < 2 annulus covering the largest imaged radii). A β model (Cavaliere & Fusco-Femiano 1976) plus constant background level are then fitted to the radially outermost half of the profile,[11] and the best-fitting constant is subtracted from the image and surface brightness profile. When brightness levels are compared to the surface brightness profile in the following sections, we compare to the measured profile at radii where it was constrained with the target signal-to-noise, and to the β model at larger radii. Similarly, when random values are drawn to be consistent with the profile at a given radius, we scatter them according to the measurement uncertainty for the appropriate annulus, or the outermost annulus in the case of extrapolation.

Following the argument in Section 3.2, we define a set of characteristic surface brightness levels in our adopted units,

$$S_j = 0.002 \times 10^{0.28j} f_S, \tag{4}$$

where $j = 0, 1, \ldots, 5$. The number of levels and the range in surface brightness that they span were chosen empirically to provide good performance for the measurement of our morphological estimates (described in the following subsections) over a wide range of data quality and cluster redshifts. These scaled surface brightness levels are shown

---

[9] More specifically, $N+1$ is the variance when the prior is chosen to be a flat Gamma distribution such that the posterior is maximized at N (shape parameter $k = 1$ and rate parameter $\beta = 0$).

[10] The particular choice of units here is purely for convenience, as it makes the intensity of a typical cluster center of order unity, and simplifies the case of 2×2 binned *Chandra* images.

[11] Blindly fitting the outermost half of the profiles works well in general for *Chandra* data, where the blank-sky background subtraction is typically approximately correct. Given the adaptive binning of the profile, the outer half tends to span the power-law tail of the cluster and any residual foreground/background, e.g. Galactic contamination which is not included in the blank-sky maps. In rare cases where the residual constant term has very high signal-to-noise (so that the outer half of the adaptively binned profile excludes too much of the cluster), we manually choose the radial range of the profile to use in this step.
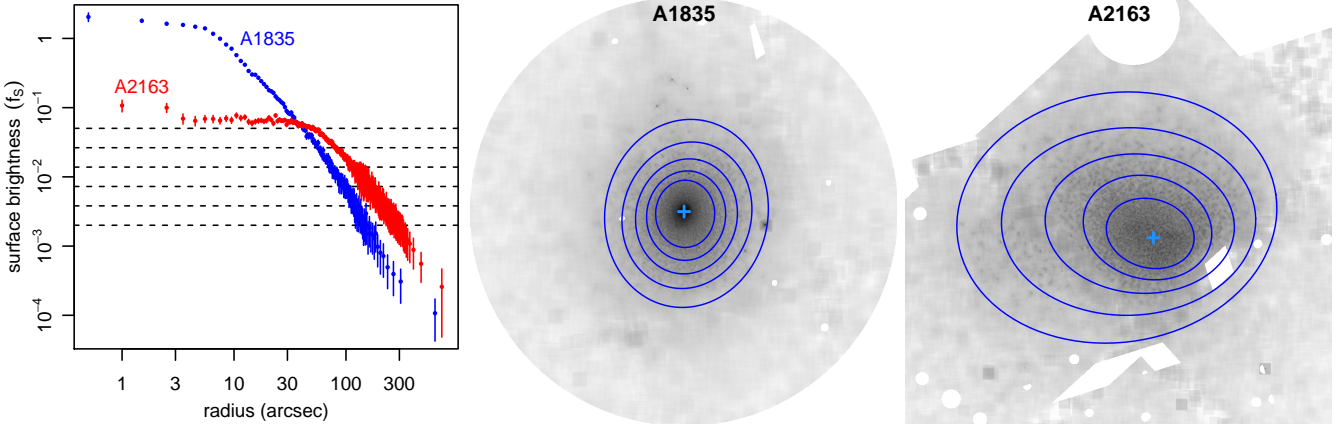
Figure 3: Left: Surface brightness profiles for Abell 1835 and Abell 2163, scaled according to Equation 3. Dashed lines correspond to the brightness levels defined in Equation 4 (the lowest level corresponds to $j = 0$). Our peakiness metric depends on the average surface brightness in a circular aperture whose radius is given by the intersection of the observed profile with the highest level ($j = 5$). Center and right: Smoothed images of the same clusters, logarithmically scaled. Crosses show the global centers determined in Section 4.2. Also shown are the ellipses fit to each of five isophotes, defined as the ranges between the surface brightness levels given in Equation 4. The alignment metric reflects how close the centers of these ellipses lie to one another, while the symmetry metric reflects how well they agree with the global center. These clusters exemplify very relaxed (Abell 1835) and very unrelaxed (Abell 2163) morphologies, according to all three quantities.

along with example profiles for Abell 1835 (which has a cool, bright core) and Abell 2163 (which has a flat core) in the left panel of Figure 3.

4.3 Surface Brightness Peakiness

The presence of a core of bright, relatively cool, X-ray emitting gas in the center of a cluster is a common signature of dynamically relaxed systems (Fabian et al. 1994, Peterson & Fabian 2006). The formation of these features is expected, and to some extent observed, to be disrupted by major mergers (Burns et al. 2008, Henning et al. 2009, Million et al. 2010, Rossetti et al. 2011, Skory et al. 2013, Ichinohe et al. 2014). Thus, while cool cores are not necessarily completely destroyed by major mergers once formed, requiring the presence of a core should provide an efficient way to reject unrelaxed clusters.

Although measuring a temperature decrement in the center of a cluster is relatively involved, detecting the presence of a central brightness enhancement is straightforward. Consequently, simple measurements of the sharpness of the peak in surface brightness at cluster centers have been widely employed as a proxy for the presence of cool cores. Various measurements of peak strength have been introduced. Vikhlinin et al. (2007) used the logarithmic slope of the gas density profile at a radius of $0.04\,r_{500}$. Santos et al. (2008) advocate using the ratio of fluxes contained in two metric apertures; flux ratios in apertures linked to r_{500} have also been employed (e.g. Mantz 2009, Böhringer et al. 2010).

For the present work, the explicit reliance of each of these approaches on metric distances (i.e. on an assumed angular diameter distance) or scale radii (r_{500}) is a disadvantage. Instead, we introduce a measurement which relies only on the scaled surface brightness profile in the region where it is typically very well constrained, as follows. First, we determine the angular radius, θ_5, where the measured surface brightness profile is equal to S_5, as defined in the previous section; if the profile never exceeds this value, then the radius bounding the innermost bin of the surface brightness profile is used. We then calculate the average surface brightness at distances $\leq \theta_5$ from the global center of Section 4.2 in units of f_S, assigning to each masked pixel in this region a random value based on the surface brightness profile and its uncertainty at the appropriate radius. (This calculation is statistically equivalent to taking the area-weighted average of the surface brightness profile at radii $\leq \theta_5$.)

This average, scaled central surface brightness, $\bar{S}(\theta \leq \theta_5)/f_S$, shows an overall downward trend with redshift across the data set, as seen in Figure 4.3. This is expected; qualitatively similar trends have been reported in measurements of surface brightness "concentration" (Santos et al. 2008; see also Santos et al. 2010, McDonald et al. 2013), which our measurements are closely related to (see Section 5.1). Physically, this increase of brightness with time, particularly at the high central brightness end, presumably corresponds to non-self-similar evolution in the development of cool cores in relaxed clusters. Since our procedure is intended to select morphologically relaxed clusters at any redshift, we include a redshift weighting, which in the absence of precise predictions from
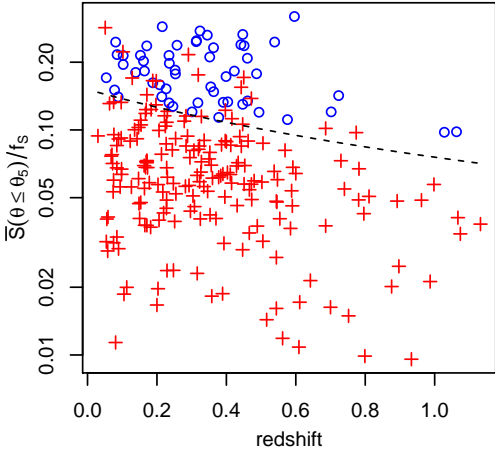
Figure 4: Average central surface brightness in scaled units as a function of redshift from our *Chandra* analysis. Clusters that we ultimately classify as relaxed (Section 5.4) are shown as blue circles, and others as red crosses. A net decreasing trend can be seen, qualitatively in agreement with observations based on similar surface brightness measurements (Santos et al. 2008, 2010, McDonald et al. 2013). Our peakiness measure incorporates a $1 + z$ weighting to approximately compensate for this evolution in core brightness; the dashed line corresponds to the constant-peakiness threshold used to define the relaxed sample in Section 5.4.

hydrodynamical simulations, we assume to be linear.[12] Taking the logarithm for convenience, the surface brightness peakiness, p, is thus defined as

$$p = \log_{10}\left[(1 + z)\frac{\bar{S}(\theta \leq \theta_5)}{f_S}\right]. \tag{5}$$

To the extent that cluster surface brightness profiles are self-similar at radii greater than θ_5, this quantity contains as much information as the ratio of flux in small and large apertures, while being measured more precisely. The particular value of S_5 (Equation 4) was chosen for exactly this purpose; the divergence of the surface brightness profiles of Abell 1835 (bright core) and Abell 2163 (non-bright core) at radii $< \theta_5$ seen in Figure 3 is typical (see also Figure 3.2). A more extreme contrast can be seen in Figure 5, which compares the clusters with the lowest and highest values of p from our analysis.

4.4 Elliptical Isophote Fitting and Statistics

Our other morphological measurements aim to quantify the two-dimensional structure of clusters. Here again we avoid algorithms which assume complete imaging coverage, such as the centroid variance (Mohr et al. 1993) and various other measures of substructure and asymmetry (e.g. Nurgaliev et al. 2013, Rasia et al. 2013), as masked point sources or the gaps between adjacent CCDs often impinge on cluster images in practice. (Indeed, Figures 3, 5, 7 and 13 all provide examples of this.)

Instead, our approach fits elliptical shapes to the 5 isophotes defined by the brightness levels in Equation 4. This analysis does not use the "filled-in" image introduced in Section 4.3, since azimuthal symmetry is assumed in the production of those images. Instead, to reduce Poisson noise, we apply an adaptive boxcar smoothing algorithm to the original flat-fielded image, with a maximum kernel radius of 10 pixels and target signal-to-noise of two, enforcing that pixels masked in the original image remain masked in the final product. To prevent very distant pixels with large noise fluctuations from influencing our results, these smoothed images are cropped beyond the radius corresponding to $0.1S_0$. We then identify pixels in the smoothed image with values in each of the 5 brightness ranges (isophotes) $S_j < S < S_{j+1}$. An elliptical shape is fit to each of these isophotes, where the fit minimizes the sum of absolute distances from the ellipse to each pixel in the isophote along the line passing through the pixel and the ellipse center.

To automatically catch cases where the ellipse fit is suspect, we compute the following two quantities. The first, f_{el}, is straightforwardly the fraction of the ellipse which falls on unmasked pixels; this is useful for identifying cases where the ellipse fit should not be trusted because most of the true azimuthal extent of the isophote was not imaged. The second quantity is $\Gamma_{\mathrm{el}} = \langle e^{i\phi} \rangle$, where ϕ is the angle between the major axis of the ellipse and a ray from the ellipse center to a given pixel, and the average is over pixels in the corresponding isophote. This statistic measures how balanced the distribution of isophote pixels is with respect to the fitted ellipse center, and efficiently finds cases where the best-fitting ellipse simply passes as closely as possible to a very non-elliptical distribution of pixels.[13] For a given isophote and bootstrap iteration, if $f_{\mathrm{el}} < 0.5$ or either the real or imaginary part of Γ_{el} has magnitude > 0.4,

---

[12]We have not attempted to fine-tune the redshift dependence further, since the motivation for doing so is questionable and since it would provide an opportunity to tailor the high-redshift content of our final relaxed sample (potentially biasing the cosmological results of Paper II). However, a posteriori, it is interesting to note that the $1 + z$ weighting results in an approximately constant fraction of peaky clusters with redshift (Section 5.9), seemingly in good agreement with the constant cool-core fraction predicted from simulations (Burns et al. 2008). This is encouraging, as it suggests we are selecting dynamically similar clusters at each redshift.

[13]Note that Γ_{el} is similar to the displacement between the ellipse center and the isophote centroid, under the assumption that all pixels in the isophote have exactly the same brightness.

9
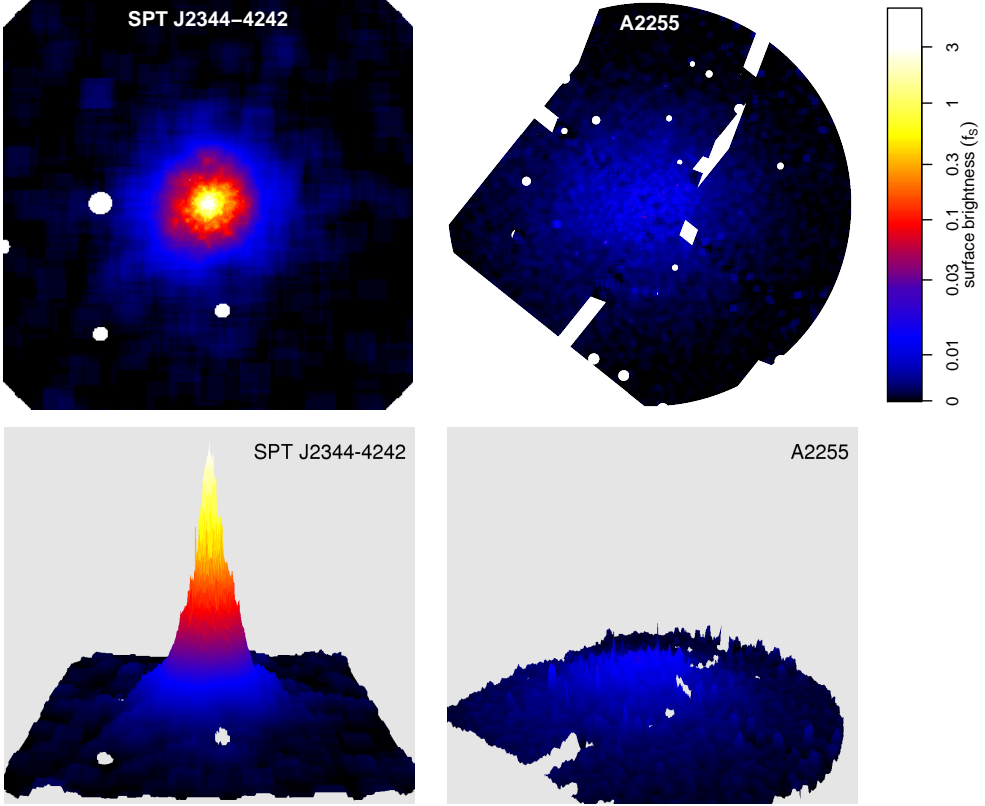
Figure 5: The most and least peaky clusters in our *Chandra* sample: SPT J2344−4242 ($p = -0.29$; left column) and Abell 2255 ($p = -1.91$; right column). The top row shows the adaptively smoothed images, scaled according to Equation 3, used in our isophote analysis (Section 4.4), and the bottom row shows the same images as 3-dimensional surfaces to emphasize the contrast in central brightness. The vertical direction in the bottom row, and the colors throughout, use a common logarithmic scaling.

the fit is considered to have failed, and the isophote is discarded. In addition, no fit is attempted for isophotes where the lower end of the brightness range lies in the outer portion of the surface brightness profile (where the target signal-to-noise was not achieved), for isophotes where the upper end of the brightness range is greater than the central point in the surface brightness profile, or for isophotes consisting of < 100 pixels. For an isophote to contribute to the final set of statistics for a cluster, we require it to be successfully fit in $> 3/4$ of bootstrap iterations.

In Paper II, mass profiles are derived for a sample of 40 relaxed clusters identified in the present work. Histograms of the mean of the semi-major and semi-minor axes in units of r_{2500} are shown for these clusters in Figure 4.4. As expected, the isophotes in units of f_S broadly map onto comparable radii in units of r_{2500}.

From this set of ellipses, we calculate two statistics, which we refer to as alignment, a, and symmetry, s. These are defined to have the same sense as the peakiness, i.e. more positive (negative) values being typical of more (less) relaxed clusters.

The alignment is defined as

$$a = -\log_{10} \left[\frac{1}{N_{\mathrm{el}} - 1} \sum_{j=1}^{N_{\mathrm{el}}-1} \frac{\delta_{j,j+1}}{\langle b \rangle_{j,j+1}} \right], \qquad (6)$$

where N_{el} is the number of ellipses and the sum is over pairs of "adjacent" ellipses, i.e. those corresponding to progressively higher surface brightness. Here $\delta_{j,j+1}$ is the distance between the centers of two ellipses, and $\langle b \rangle_{j,j+1}$ is the average of the four ellipse axis lengths (major and minor axes of both ellipses).

The symmetry statistic is

$$s = -\log_{10} \left[\frac{1}{N_{\mathrm{el}}} \sum_{j=1}^{N_{\mathrm{el}}} \frac{\delta_{j,\mathrm{c}}}{\langle b \rangle_j} \right], \qquad (7)$$

where $\delta_{j,\mathrm{c}}$ is the distance between the center of the jth ellipse and the global center identified in Section 4.2, and $\langle b \rangle_j$ is the average of the major and minor axes of the ellipse.
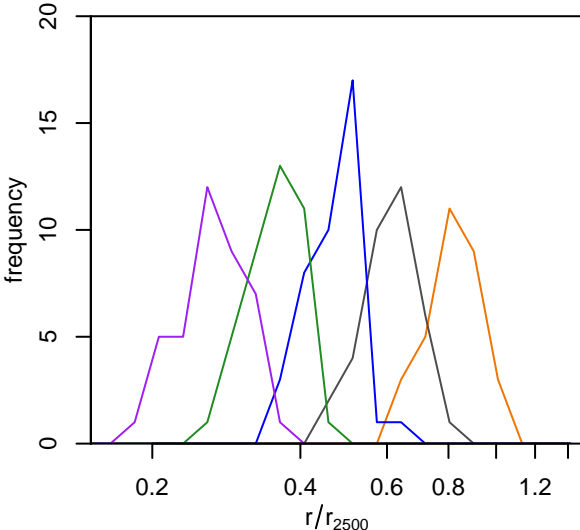
Figure 6: Histograms of the average of the semi-major and semi-minor axes of ellipses corresponding to the five isophotes used in our analysis, as a fraction of r_{2500} (shown as lines, for clarity). Only 40 clusters which are classified as highly relaxed here and for which we can reliably determined mass profiles (hence r_{2500}; see Paper II) are used here. The cluster region used in our isophote analysis typically spans radii $0.2 \lesssim r/r_{2500} \lesssim 1$.
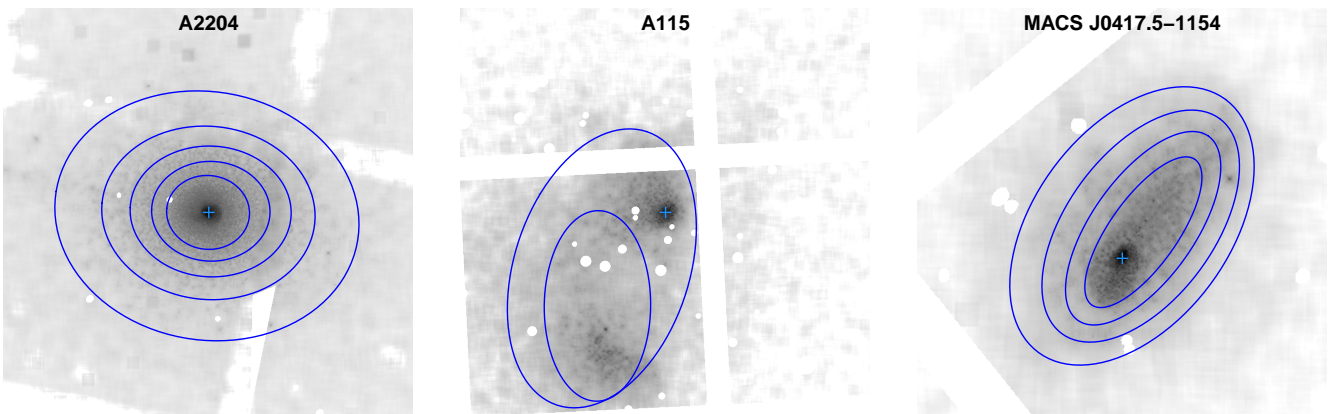
Figure 7: Left, center: Smoothed images of clusters representing the extremes of symmetry from our *Chandra* analysis, with elliptical isophote fits superimposed. The clusters also represent extremes in alignment, as these quantities are strongly correlated in practice (Figure 8). The left panel shows Abell 2204 ($s = 1.64$, $a = 1.55$), and the center panel shows Abell 115 ($s = -0.04$, $a = 0.45$). In Abell 115, the low symmetry value is due to the strong disagreement between the ellipse centers and the global center (blue cross), which is located in the cool core of one of the merging sub-clusters. The low alignment value follows from the disagreement of the ellipse centers with one another. Note that the ellipses shown correspond to isophotes that truly are (roughly) elliptical in shape (the $j = 0$–1 and 1–2 isophotes in Equation 4). The three brighter isophotes are disjoint, containing well separated groupings of pixels in the two X-ray bright clumps; our algorithm flags them as being non-elliptical and excludes them from the analysis. The right panel shows MACS J0417.5−1154, a good example of a merging cluster that has acceptable alignment but poor symmetry.

These quantities provide complementary measurements of cluster substructure. The alignment is sensitive to shifts in the center of emission at the relatively large scales probed by our set of isophotes, whereas the symmetry parameter measures the overall agreement of those isophotes with the global center. Note that, by design, the brightness range covered by this analysis does not extend to the brightest (spatially central) regions of cool core clusters (left panel of Figure 3), where complex, non-elliptical features such as cavities and small-scale sloshing are ubiquitous, even in more globally relaxed clusters. Figure 3 shows smoothed images and isophote ellipse fits to the unmodified (i.e. not bootstrapped) data for the example clusters A1835 and A2163, which respectively have relatively high and low values of both alignment and symmetry. Clusters representing even more extreme values of a and s are on display in Figure 7.

Table 1: Abridged results of our morphological analysis. The remaining clusters can be found in Table 4. [1] Catalog that each cluster was drawn from, abbreviating the BCS, REFLEX, CIZA, MACS, 400d and SPT catalogs, or none of the above (⋆). A ⋆ appended to a catalog identifier means that the cluster can be found in the indicated sample, but does not satisfy the X-ray luminosity threshold normally applied in Section 2. [2] Cluster name. Prefixes that are implied by column [1] have been suppressed. [3] Observatory used to produce the listed results, either *Chandra* (C) or ROSAT (R). [4] Flags indicating whether a cluster is part of the A08 (a), CLASH relaxed (c), LoCuSS low centroid variance (l), or CCCP low central entropy (p) samples (see Sections 5.5–5.7). An *f* indicates that the cluster is used in Paper II. [5–7] Symmetry, peakiness and alignment measurements. Note that some or all may be missing, dependent on data quality (see Section 5). In general, when the data were inadequate to measure *s* and *a*, we did not carry through the bootstrapping procedure to obtain uncertainties on *p*. [8] Indicates whether the cluster is relaxed according to the SPA criterion introduced in Section 5.4. [9] Mean ellipticity of the isophotes employed in our analysis. [10–11] J2000 coordinates of the global center measured from the X-ray analysis (without bootstrapping). [12–13] J2000 coordinates of the BCG identified in Section 5.2.

Cat.	Name	Obs.	flags	s	p	a	Rel.	ellip.	RA_X	Dec_X	RA_{BCG}	Dec_{BCG}
B	Abell 1068	C		1.050 ± 0.033	-0.688 ± 0.019	1.51 ± 0.07	√	0.256 ± 0.013	160.1859	39.9531	160.1854	39.9531
B	Abell 1132	C		1.034 ± 0.217	-1.369 ± 0.064	1.25 ± 0.15		0.192 ± 0.027	164.6091	56.7950	164.5986	56.7949
B	Abell 115	C	p	-0.040 ± 0.029	-0.810 ± 0.023	0.45 ± 0.08		0.406 ± 0.019	13.9598	26.4098	13.9609	26.4104
B	Abell 1201	C		0.488 ± 0.032	-1.074 ± 0.019	1.08 ± 0.10		0.505 ± 0.019	168.2264	13.4351	168.2271	13.4358
B	Abell 1204	C		1.171 ± 0.073	-0.558 ± 0.024	1.20 ± 0.09	√	0.194 ± 0.020	168.3354	17.5945	168.3354	17.5947
B	Abell 1246	C			-1.390				170.9906	21.4810	170.9947	21.4794
B	Abell 1413	C	a	1.333 ± 0.050	-0.981 ± 0.007	1.71 ± 0.08		0.307 ± 0.005	178.8247	23.4050	178.8250	23.4049
B	Abell 1423	C	c	0.900 ± 0.116	-1.024 ± 0.026	0.85 ± 0.16		0.231 ± 0.032	179.3217	33.6112	179.3222	33.6109
B	Abell 1553	C		0.621 ± 0.097	-1.357 ± 0.314	0.81 ± 0.17		0.146 ± 0.027	187.6972	10.5530	187.7036	10.5464
B	Abell 1682	C			-1.421				196.7088	46.5579	196.6904	46.5585
B	Abell 1758	C			-1.733				203.1737	50.5472	203.1601	50.5599
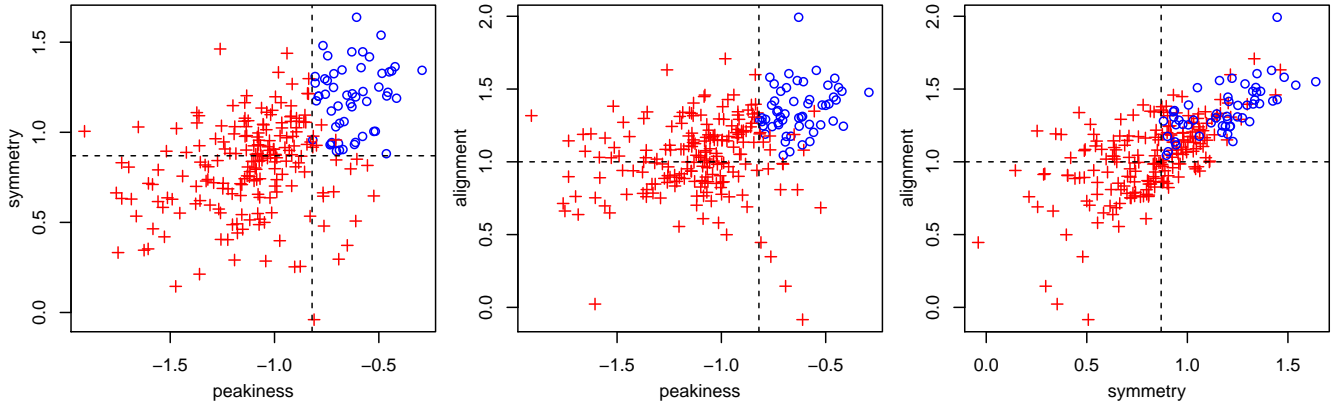
Figure 8: Distributions of measured morphological values from our *Chandra* analysis, with the *s*-*p*-*a* cuts defining the relaxed sub-sample shown as dashed lines. Clusters in this relaxed sub-sample (identified with a √ symbol in Tables 1 and 4) are shown as blue circles, and others as red crosses. To be considered relaxed a cluster must simultaneously pass all three cuts at > 50 per cent confidence (see Section 5.4).

5 Results

The procedure of Section 4 was applied to obtain morphological statistics from 1000 bootstrap simulations of the clusters identified in Section 2. Results are tabulated in Tables 1 and 4. For the *Chandra* sample, these are also shown in Figure 8.

We note that there are cases where our morphology code fails outright. For example, for flat-core (low *p*) clusters in very shallow images, we are sometimes unable to constrain even two isophote ellipses, which is necessary for the calculation of alignment; however, in these cases, it is generally still possible to measure peakiness. The great majority of these can be classified as unrelaxed according to the criterion introduced in Section 5.4 based solely on peakiness. In yet lower signal-to-noise data, it is sometimes impossible to obtain meaningful constraints on the surface brightness profile, and thus even peakiness cannot be measured. Subjectively speaking, this small minority of clusters appears unambiguously unrelaxed, and we classify them as such.

Note that there is a strong correlation between symmetry and alignment (Figure 8), by virtue of their similar definitions in terms of isophote properties. Somewhat weaker correlations exists between symmetry or alignment on
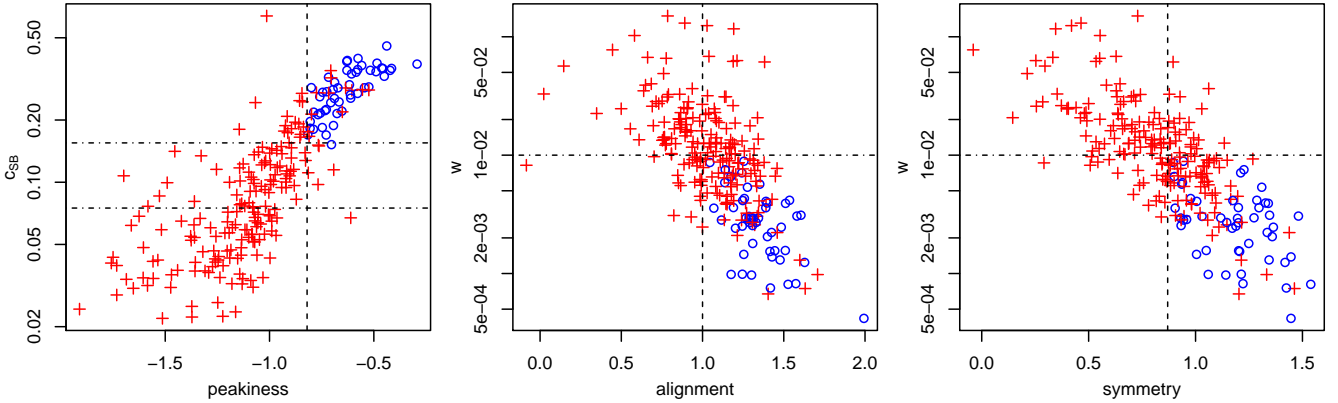
Figure 9: Comparison of our morphology statistics (peakiness, alignment, symmetry) from *Chandra* data with surface brightness concentration (c_{SB}) and centroid shift (w). Clusters that we classify as relaxed in Section 5.4 are shown as blue circles, and others as red crosses. As expected, our peakiness metric correlates with c_{SB} and both alignment and symmetry anti-correlate with the centroid shift. Dot-dashed lines show the c_{SB} thresholds defining "moderate" and "strong" cool cores in the work of Santos et al. (2008) and the w cut used by Böhringer et al. (2010) to distinguish relaxed systems, while dashed lines show the thresholds we adopt in Section 5.4. (The latter were determined without reference to either c_{SB} or w.)

one hand and peakiness on the other; these presumably reflect the role of mergers in either destroying or preventing the formation of cool cores.

5.1 Comparison with Other X-ray Morphology Statistics

To provide some context, we now compare our morphological statistics to typical estimators used in the literature. Specifically, we have chosen the surface brightness concentration parameter of Santos et al. (2008) and the centroid variance (Mohr et al. 1993), defined by

$$
\begin{aligned}
c_{SB} &= \frac{F(r < 40\,\mathrm{kpc})}{F(r < 400\,\mathrm{kpc})}, \\
w^2 &= \frac{1}{r_{500}^2}\mathrm{Var}(\Delta),
\end{aligned}
\tag{8}
$$

where we estimate r_{500} from the temperature–mass relation of Mantz et al. (2010b). The distances Δ are calculated between our global centers and the centroids of emission in our "filled-in" images within apertures of radius $(0.1j)r_{500}$ ($j = 1, 2, \ldots, 10$) about the global centers. We additionally compute the power ratio P_3/P_0 (Buote & Tsai 1995), again using the filled-in images.

We compare our morphological statistics to these alternatives in Figure 9. Not surprisingly, peakiness correlates most strongly with c_{SB},[14] while both alignment and symmetry anti-correlate strongly with centroid variance. The power ratio correlates less well with our statistics. While there are important differences, it is clear that our statistics measure similar image features to these other quantities. In fact, the cuts in s, p and a that we use to define a relaxed sample in Section 5.4, which were determined before we had even calculated c_{SB} and w, correspond surprisingly well to the cuts used by Santos et al. (2008) and Böhringer et al. (2010) to define strong cool cores and low centroid variance, respectively. Note, however, that our final selection appears to be somewhat more conservative than these cuts on c_{SB} and w would be, as one might generically expect given the use of a third, non-degenerate measurement in our selection.

5.2 Comparison with BCG/X-ray Offsets

A simple metric that has been used to try to distinguish between relaxed and unrelaxed clusters is the distance in projection between the center of the X-ray emission and the location of the brightest cluster galaxy (BCG). This approach is potentially appealing because in principle the X-ray data need not be deep enough to provide peakiness measurements, let alone the more challenging alignment and symmetry measurements. This may be the case for, e.g., X-ray snapshots of distant SZ- or IR-selected clusters, whose X-ray brightness is not well known prior to the

---

[14]Consequently, we can also conclude that peakiness correlates with other cool-core indicators, such as central cooling time, which have been observed to correlate with c_{SB} (Santos et al. 2008).
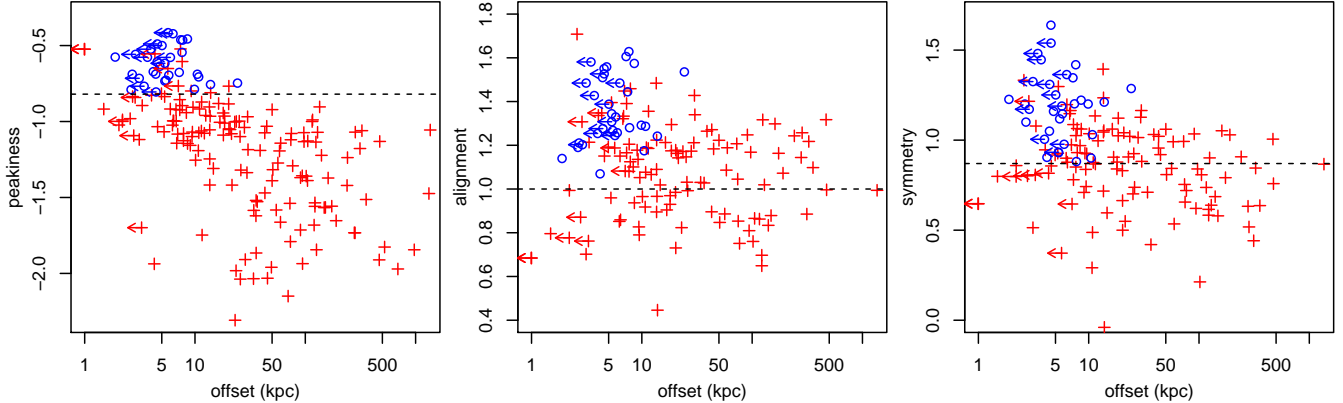
Figure 10: Comparison of our morphology statistics (peakiness, alignment, symmetry) from *Chandra* data with the projected offset in kpc between our measure of the global X-ray center and the location of the brightest cluster galaxy. Clusters that we classify as relaxed in Section 5.4 are shown as blue circles, and others as red crosses (dashed lines show the cuts associated with this classification). Arrows label offsets which are $< 1''$ in projection, i.e. below the resolution of our X-ray images (distances in kpc for these are calculated assuming $1''$ offsets). The BCG offsets are visibly correlated with peakiness, which is intuitive, since both measurements are most sensitive to activity in the cluster center.

observations. At the same time, optical or IR imaging is still commonly used to confirm the presence of a galaxy overdensity at the location of a candidate cluster, and to study the properties of cluster galaxies, and so a BCG identification may be readily available.

Where available, we use the BCGs identified in the Weighing the Giants project (54 clusters; von der Linden et al. 2014) or for the SPT survey (18 clusters in common with our sample; Song et al. 2012). For the remaining clusters, we query the DR7 and DR10 catalog and imaging databases of the Sloan Digital Sky Survey[15] (SDSS; Abazajian et al. 2009, Ahn et al. 2014), which provides BCGs for an additional 123 clusters. The clusters considered here span a wide redshift range, and several are known to have central galaxies bluer than the red sequence (e.g. Crawford et al. 1999), making simple algorithmic identification schemes difficult to implement. We therefore verify each BCG candidate by eye, considering galaxies up to 1 Mpc from the X-ray center. For each cluster, the initial BCG candidates are taken as the brightest objects likely to be elliptical galaxies (in the SDSS GALAXIES catalog, with concentration $R_{90}/R_{50} > 2.3$, and where a de Vaucouleur profile is a better fit than an exponential) within two apertures (50 kpc and 500 kpc) from the X-ray center. For 73 clusters, the two apertures select the same galaxy; in 69 clusters, it also passes visual verification (in the remaining 4 clusters the initial candidate is a foreground galaxy). For 38 clusters, the two apertures select different BCG candidates; in 21 (17) clusters, we select the candidate within 50 kpc (500 kpc). For 12 clusters, the BCG is not one of these two candidates for a variety of reasons (e.g. nearby BCGs are de-blended into several detections). In total, this yields 195 BCG positions.

Figure 10 shows the projected distance between these BCG locations and the global X-ray centers defined in Section 4.2 versus the corresponding measurements of X-ray symmetry, peakiness and alignment. Note that a large fraction of the < 10 kpc offsets translate to $< 1''$ in angular distance (i.e. less than the resolution of our X-ray images), and so are uncertain in detail. (Conversely, offsets > 10 kpc are resolved, i.e. $> 1''$, for the entire data set.) Nevertheless, there is a clear correlation between the BCG/X-ray offset and peakiness, while in contrast there is not such a pronounced trend between the offset and either alignment or symmetry. This makes physical sense, since merger activity generically should produce BCG/X-ray offsets as well as a reduction in peakiness at some level. At the same time, while the offsets for clusters that we ultimately classify as morphologically relaxed (Section 5.4) are generally small, there is a range in offsets, reaching 24 kpc in the most extreme case.[16] This scatter has a natural explanation in sloshing of the ICM due to merger events; the small-scale displacement of the ICM from the precise center of the gravitational potential may persist for Gyr, even as the effect on X-ray emission on the larger scales probed by the symmetry and alignment measurements is muted (ZuHone et al. 2011).

Based on the distributions in Figure 10, it is not clear that measurements of the BCG offset contribute much in addition to the full set of X-ray morphological measurements, particularly peakiness. On the other hand, given BCG locations and relatively poor X-ray data – sufficient to find an X-ray center, but not to measure even peakiness, e.g. from a shallow survey – a suitable cut on the BCG offset clearly would eliminate a large fraction of unrelaxed

---

[15]Querying both databases is advantageous since bright galaxies are masked in the DR10 catalog processing.

[16]The relaxed cluster with the largest BCG/X-ray offset (24 kpc) is MACS J1311.0−0311. This cluster fails the additional cuts required for inclusion in our cosmology sample, although for reasons of data quality rather than morphology (Paper II). The other relaxed clusters all have BCG/X-ray offsets < 14 kpc.
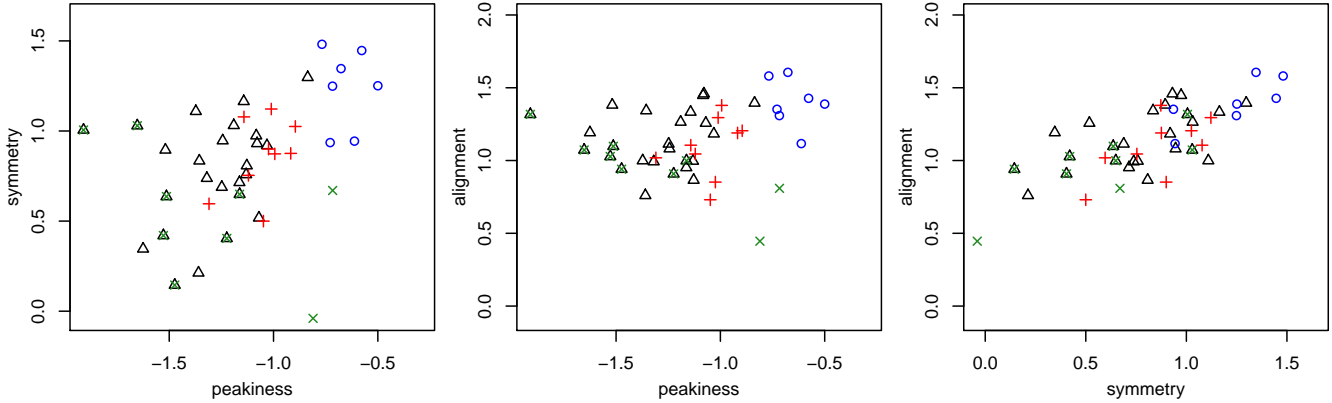
Figure 11: As Figure 8, but showing only a subset of clusters. Those with radio halos listed in the compilations of Feretti et al. (2012) or Cassano et al. (2013), all of which we identify as unrelaxed based on their X-ray morphology, are shown as black triangles. Clusters for which Cassano et al. (2013) list strong upper limits on the radio halo power are shown as red crosses (unrelaxed) or blue circles (relaxed). Green × symbols indicate clusters with radio relics compiled by Feretti et al. (2012). Our findings are consistent with radio halos and relics occurring exclusively in morphologically unrelaxed clusters.

clusters.

5.3 Comparison with Radio Halo/Relic Samples

Radio halos, low surface brightness synchrotron emission located in the central regions of clusters, have been associated with merging activity, although not all merging clusters display radio halos (see Feretti et al. 2012 and references therein). Figure 11 shows our morphological measurements for clusters with detected radio halos (Feretti et al. 2012, Cassano et al. 2013). Also shown are clusters for which strong upper limits have been placed on the radio power without detecting a halo (Cassano et al. 2013). The radio halo clusters are uniformly unrelaxed according to our X-ray morphological analysis (Section 5.4), while the clusters with only upper limits split between being relaxed and unrelaxed. These trends are consistent with previous work comparing the incidence of radio halos with other morphological estimators, namely power ratios, surface brightness concentration and/or centroid variance (Buote 2001, Cassano et al. 2010). Similarly, all the clusters in our analysis which host radio relics (emission localized to cluster outskirts) according to the compilation of Feretti et al. (2012) are found to be unrelaxed.

5.4 The SPA Criterion for Relaxation

An interesting extension of this work would be to test our morphological statistics against the actual dynamical state of simulated clusters using mock X-ray images, as in Böhringer et al. (2010) and Meneghetti et al. (2014), although we note that overcooling in simulations has historically limited the applicability of this approach. For the moment, we are concerned only with selecting the most morphologically relaxed group of clusters, rather than clusters that meet a specific criterion in terms of non-thermal support. We therefore use the subjective determinations of A08 as a broad guide for identifying the ranges of p, a and s corresponding to the most relaxed clusters. Note that the A08 selection, though subjective, has previously survived "double-blind" tests; i.e., the same clusters were independently selected as the most relaxed by multiple viewers, with cluster identities hidden. The advantage of this work is that it provides a practical and evenhanded way to compare a large number of clusters, putting the A08 selection in a wider context.

Figure 12 shows the distribution of peakiness, alignment and symmetry for the large sample of analyzed clusters as purple '×' symbols, with clusters from A08 shown as green triangles. Clearly, the morphological statistics introduced above are related to the subjective determinations used by A08. At the same time, within the context of the large, homogeneously analyzed sample, it is clear that not all of the A08 clusters belong to a well defined locus in the most relaxed corner of parameter space. Introducing cuts based on our morphology measurements may thus produce a more rigorously defined relaxed sample.

Motivated by the distributions in Figure 12, we introduce the Symmetry-Peakiness-Alignment (SPA) criterion for cluster relaxation. Namely, we define simple cuts in these three parameters, as depicted in Figure 8: $s > 0.87$, $p > -0.82$, and $a > 1.00$ (Figure 8).[17] We categorize a cluster as relaxed if > 50 per cent of the s-p-a triplets from

---

[17]A posteriori, these cuts appear well matched to thresholds in surface brightness concentration and centroid variance, respectively
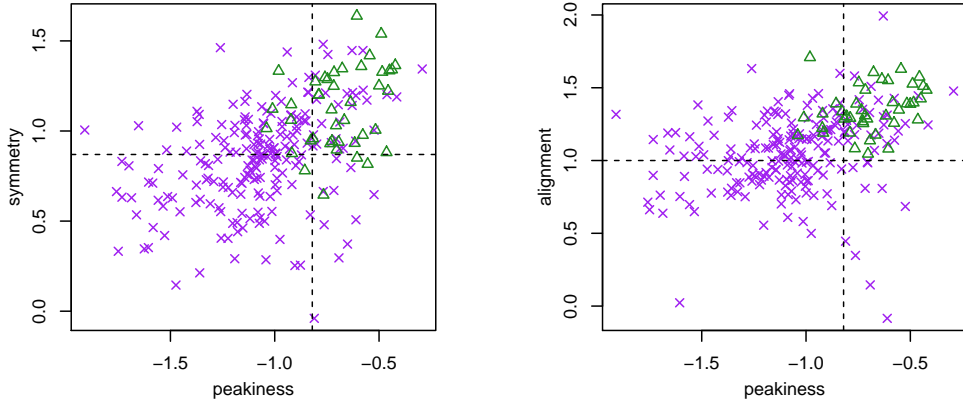
Figure 12: Peakiness–symmetry and peakiness–alignment distributions from our *Chandra* analysis. Clusters used in A08 are shown as green triangles, and others as purple ×s. Our criterion for relaxation is motivated by but more strict than (in terms of these quantities) the subjective determinations of A08. To be classified relaxed, a cluster must simultaneously exceed thresholds in all three quantities (dashed lines) at > 50 per cent confidence (see Section 5.4).

the cluster's bootstrap analysis simultaneously satisfy all three of these cuts.[18] Table 1 lists whether each cluster was classified as relaxed. Our intent is to generate a *conservative* (i.e. as pure as possible) sample of relaxed clusters, even at the expense of excluding some legitimately relaxed systems; however, for convenience, we will use the term "unrelaxed" to refer to clusters that do not meet the SPA criterion. We compare the resulting selection to similarly motivated samples in the literature in Sections 5.5 and 5.7, below.

Figure 13 shows the SPA cuts in relation to the bootstrap confidence regions associated with three example clusters, Abell 1413, MACS J0744.8+3927 and RX J0331.1−2100, along with smoothed images. Each of these clusters is classified as unrelaxed due to only one of the SPA criteria (i.e., each would be classified as relaxed if only two of the cuts were applied to the bootstrap distributions). Specifically, the emission from Abell 1413 is very regular, but not strongly peaked; MACS J0744.8+3927 has a strong peak and acceptable alignment, but fails the symmetry requirement; and RX J0331.1−2100 has acceptable peakiness and symmetry, but low alignment.

5.5 Differences from the A08 Sample

One motivation for this work is to identify a relaxed cluster sample to be used for cosmological studies of the gas mass fraction, as in A08 and Paper II. The cosmological sample must meet additional criteria to those discussed here, regarding the cluster temperature and data quality (see Paper II for details). Nevertheless, we note here the differences between the two cosmology samples which are due to morphological considerations. Specifically, Abell 1795, Abell 1413, Abell 963, Abell 2390, Abell 611, Zw 3146, Abell 2537, MACS J0329.7−0212, MACS J0744.9+3927, MS 1137.5+6625, and CL J1226.9+3332 were used in A08 but are excluded from the sample used in Paper II (henceforth SPA$_c$) by the present analysis. (This analysis adds an equal number of clusters to the SPA$_c$ sample, on the basis of data taken since 2008.) A gallery of clusters in the SPA$_c$ sample appears in Figure 14.

The intrinsic scatter in cluster gas mass fractions, f_{gas}, is a useful metric for determining the effect of our more stringent morphological criteria compared to A08. To the extent that dynamical state is the main difference between the SPA$_c$ and A08 samples, the intrinsic scatter in f_{gas} can be interpreted as a surrogate for scatter in non-thermal support, since other systematics affecting the f_{gas} measurements should be roughly equivalent across the two samples. We use the gas mass fraction measured in a spherical shell at radii $0.8 < r/r_{2500} < 1.2$, as discussed in detail in Paper II, and compare the intrinsic scatter of f_{gas} for the SPA$_c$ sample to that of SPA$_c$ plus the clusters which were included in A08 but are classified as unrelaxed on morphological grounds in this work. Marginalizing over a complete model, including cosmological terms appropriate for non-flat ΛCDM models and various astrophysical and calibration nuisance parameters (see Paper II), yields intrinsic scatters of 7.4 ± 2.3 and 13.5 ± 2.4 per cent for these two samples. We conclude that adopting the more stringent selection criteria motivated by our morphological analysis results in a quantitatively more relaxed cluster sample. The smaller intrinsic scatter of the SPA$_c$ sample

---

used by Santos et al. (2008) and Böhringer et al. (2010), as noted in Section 5.1.

[18]There is a straightforward degeneracy between the location of the cuts themselves and the fraction of passing bootstrap samples required for to be classified as relaxed. While essentially the same selection could be obtained with an ostensibly stricter threshold (given slightly shifted cuts), the 50 per cent threshold is convenient because it makes plots of the bootstrap mean for each cluster simpler to interpret (e.g. Figures 8–12). Note, however, that this 50 per cent criterion is not identical to only requiring the bootstrap mean to satisfy all three cuts, even assuming a symmetric bootstrap distribution.
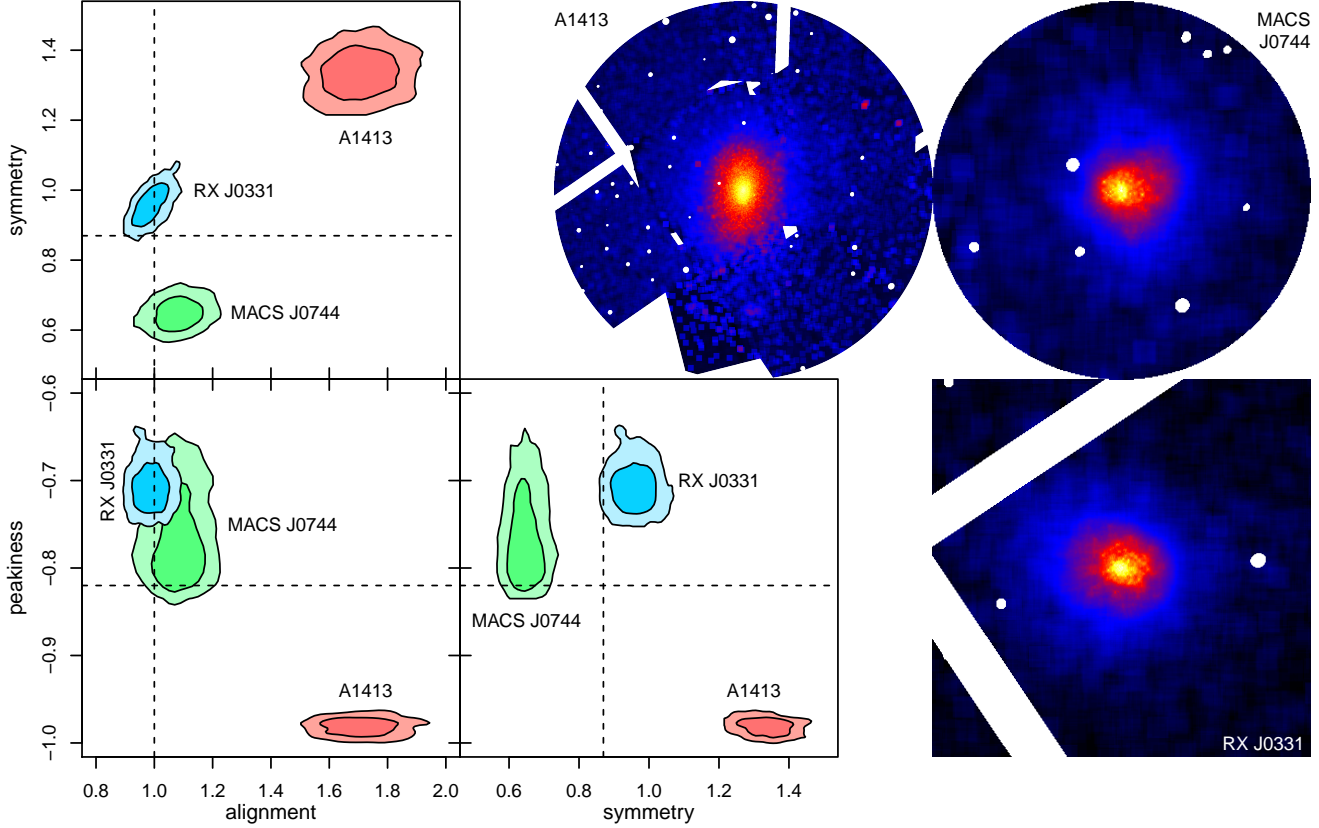
Figure 13: Left triangle: 68.3 and 95.4 per cent confidence regions of our morphological statistics for Abell 1413, MACS J0744.8+3927 and RX J0331.1−2100 from the bootstrap analysis. Dashed lines show the cut applied to each statistic to identify relaxed clusters: clusters are classified as relaxed only if > 50 per cent of their bootstrap samples exceed the cuts on all three quantities (i.e. relaxed clusters must reside in the upper-right quadrant of all panels). Right triangle: Smoothed images of the three clusters. Each of these clusters is classified as unrelaxed due to (only) one of the morphological indicators: Abell 1413 due to peakiness, MACS J0744.8+3927 due to symmetry and RX J0331.1−2100 due to alignment. Note that the color scaling is chosen independently for each image to maximize the dynamic range shown, unlike Figures 5 and 14.

translates directly into tighter cosmological constraints on dark energy parameters (Paper II). Note that this check was performed a posteriori, and did not influence the construction of the $\mathrm{SPA_c}$ sample itself.

5.6 Caveats Regarding ROSAT Observations

Image resolution potentially affects many stages of our morphology analysis. Low resolution generically results in flatter surface brightness peaks, rounder isophotes, and a diminished sensitivity to structure that would otherwise influence the global center and isophote centers. These limitations should be kept in mind when interpreting our results based on ROSAT PSPC data, although their effect should be negligible for the largest, most nearby clusters such as Perseus and Coma.

For 17 clusters spanning redshifts $0.04 < z < 0.1$, we directly compared the SPA values obtained from ROSAT and *Chandra*. As expected, the peakiness values from ROSAT are lower, although only by $\sim 0.04 \pm 0.03$ (mean and intrinsic scatter). Alignment and symmetry values are higher by 0.08 ± 0.23 and 0.11 ± 0.18, respectively. Somewhat surprisingly, there is no clear trend with redshift over the range probed (i.e. as a function of how well resolved the clusters are), although in the cases of alignment and symmetry a trend could easily be lost in the scatter.

Among the 24 clusters for which we only use ROSAT data, only three are classified as relaxed: Abell 133, Abell 780 and Perseus. Each of these meets the SPA criteria with sufficient margin that the above scatter should not affect this determination.
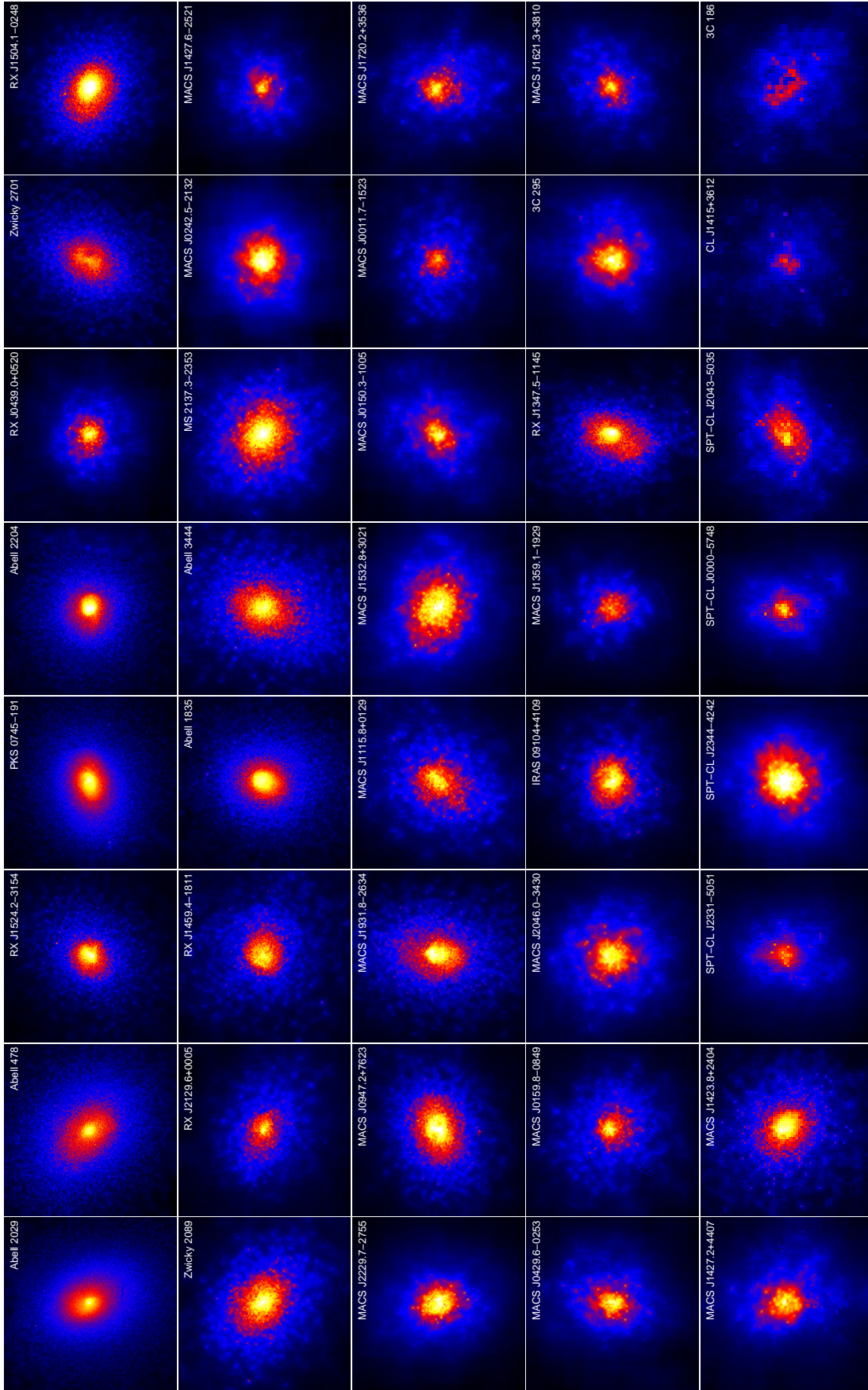
Figure 14: Smoothed, flat-fielded images of clusters satisfying the SPA criterion for relaxation, which are used in Paper II to constrain cosmological models. Clusters ordered by increasing redshift, left-to-right and top-to-bottom. All images are scaled by the factor f_S given in Equation 3 and use the same logarithmic color scale. Each square image is r_{2500} on a side, according to the analysis of Paper II. Masked regions have been filled in by randomly sampling values from nearby, unmasked pixels.
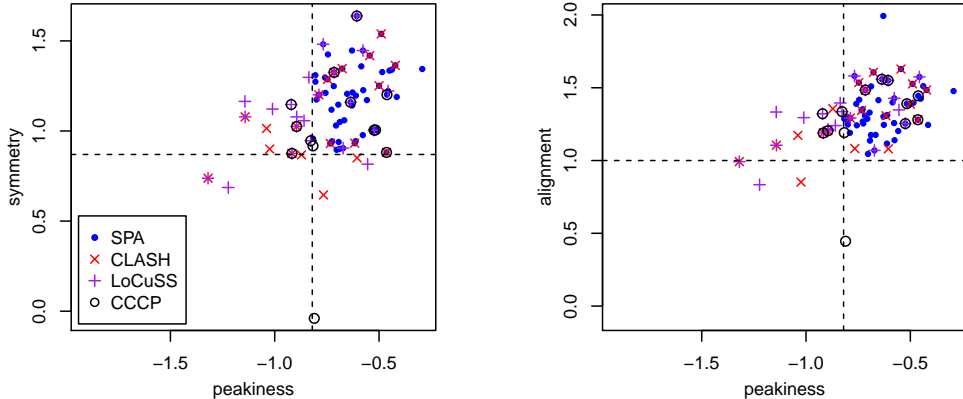
Figure 15: Peakiness–symmetry and peakiness–alignment distributions from our *Chandra* analysis. Shown are clusters selected according to our SPA criterion, "relaxed" clusters from CLASH (Postman et al. 2012), low centroid variance clusters from LoCuSS (Martino et al. 2014), and low central entropy clusters from the CCCP (Mahdavi et al. 2013).

5.7 Comparison with Other X-ray Image-Based Samples

For reference, we show in Figure 15 the morphological quantities from our analysis for clusters which have been selected by broadly similar criteria to ours, specifically subsets of the Cluster Lensing And Supernova survey with Hubble (CLASH; Postman et al. 2012), the Local Cluster Substructure Survey (LoCuSS; Martino et al. 2014), and the Canadian Cluster Comparison Project (CCCP; Mahdavi et al. 2013). Significantly, only in the case of CLASH is the cluster selection explicitly described as targeting relaxed systems (in this case, a majority are selected from A08). The LoCuSS and CCCP clusters considered here are instead selected based on a single measurement, respectively the centroid variance and central entropy. While only ∼ 50 per cent of the clusters selected in these independent samples typically meet our SPA criterion, they clearly are close to relaxation (by our metric) compared with the cluster population as a whole, as one would expect. (The most obvious outlier in Figure 15 is Abell 115, selected in CCCP due to the cool core in the northern sub-cluster.)

5.8 Additional X-ray Morphological Statistics

In this section, we consider three additional morphological quantities which are potentially of interest, but which do not inform our criterion for relaxation. Each of these is a function of the elliptical isophote model fits described in Section 4.4, namely (1) their mean ellipticity, (2) the change of ellipticity with brightness, and (3) the change of position angle with brightness. The latter two cases we quantify with a "slope" obtained by regressing ellipticity or position angle against the index of the isophotes, which is effectively the logarithm of the surface brightness (Equation 4). Figure 16 compares histograms of relaxed and unrelaxed clusters for these three quantities.

While the lowest mean ellipticity clusters are relaxed, and the highest unrelaxed, the two distributions overlap considerably. In particular, the excess density of the relaxed distribution at the lowest ellipticities corresponds to only 3 clusters. At large ellipticities, the heavy tail seen in the unrelaxed cluster distribution consists of messy mergers rather than simple, prolate ellipsoids seen in the plane of the sky, and is thus not replicated in the relaxed sample. Discounting this tail, we thus see no evidence that the SPA selection of relaxed clusters is particularly biased towards lower than typical projected ellipticities, i.e. clusters likely to be elongated along the line of sight as opposed to in the plane of the sky. This is by construction, since our morphological estimators do not penalize clusters for having ellipsoidal rather than circular shapes in projection. For all clusters, the mean ellipticity is 0.22, with an intrinsic (Gaussian) scatter of 0.08.

The distributions of ellipticity slope and position angle slope peak near zero for both relaxed and unrelaxed clusters, but are more sharply peaked for relaxed clusters. The difference is particularly evident for the ellipticity slope, which for unrelaxed clusters is asymmetric and has a heavy tail towards positive values (larger ellipticity at smaller radius/greater brightness). The ellipticity slope is plotted against each of the SPA measurements in Figure 16, which shows that the clusters with the lowest alignment and symmetry also tend to have large absolute values of the ellipticity slope. This is intuitive, as all three indicators should be sensitive to the effects of ongoing merger activity on cluster emission.

19
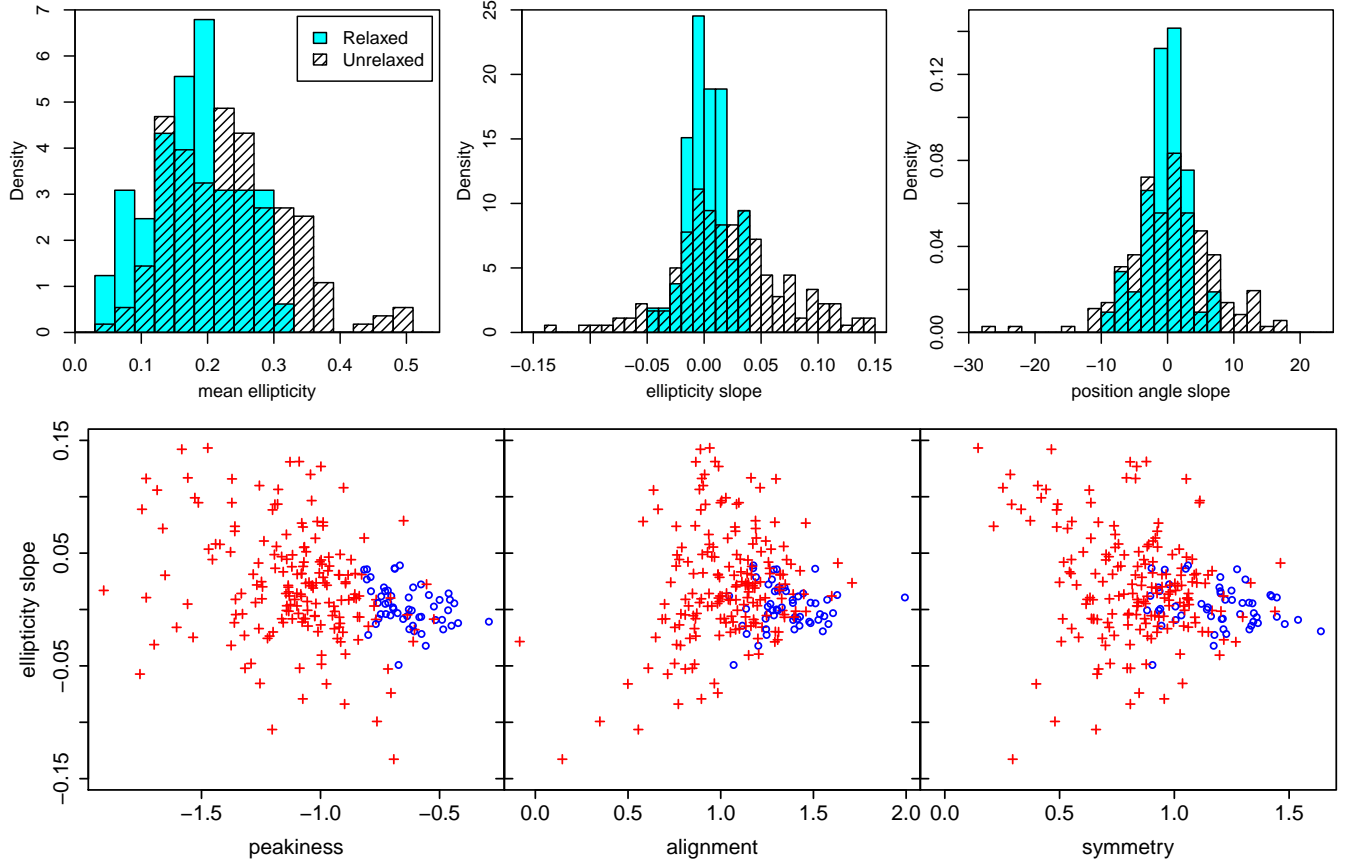
Figure 16: Top row: Histograms (normalized by sample size) of the mean ellipticity, ellipticity slope (i.e. the trend with isophote/radius) and position angle slope for clusters classified as relaxed or unrelaxed, based on the set of elliptical isophote fits generated by our analysis. The relaxed sample has slightly lower (but consistent) ellipticity compared with the unrelaxed sample, and has more consistent ellipticities and position angles as a function of radius. Bottom: Ellipticity slope is plotted against our three morphological statistics, with relaxed clusters shown as blue circles, and unrelaxed clusters as red crosses. The least relaxed clusters in terms of alignment and symmetry tend to also be outliers in ellipticity slope.

5.9 Trends with Redshift, Temperature and Parent Sample

The fraction of clusters that are relaxed as a function of mass and redshift has important implications for cluster cosmology, in addition to astrophysical significance. In this section, we consider four subsets of the data set, defined according to how they were originally selected: from the X-ray flux-limited ROSAT All-Sky Survey (RASS),[19] the 400d ROSAT survey, the SPT-SZ cluster survey, and the *Planck* Early SZ sample (Planck Collaboration 2014). Here we remove from consideration the 400d detections at $z < 0.35$, for which *Chandra* follow-up is neither extensive nor systematic. For the *Planck* sample, we consider only the 30 most significant SZ detections in terms of signal-to-noise, all of which were previously known in our source X-ray catalogs. The resulting sample is thus well represented in our data set, while nevertheless being SZ rather than X-ray selected. To good approximation, this *Planck* sample, and the *Chandra* follow-up of SPT clusters, can be considered fair selections of SZ signal-to-noise limited surveys, with the effective mass limit of the *Planck* sample being somewhat higher. The distribution of each of these samples in redshift and temperature is shown in Figure 5.9. Note that in this section we use only clusters where our temperatures are based on spectral measurements, as opposed to being estimated using an X-ray luminosity–temperature relation.

In principle, X-ray selected samples should be biased in favor of detecting strongly peaked clusters, due to the enhanced X-ray surface brightness that this implies, and we therefore expect the yield of relaxed clusters to be higher than in other samples. In contrast, SZ selection is not directly dependent on any of the X-ray surface brightness features we have measured. Merging could plausibly affect the SZ detectability of a cluster: in most cases we expect a decrease in the SZ signal for a given mass, since the ICM takes some time to reach its post-merger virial temperature,

---

[19]Strictly speaking, the BCS, REFLEX, CIZA and MACS samples, which we collectively call RASS here, were also constructed using different methods to detect cluster emission. However, particularly given the exhaustive optical follow-up and confirmation employed for the RASS samples, these differences are relatively minor.
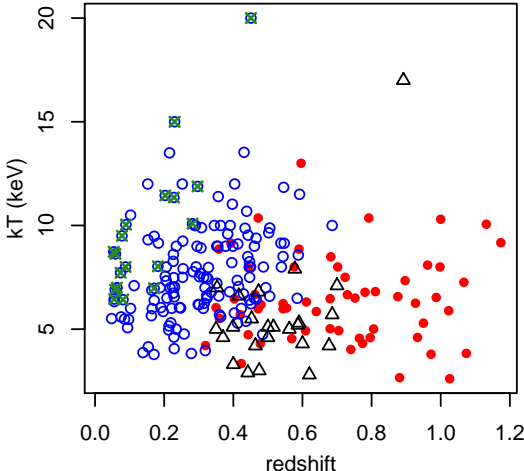
Figure 17: The redshift–temperature distribution of four differently selected cluster populations within our data set: those detected in the X-ray flux-limited ROSAT All-Sky Survey (blue, open circles), the smaller 400 square degree ROSAT survey (black triangles), the SZ-selected SPT cluster survey (red, filled circles), and an SZ-selected subset of the *Planck* Early SZ catalog (green crosses).

but the generation of a strong shock could significantly if briefly boost the SZ signal from a merging cluster. A variety of hydrodynamical simulations indicate that the net bias of SZ samples due to mergers should be relatively small (Yang et al. 2010, Rasia et al. 2011, Battaglia et al. 2012, Krause et al. 2012), although the dependence of these predictions on complex gas physics is such that they must be treated with caution. The uncertain effect of X-ray and SZ selection biases, as well as the relatively large statistical uncertainties, should be kept in mind throughout the following discussion.

With that caveat in mind, Figure 18 shows, for each cluster sample, the redshift and temperature dependence of three quantities: the fraction of relaxed clusters, the fraction of peaky clusters (satisfying our cut in peakiness, irrespective of symmetry or alignment), and the fraction of "undisturbed" clusters (satisfying cuts in symmetry and alignment, irrespective of peakiness). Horizontal bars in the figure show the bins in z or kT, points the relaxed, peaky or undisturbed fraction in each bin, and vertical bars the corresponding 68.3 per cent confidence intervals.[20] In choosing the bins, we have endeavored to make the results for different samples as straightforward to compare as possible, while still having a statistically useful number of clusters in each bin.[21]

Due to selection effects, we expect the X-ray samples to contain a larger fraction of peaky clusters than SZ samples at any redshift or temperature. In fact, since there is also a correlation between peakiness and both symmetry and alignment, this preference should also hold for the undisturbed and relaxed fractions. For the RASS sample this is indeed the case; the relaxed, peaky and undisturbed fractions uniformly exceed those of SZ samples. They are, in addition, approximately constant as a function of both redshift and mass (with the possible exception of the peaky fraction as a function of z). Overall, the relaxed cluster fraction of RASS is 29 per cent.

However, the situation is markedly different for the 400d sample, which in all respects appears more similar to the SZ samples (below) than to the RASS sample. In particular, the fraction of peaky clusters in the 400d sample is significantly smaller than in RASS, as has been remarked on previously (Vikhlinin et al. 2007, Mantz 2009, Santos et al. 2010). We find no relaxed clusters in the 400d sample. Note that, while the RASS and 400d samples are essentially disjoint in the X-ray luminosity–redshift plane (e.g. Allen et al. 2011), they do overlap in both redshift and temperature (a more reliable tracer of mass than luminosity; see the right panel of Figure 18). The level of disagreement between the two X-ray samples suggests two possible explanations: either the relaxed cluster fraction drops precipitously at relatively high redshifts and low masses, or the selection properties of the two samples are significantly different. For example, wavelet-based detection algorithms designed to automatically reject point-like sources, which the 400d sample employs, could plausibly be biased against finding peaky clusters near the flux limit (Santos et al. 2010).

Taking the SPT and *Planck* samples together, the relaxed cluster fraction in SZ samples is consistent with being constant with redshift; this behavior is similar to the RASS sample, but the SZ relaxed fraction is lower (8.5 per cent overall). The SZ relaxed fraction is consistent with RASS at high temperatures, $kT \gtrsim 10\,\mathrm{keV}$, but appears to decrease down to zero for cooler clusters, $kT \lesssim 6\,\mathrm{keV}$. As a function of temperature, the peaky and undisturbed fractions behave similarly, increasing from $\lesssim 0.1$ at low temperatures to values comparable to the RASS sample at $\gtrsim 10\,\mathrm{keV}$. In contrast, their trends with redshift differ; the peaky fraction is consistent with a constant, while

---

[20]We adopt a uniform prior between 0 and 1 on the fraction of relaxed (or peaky or undisturbed) clusters in a given redshift or temperature bin. With this choice, for a bin where x clusters are found to be relaxed and y unrelaxed, the posterior for the relaxed fraction is the Beta distribution with shape parameters $x + 1$ and $y + 1$.

[21]In practice, we aimed to have ≥ 10 clusters in each bin. Matching the approximate redshift and temperature binning across samples sometimes resulted in there being significantly more, ~ 70 in the case of the most populated bin. The exception is the highest-kT bin for the 400d sample, which contains only 1 cluster.
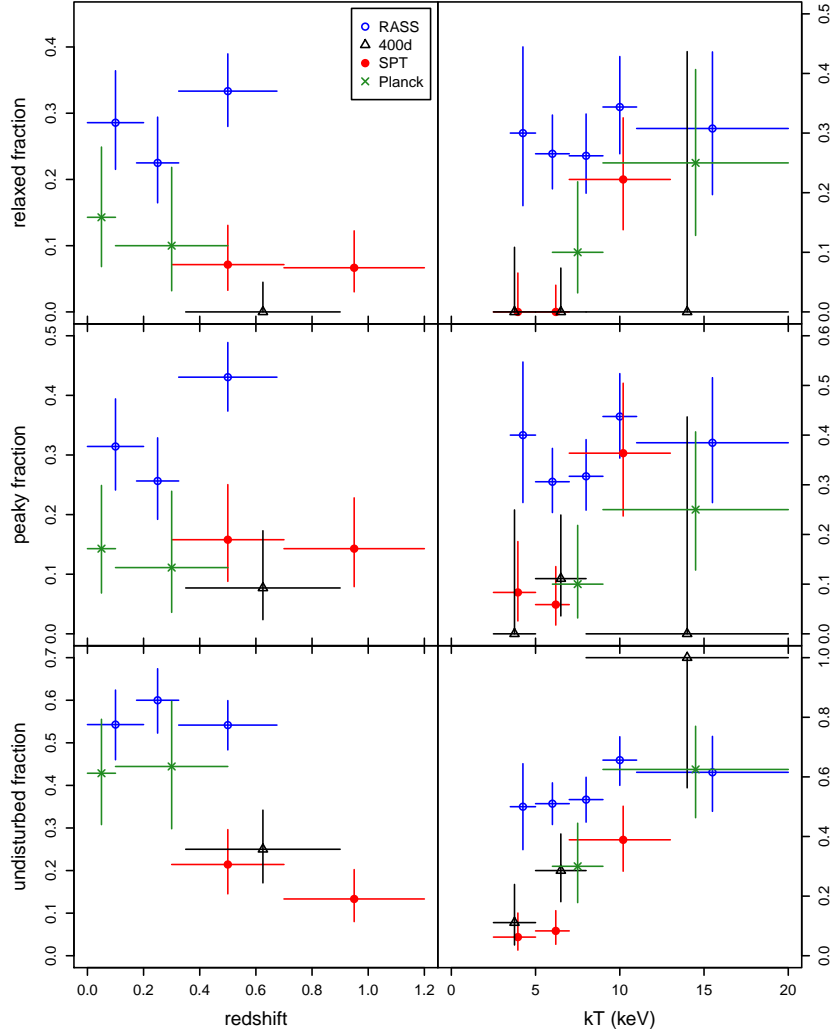
Figure 18: The fraction of relaxed, peaky and undisturbed clusters as a function of redshift and temperature, as determined for four differently selected cluster populations: those detected in the X-ray flux-limited ROSAT All-Sky Survey (high X-ray luminosity at redshifts < 0.7), the smaller 400 square degree ROSAT survey (lower luminosities at redshifts $0.35 < z < 0.9$), the SZ-selected SPT cluster survey, and an SZ-selected subset of the *Planck* Early SZ catalog. Horizontal bars indicate bins in redshift or temperature, points the fraction in each bin, and vertical bars the corresponding 68.3 per cent confidence intervals (for equivalently selected clusters). In the right panels, SPT points have been offset slightly in kT for clarity. "Peaky" refers to clusters which satisfy our peakiness cut, irrespective of symmetry and alignment, and conversely "undisturbed" refers to clusters satisfying cuts in symmetry and alignment, irrespective of peakiness.

the undisturbed fraction decreases with z. The latter is, however, largely an artifact of the observed kT dependence combined with the differing redshift–temperature distributions of the *Planck* and SPT samples. Restricting the SPT sample to $kT > 6\,\mathrm{keV}$ (i.e. to the range spanned by the *Planck* clusters) increases its undisturbed fraction to 26 per cent, reducing the evidence of a trend with redshift, while not significantly changing the picture for the peaky fraction.

Both the absolute value of the SZ peaky fraction (14 per cent overall) and its constant behavior with redshift are consistent with the predictions of hydrodynamical simulations (Burns et al. 2008, Planelles & Quilis 2009). However, the same simulations predict a decreasing cool-core fraction with cluster mass, which contradicts the increasing fraction of peaky clusters with temperature observed for the SZ sample. The increase in the undisturbed fraction with temperature, and its decrease with redshift (if real), are also seemingly in contradiction with simulations, which predict a mildly decreasing relaxed fraction (increasing fraction of merging clusters) as a function of mass and a constant merging fraction with redshift (Planelles & Quilis 2009, Fakhouri et al. 2010). Note, however, that these simulations contain relatively few clusters in the mass range of our data set, and generally combine these into a single

bin of masses $\gtrsim 10^{14}\,M_\odot$. Hence, the simulation results reflect trends with mass between cluster and group scales, not necessarily within the mass range probed by our data.

A strong SZ selection bias favoring mergers, though contrary to expectations, could account for the lack of relaxed clusters at low temperatures in our SZ sample. However, the close agreement of the SZ and 400d results poses a problem for this explanation, since it would need the 400d X-ray selection to be similarly biased in favor of mergers. A simpler scenario is simply that the 400d selection is not biased towards finding strongly peaked clusters, as speculated above, and thus finds clusters morphologically similar to SZ searches. Note that, according to this picture, the lack of cool cores in the 400d sample compared to RASS is not due to its higher redshift coverage (as suggested by Vikhlinin et al. 2007), but rather its lower mass range in combination with different selection effects.

Assuming that the temperature trends seen in the SZ sample are indeed real, they have potentially interesting implications for cool core formation and survival. Specifically, the increasing peaky fraction implies that cool core disruption is more efficient in less massive halos. There are several known examples of cool cores being destroyed by ram pressure stripping as they oscillate (slosh) about the bottom of the cluster potential following a merger (Markevitch et al. 2000, Mazzotta et al. 2001, Million et al. 2010, Ehlert et al. 2011, Ichinohe et al. 2014, Canning et al., in prep.), a process also observed in hydrodynamic simulations (e.g. Burns et al. 2008, ZuHone et al. 2011). Hence a possible explanation is that mergers with the necessary mass ratio and impact parameter to destroy a hosted cool core via sloshing are relatively less common for the most massive clusters, despite these clusters having a larger merger rate overall; this would be qualitatively consistent with the larger undisturbed fraction we observe for the most massive clusters. Since cool core development is manifestly a non-self-similar phenomenon, it may also be the case that cool cores formed in more massive clusters are intrinsically more resilient to ram pressure stripping by the ambient ICM.

Regardless of the reasons underlying the observed trends, we can make some broad statements about the best strategy for finding new relaxed clusters. Overall, the greatest yield of relaxed clusters can be obtained from an all-sky X-ray survey with greater sensitivity than RASS (such as eROSITA; Predehl et al. 2010), provided that the cluster detection algorithm does not reject peaky cool-core clusters. Assuming optical/IR follow-up observations exist, a first cut for selecting relaxed clusters can be made using the X-ray/BCG position offset in all cases. For a fraction of the discovered clusters, it should be possible to make additional, preliminary cuts from the X-ray survey data based on peakiness alone or, for the brightest systems, using the full suite of SPA measurements (adjusting appropriately for image resolution). However, the similarity of the RASS and SZ relaxed fractions at high temperatures strongly suggests that targeted X-ray snapshots of the most significant detections in SZ surveys would be an efficient complement for finding relaxed clusters, particularly at high redshifts where X-ray survey data suffer more from cosmological dimming.

6 Summary

We have presented a new suite of image measurements used to assess the X-ray morphology of galaxy clusters. These estimators are designed to provide a fair basis for comparison over a wide range in redshift, to avoid strong assumptions regarding the background cosmology and cluster scaling relations, and to be as robust as possible against incomplete images (due to CCD gaps, point-source masks, etc.). The three statistics we use respectively probe the *peakiness* of the cluster surface brightness profile, the degree of *alignment* between isophotes at intermediate radii, and the *symmetry* of those isophotes with respect to a globally determined center. Uncertainties are propagated faithfully by bootstrap sampling the original images and varying the background normalization.

These measurements were performed for a sample of 361 galaxy clusters, selected from several X-ray and SZ cluster surveys, using a combination of archival *Chandra* and ROSAT observations. There are clear correlations between the new measurements and more traditional X-ray estimators, indicating that they are sensitive to similar features, as expected. Intuitively, our peakiness measure also correlates clearly with the metric distance separating the X-ray center and the BCG. Motivated by trends in the data and comparison with the earlier relaxed cluster sample of A08, we define a requirement for a cluster to be considered morphologically relaxed in terms of the symmetry, peakiness and alignment measurements. The fraction of relaxed clusters identified this way is strongly dependent on the selection of the parent sample. We find a higher relaxed fraction in clusters selected from the RASS compared with SZ samples (respectively 0.29 and 0.085), as expected due to the strong dependence of X-ray detectability on surface brightness peakiness. Furthermore, the relaxed fraction in RASS is consistent with being constant with both redshift and ICM temperature, whereas an increasing trend with temperature is observed in the SZ-selected sample.

The relaxed sample identified here, with some refinements based on cluster temperature and data quality, is used to derive cosmological constraints from cluster gas mass fractions in Paper II. As described in that work, significant improvements in dark energy constraints using this method will require the efficient identification and follow-up of relaxed clusters discovered in new cluster surveys. The algorithms introduced here provide a widely useful tool for identifying relaxed systems in new data, and for quantifying the morphological states of cluster samples in general.

Acknowledgments

References

Abazajian K. N. et al., 2009, ApJS, 182, 543

Ahn C. P. et al., 2014, ApJS, 211, 17

Allen S., Schmidt R., Fabian A., 2002, MNRAS, 334, L11

Allen S. W., Evrard A. E., Mantz A. B., 2011, ARA&A, 49, 409

Allen S. W., Rapetti D. A., Schmidt R. W., Ebeling H., Morris R. G., Fabian A. C., 2008, MNRAS, 383, 879

Allen S. W., Schmidt R. W., Ebeling H., Fabian A. C., van Speybroeck L., 2004, MNRAS, 353, 457

Allen S. W., Schmidt R. W., Fabian A. C., 2001, MNRAS, 328, L37

Allen S. W. et al., 2001, MNRAS, 324, 842

Arnaud K. A., Fabian A. C., Eales S. A., Jones C., Forman W., 1984, MNRAS, 211, 981

Arnaud M., Pointecouteau E., Pratt G. W., 2007, A&A, 474, L37

Ascasibar Y., Markevitch M., 2006, ApJ, 650, 102

Battaglia N., Bond J. R., Pfrommer C., Sievers J. L., 2012, ApJ, 758, 74

Bleem L. E. et al., 2015, ApJS, 216, 27

Böhringer H. et al., 2010, A&A, 514, A32

Böhringer H. et al., 2004, A&A, 425, 367

Buote D. A., 2001, ApJL, 553, L15

Buote D. A., Tsai J. C., 1995, ApJ, 452, 522

Burenin R. A., Vikhlinin A., Hornstrup A., Ebeling H., Quintana H., Mescheryakov A., 2007, ApJS, 172, 561

Burns J. O., Hallman E. J., Gantner B., Motl P. M., Norman M. L., 2008, ApJ, 675, 1125

Cassano R. et al., 2013, ApJ, 777, 141

Cassano R., Ettori S., Giacintucci S., Brunetti G., Markevitch M., Venturi T., Gitti M., 2010, ApJL, 721, L82

Cavaliere A., Fusco-Femiano R., 1976, A&A, 49, 137

Crawford C. S., Allen S. W., Ebeling H., Edge A. C., Fabian A. C., 1999, MNRAS, 306, 857

Croston J. H. et al., 2008, A&A, 487, 431

Ebeling H., Barrett E., Donovan D., Ma C.-J., Edge A. C., van Speybroeck L., 2007, ApJL, 661, L33

Ebeling H., Edge A. C., Bohringer H., Allen S. W., Crawford C. S., Fabian A. C., Voges W., Huchra J. P., 1998, MNRAS, 301, 881

Ebeling H., Edge A. C., Henry J. P., 2001, ApJ, 553, 668

Ebeling H., Edge A. C., Mantz A., Barrett E., Henry J. P., Ma C. J., van Speybroeck L., 2010, MNRAS, 407, 83

Ebeling H., Mullis C. R., Tully R. B., 2002, ApJ, 580, 774

Ehlert S. et al., 2011, MNRAS, 411, 1641

Fabian A. C., 2012, ARA&A, 50, 455

Fabian A. C., Crawford C. S., Edge A. C., Mushotzky R. F., 1994, MNRAS, 267, 779

Fabian A. C., Sanders J. S., Allen S. W., Crawford C. S., Iwasawa K., Johnstone R. M., Schmidt R. W., Taylor G. B., 2003, MNRAS, 344, L43

Fabian A. C. et al., 2000, MNRAS, 318, L65

Fabian A. C., Sanders J. S., Taylor G. B., Allen S. W., Crawford C. S., Johnstone R. M., Iwasawa K., 2006, MNRAS, 366, 417

Fakhouri O., Ma C.-P., Boylan-Kolchin M., 2010, MNRAS, 406, 2267

Feretti L., Giovannini G., Govoni F., Murgia M., 2012, A&AR, 20, 54

Forman W., Bechtold J., Blair W., Giacconi R., van Speybroeck L., Jones C., 1981, ApJL, 243, L133

Forman W. et al., 2007, ApJ, 665, 1057

Forman W. et al., 2005, ApJ, 635, 894

Henning J. W., Gantner B., Burns J. O., Hallman E. J., 2009, ApJ, 697, 1597

Hlavacek-Larrondo J., Fabian A. C., Edge A. C., Ebeling H., Sanders J. S., Hogan M. T., Taylor G. B., 2012, MNRAS, 421, 1360

Ichinohe Y., Werner N., Simionescu A., Allen S. W., Canning R. E. A., Ehlert S., Mernier F., Takahashi T., 2014, arXiv:1410.1955

Jeltema T. E., Canizares C. R., Bautz M. W., Buote D. A., 2005, ApJ, 624, 606

Johnson R. E., Zuhone J., Jones C., Forman W. R., Markevitch M., 2012, ApJ, 751, 95

Kaiser N., 1986, MNRAS, 222, 323

Kocevski D. D., Ebeling H., Mullis C. R., Tully R. B., 2007, ApJ, 662, 224

Krause E., Pierpaoli E., Dolag K., Borgani S., 2012, MN-RAS, 419, 1766

Mahdavi A., Hoekstra H., Babul A., Bildfell C., Jeltema T., Henry J. P., 2013, ApJ, 767, 116

Mantz A., 2009, Ph.D. thesis, Stanford University, ADS

Mantz A., Allen S. W., Ebeling H., Rapetti D., Drlica-Wagner A., 2010b, MNRAS, 406, 1773

Mantz A., Allen S. W., Rapetti D., Ebeling H., 2010a, MNRAS, 406, 1759

Mantz A. B., Allen S. W., Morris R. G., Rapetti D. A., Applegate D. E., Kelly P. L., von der Linden A., Schmidt R. W., 2014, MNRAS, 440, 2077

Markevitch M., Gonzalez A. H., David L., Vikhlinin A., Murray S., Forman W., Jones C., Tucker W., 2002, ApJL, 567, L27

Markevitch M., Govoni F., Brunetti G., Jerius D., 2005, ApJ, 627, 733

Markevitch M. et al., 2000, ApJ, 541, 542

Markevitch M., Vikhlinin A., 2007, Phys. Rep., 443, 1

Martino R., Mazzotta P., Bourdin H., Smith G. P., Bartalucci I., Marrone D. P., Finoguenov A., Okabe N., 2014, MNRAS, 443, 2342

Mazzotta P., Markevitch M., Vikhlinin A., Forman W. R., David L. P., van Speybroeck L., 2001, ApJ, 555, 205

McDonald M. et al., 2012, Nat, 488, 349

McDonald M. et al., 2013, ApJ, 774, 23

McNamara B. R. et al., 2000, ApJL, 534, L135

Meneghetti M. et al., 2014, ApJ, 797, 34

Million E. T., Allen S. W., Werner N., Taylor G. B., 2010, MNRAS, 405, 1624

Mohr J. J., Fabricant D. G., Geller M. J., 1993, ApJ, 413, 492

Nurgaliev D., McDonald M., Benson B. A., Miller E. D., Stubbs C. W., Vikhlinin A., 2013, ApJ, 779, 112

Paterno-Mahler R., Blanton E. L., Randall S. W., Clarke T. E., 2013, ApJ, 773, 114

Peres C. B., Fabian A. C., Edge A. C., Allen S. W., Johnstone R. M., White D. A., 1998, MNRAS, 298, 416

Peterson J. R., Fabian A. C., 2006, Phys. Rep., 427, 1

Planck Collaboration, 2014, A&A, 571, A29

Planelles S., Quilis V., 2009, MNRAS, 399, 410

Postman M. et al., 2012, ApJS, 199, 25

Predehl P. et al., 2010, Vol. 7732, Society of Photo-Optical Instrumentation Engineers (SPIE) Conference Series

Rapetti D., Allen S. W., Mantz A., 2008, MNRAS, 388, 1265

Rapetti D., Allen S. W., Weller J., 2005, MNRAS, 360, 555

Rasia E., Mazzotta P., Evrard A., Markevitch M., Dolag K., Meneghetti M., 2011, ApJ, 729, 45

Rasia E., Meneghetti M., Ettori S., 2013, The Astronomical Review, 8, 010000

Roediger E., Brüggen M., Simionescu A., Böhringer H., Churazov E., Forman W. R., 2011, MNRAS, 413, 2057

Rossetti M., Eckert D., Cavalleri B. M., Molendi S., Gastaldello F., Ghizzardi S., 2011, A&A, 532, A123

Santos J. S., Rosati P., Tozzi P., Böhringer H., Ettori S., Bignamini A., 2008, A&A, 483, 35

Santos J. S., Tozzi P., Rosati P., Böhringer H., 2010, A&A, 521, A64

Schmidt R. W., Allen S. W., 2007, MNRAS, 379, 209

Schmidt R. W., Allen S. W., Fabian A. C., 2004, MN-RAS, 352, 1413

Semler D. R. et al., 2012, ApJ, 761, 183

Siemiginowska A., Burke D. J., Aldcroft T. L., Worrall D. M., Allen S., Bechtold J., Clarke T., Cheung C. C., 2010, ApJ, 722, 102

Simionescu A. et al., 2011, Sci, 331, 1576

Simionescu A. et al., 2012, ApJ, 757, 182

Skory S., Hallman E., Burns J. O., Skillman S. W., O'Shea B. W., Smith B. D., 2013, ApJ, 763, 38

Snowden S. L., McCammon D., Burrows D. N., Mendenhall J. A., 1994, ApJ, 424, 714

Song J. et al., 2012, ApJ, 761, 22

Urban O. et al., 2014, MNRAS, 437, 3939

Urban O., Werner N., Simionescu A., Allen S. W., Böhringer H., 2011, MNRAS, 414, 2101

Vikhlinin A., Burenin R., Forman W. R., Jones C., Hornstrup A., Murray S. S., Quintana H., 2007, in Böhringer H., Pratt G. W., Finoguenov A., Schuecker P., eds, Heating versus Cooling in Galaxies and Clusters of Galaxies, p. 48

Vikhlinin A. et al., 2009a, ApJ, 692, 1033

Vikhlinin A., Kravtsov A., Forman W., Jones C., Markevitch M., Murray S. S., Van Speybroeck L., 2006, ApJ, 640, 691

Vikhlinin A. et al., 2009b, ApJ, 692, 1060

Vikhlinin A., Markevitch M., Murray S. S., 2001, ApJ, 551, 160

Vikhlinin A., Markevitch M., Murray S. S., Jones C., Forman W., Van Speybroeck L., 2005, ApJ, 628, 655

von der Linden A. et al., 2014, MNRAS, 439, 2

Walker S. A., Fabian A. C., Sanders J. S., George M. R., 2012a, MNRAS, 424, 1826

Walker S. A., Fabian A. C., Sanders J. S., George M. R., Tawara Y., 2012b, MNRAS, 422, 3503

White D. A., Jones C., Forman W., 1997, MNRAS, 292, 419

Yang H.-Y. K., Bhattacharya S., Ricker P. M., 2010, ApJ, 725, 1124

ZuHone J. A., Markevitch M., Lee D., 2011, ApJ, 743, 16

A X-ray Data

Tables 2 and 3 provides details of the *Chandra* and ROSAT observations employed here.

B Complete Results

Table 4 extends the listing of results in Table 1 to the entire data set.

Table 2: *Chandra* data used in this work: [1] cluster name (ordered as in Table 1); [2] observation ID; [3] date of observation; [4] blank-sky background epoch; [5] detector (ACIS-I or ACIS-S); [6] data mode (VFAINT or FAINT; V⋆ indicates VFAINT reduced in FAINT mode); [7] nominal exposure length, ks; [8] good time interval remaining after filtering, ks (E indicates an excluded exposure).

Cluster	ObsID	Date	B	D	M	exp.	gti
Abell 1068	1652	2001-02-04	D	S	F	26.8	24.3
Abell 1068	3068	2002-03-11	D	S	F	6.0	E
Abell 1132	13376	2011-08-25	E	I	V	8.9	8.7
Abell 115	3233	2002-10-07	D	I	V	49.7	39.7
Abell 1201	4216	2003-11-01	D	S	V	39.7	16.4
Abell 1201	7697	2007-03-18	E	I	V	4.9	4.7
Abell 1201	9616	2008-04-06	E	I	V	47.4	45.6
Abell 1204	2205	2001-06-01	D	I	V	23.6	20.2
Abell 1246	11770	2009-10-30	E	I	V	5.0	4.7
Abell 1413	537	2000-06-23	C	I	V⋆	9.6	E
Abell 1413	1661	2001-05-16	D	I	V	9.7	8.7
Abell 1413	5003	2004-03-06	D	I	V	75.1	64.2
Abell 1413	5002	2005-02-03	D	I	V	36.7	32.1
Abell 1413	7696	2007-07-10	E	I	V	5.1	4.3
Abell 1423	538	2000-07-07	C	I	V⋆	9.9	9.6
Abell 1423	11724	2010-07-12	E	I	V	25.7	23.4
Abell 1553	12254	2010-11-20	E	I	V	13.9	11.8
Abell 1682	3244	2002-10-19	D	I	V	9.8	E
Abell 1682	11725	2009-11-06	E	I	V	19.9	17.8
Abell 1758	2213	2001-08-28	D	S	V	58.3	E
Abell 1758	7710	2007-07-12	E	I	V	7.0	6.2
Abell 1763	3591	2003-08-28	D	I	V	19.6	16.5
Abell 1795	494	1999-12-20	B	S	F	19.5	E
Abell 1795	493	2000-03-21	C	S	V⋆	19.6	18.4
Abell 1795	3666	2002-06-10	D	S	V	14.4	13.4
Abell 1795	5286	2004-01-14	D	S	V	14.3	12.2
Abell 1795	5287	2004-01-14	D	S	V	14.3	12.3
Abell 1795	5288	2004-01-16	D	S	V	14.6	13.5
Abell 1795	5289	2004-01-18	D	I	V	15.0	12.5
Abell 1795	5290	2004-01-23	D	I	V	14.9	12.9
Abell 1795	6159	2005-03-20	D	I	V	14.9	12.8
Abell 1795	6160	2005-03-20	D	S	V	14.8	14.8
Abell 1795	6161	2005-03-28	D	I	V	13.6	12.3
Abell 1795	6162	2005-03-28	D	I	V	13.6	12.8
Abell 1795	6163	2005-03-31	D	I	V	14.9	14.3
Abell 1795	10432	2009-03-16	E	I	V	5.1	4.6
Abell 1795	10433	2009-03-23	E	I	V	5.1	5.1
Abell 1795	10898	2009-04-20	E	I	V	15.7	14.8
Abell 1795	10900	2009-04-20	E	S	V	15.8	15.8
Abell 1795	10901	2009-04-20	E	S	V	15.5	13.3
Abell 1795	10899	2009-04-22	E	I	V	14.9	13.4
Abell 1795	12027	2010-03-16	E	I	V	14.8	14.3
Abell 1795	12029	2010-04-28	E	S	V	14.7	14.7
Abell 1795	12028	2010-05-10	E	S	V	15.0	15.0
Abell 1795	12026	2010-05-11	E	I	V	14.9	13.6
Abell 1795	13108	2011-03-10	E	I	V	14.9	14.3
Abell 1795	13109	2011-03-11	E	I	V	14.6	13.8
Abell 1795	13110	2011-03-11	E	I	V	14.6	13.3
Abell 1795	13111	2011-03-11	E	I	V	14.6	12.5
Abell 1795	13112	2011-03-11	E	I	V	14.6	13.8
Abell 1795	13113	2011-03-11	E	I	V	14.6	13.6
Abell 1795	13106	2011-04-01	E	S	V	9.9	9.9
Abell 1795	13107	2011-04-01	E	S	V	9.6	9.6
Abell 1795	13412	2011-05-22	E	I	V	14.9	E
Abell 1795	13413	2011-05-29	E	I	V	14.9	14.1
Abell 1795	13414	2011-05-29	E	I	V	14.6	14.1
Abell 1795	13415	2011-05-29	E	I	V	14.6	13.3
Abell 1795	13416	2011-05-30	E	I	V	14.6	12.8
Abell 1795	13417	2011-06-02	E	I	V	14.9	13.8
Abell 1795	14270	2012-03-25	E	I	V	14.3	13.5
Abell 1795	14271	2012-03-25	E	I	V	14.0	9.1

Table 2: continued

Cluster	ObsID	Date	B	D	M	exp.	gti
Abell 1795	14272	2012-03-25	E	I	V	14.6	13.3
Abell 1795	14268	2012-03-26	E	S	V	9.9	9.9
Abell 1795	14273	2012-03-26	E	I	V	14.6	12.8
Abell 1795	14274	2012-04-02	E	I	V	14.9	14.1
Abell 1795	14275	2012-04-07	E	I	V	14.9	12.8
Abell 1795	14269	2012-04-08	E	S	V	9.9	9.9
Abell 1835	495	1999-12-11	B	S	F	19.5	E
Abell 1835	496	2000-04-29	C	S	F	10.7	10.7
Abell 1835	6881	2005-12-07	E	I	V	36.3	29.9
Abell 1835	7370	2006-07-24	E	I	V	39.5	36.1
Abell 1835	6880	2006-08-25	E	I	V	117.9	107.9
Abell 1914	542	1999-11-21	B	I	V⋆	8.1	6.6
Abell 1914	3593	2003-09-03	D	I	V	18.9	16.1
Abell 2009	10438	2008-12-04	E	I	V	19.9	17.6
Abell 2029	891	2000-04-12	C	S	F	19.8	19.8
Abell 2029	4977	2004-01-08	D	S	F	77.9	72.8
Abell 2029	6101	2004-12-17	D	I	V	9.9	9.0
Abell 2029	10434	2009-04-01	E	I	V	5.1	4.9
Abell 2029	10435	2009-04-01	E	I	V	4.7	4.1
Abell 2029	10436	2009-04-01	E	I	V	4.7	3.8
Abell 2029	10437	2009-04-01	E	I	V	4.7	4.5
Abell 2034	2204	2001-05-05	D	I	V	53.9	44.2
Abell 2034	7695	2007-05-07	E	I	V	4.8	4.4
Abell 2034	12885	2010-11-22	E	I	V	81.2	73.0
Abell 2034	12886	2010-11-24	E	I	V	91.3	80.3
Abell 2034	13192	2010-11-28	E	I	V	16.8	15.6
Abell 2034	13193	2010-11-28	E	I	V	7.7	6.6
Abell 2065	3182_obi1	2002-08-18	D	I	V	27.7	E
Abell 2065	3182_obi2	2002-11-24	D	I	V	21.8	20.0
Abell 2065	7689	2007-09-13	E	I	V	5.1	4.8
Abell 2069	4965	2004-05-31	D	I	V	55.4	33.3
Abell 2111	544	2000-03-22	C	I	F	10.3	9.3
Abell 2111	11726	2009-11-12	E	I	V	20.9	19.6
Abell 2142	1196	1999-08-20	A	S	F	11.4	E
Abell 2142	1228	1999-08-20	A	S	F	12.1	E
Abell 2142	5005	2005-04-13	D	I	V	44.6	39.4
Abell 2142	7692	2007-05-07	E	I	V	5.0	4.7
Abell 2204	499	2000-07-29	C	S	F	10.1	9.0
Abell 2204	6104	2004-09-20	D	I	V	9.6	8.6
Abell 2204	7940	2007-06-06	E	I	V	77.1	72.0
Abell 2218	553	1999-10-19	B	I	F	5.9	5.9
Abell 2218	1454	1999-10-19	B	I	F	11.4	10.7
Abell 2218	1666	2001-08-30	D	I	V	48.6	31.7
Abell 2218	7698	2007-06-13	E	I	V	5.1	4.1
Abell 2219	896	2000-03-31	C	S	F	42.3	42.3
Abell 2219	7892	2007-09-27	E	I	V	5.1	4.8
Abell 2219	13988	2012-05-26	E	I	V	9.9	9.2
Abell 2219	14431	2012-05-27	E	I	V	38.6	34.7
Abell 2219	14451	2012-06-26	E	I	V	19.8	18.0
Abell 2219	14355	2012-06-28	E	I	V	29.7	25.8
Abell 2219	14356	2012-10-15	E	I	V	49.4	43.5
Abell 2244	4179	2003-10-10	D	S	V	57.0	53.9
Abell 2244	7693	2007-07-27	E	I	V	5.1	4.8
Abell 2255	894	2000-10-20	C	I	F	39.4	32.3
Abell 2255	7690	2007-07-02	E	I	V	5.1	4.4
Abell 2256	1386	1999-10-13	B	I	F	12.4	7.7
Abell 2256	965	1999-10-14	B	S	F	11.0	8.9
Abell 2256	1521	2000-02-27	C	S	F	2.9	E
Abell 2256	2419	2001-02-06	D	S	F	11.9	E
Abell 2259	3245	2002-09-16	D	I	V	10.0	8.4
Abell 2261	550	1999-12-11	B	I	V⋆	9.1	7.8
Abell 2261	5007	2004-01-14	D	I	V	24.3	21.7
Abell 2294	3246	2001-12-24	D	I	V	10.0	7.7
Abell 2390	501	1999-11-05	B	S	F	9.0	E
Abell 2390	500	2000-10-08	C	S	F	9.8	9.8
Abell 2390	4193	2003-09-11	D	S	V	95.1	69.6
Abell 2409	3247	2002-10-08	D	I	V	10.2	9.2
Abell 2631	3248	2002-07-08	D	I	V	9.2	8.4
Abell 2631	11728	2009-08-18	E	I	V	16.8	15.8
Abell 267	523	1999-10-16	B	I	V⋆	0.1	E

Cluster	ObsID	Date	B	D	M	exp.	gti
Abell 267	1448	1999-10-16	B	I	F	7.9	7.1
Abell 267	1517	2000-01-29	C	I	V⋆	1.2	E
Abell 267	3580	2003-12-07	D	I	V	19.9	15.5
Abell 401	518	1999-09-17	B	I	F	18.0	17.5
Abell 401	2309	2000-11-03	C	I	F	11.6	11.6
Abell 401	14024	2011-12-14	E	I	V	135.1	133.5
Abell 478	1669	2001-01-27	D	S	F	42.4	36.2
Abell 478	6102	2004-09-13	D	I	V	10.0	5.9
Abell 478	7217	2005-11-15	E	I	V	18.3	17.3
Abell 478	7218	2005-11-17	E	I	V	7.9	6.6
Abell 478	7222	2005-11-19	E	I	V	6.1	5.9
Abell 478	7235	2005-11-29	E	I	V	7.0	6.8
Abell 478	7234	2005-12-01	E	I	V	8.9	7.8
Abell 478	6928	2005-12-02	E	I	V	6.0	5.5
Abell 478	6929	2005-12-02	E	I	V	2.1	1.9
Abell 478	7233	2005-12-03	E	I	V	9.0	7.7
Abell 478	7232	2005-12-04	E	I	V	15.9	13.3
Abell 478	7231	2006-07-29	E	I	V	17.3	15.1
Abell 520	528	2000-10-10	C	I	V⋆	9.5	7.2
Abell 520	4215	2003-12-04	D	I	V	66.3	55.2
Abell 520	7703	2007-01-01	E	I	V	5.1	4.1
Abell 520	9425	2007-12-24	E	I	V	113.5	96.4
Abell 520	9424	2008-01-01	E	I	V	109.7	103.3
Abell 520	9426	2008-01-09	E	I	V	110.7	100.5
Abell 520	9430	2008-01-11	E	I	V	113.5	106.4
Abell 586	530	2000-09-05	C	I	V⋆	10.0	8.7
Abell 586	11723	2009-10-23	E	I	V	9.9	9.4
Abell 611	3194	2001-11-03	D	S	V	36.1	31.0
Abell 646	9306	2007-12-16	E	S	V	8.0	8.0
Abell 665	531	1999-12-29	B	I	V⋆	9.0	7.9
Abell 665	3586	2002-12-28	D	I	V	29.7	21.8
Abell 665	7700	2006-12-30	E	I	V	5.1	4.6
Abell 665	13201	2011-01-06	E	I	V	48.7	40.3
Abell 665	12286	2011-01-09	E	I	V	47.1	34.5
Abell 68	3250	2002-09-07	D	I	V	10.0	8.2
Abell 697	532	1999-10-21	B	I	F	8.0	E
Abell 697	4217	2002-12-15	D	I	V	19.5	15.2
Abell 750	924	2000-10-02	C	I	V⋆	29.8	28.5
Abell 750	7699	2007-01-02	E	I	V	4.7	4.2
Abell 773	533	2000-09-05	C	I	V⋆	11.3	9.7
Abell 773	3588	2003-01-25	D	I	V	9.4	8.1
Abell 773	5006	2004-01-21	D	I	V	19.8	17.9
Abell 781	534	2000-10-03	C	I	V⋆	9.9	8.9
Abell 795	11734	2010-01-13	E	S	V	29.7	29.7
Abell 963	903	2000-10-11	C	S	F	36.3	33.2
Abell 963	7704	2007-02-18	E	I	V	5.1	5.1
Hercules	1625	2001-07-25	D	S	V	14.8	13.8
Hercules	5796	2005-05-09	D	S	V	47.5	47.5
Hercules	6257	2005-05-25	D	S	V	49.5	49.5
RX J0439.0+0520	527	2000-08-29	C	I	V⋆	9.6	8.8
RX J0439.0+0520	9369	2007-11-12	E	I	V	19.9	18.6
RX J0439.0+0520	9761	2007-11-15	E	I	V	8.7	7.9
RX J0439.0+0715	526	1999-10-16	B	I	V⋆	1.6	E
RX J0439.0+0715	1449	1999-10-16	B	I	F	6.3	5.9
RX J0439.0+0715	1506	1999-12-09	B	I	V⋆	0.8	0.8
RX J0439.0+0715	3583	2003-01-04	D	I	V	19.2	15.4
RX J1720.1+2638	549	1999-10-19	B	I	V⋆	0.2	E
RX J1720.1+2638	1453	1999-10-19	B	I	F	7.8	7.0
RX J1720.1+2638	304	2000-04-19	C	I	F	2.3	2.3
RX J1720.1+2638	4361	2002-08-19	D	I	V	25.7	21.7
RX J1720.1+2638	3224	2002-10-03	D	I	V	23.8	18.7
RX J1750.2+3505	12252	2010-10-15	E	I	V	19.8	18.7
RX J2129.6+0005	552	2000-10-21	C	I	V⋆	10.0	9.2
RX J2129.6+0005	9370	2009-04-03	E	I	V	29.6	27.3
Zwicky 2089	7897	2006-12-23	E	I	V	9.0	8.2
Zwicky 2089	10463	2009-02-24	E	S	V	40.6	38.6
Zwicky 2701	3195	2001-11-04	D	S	V	26.9	14.6
Zwicky 2701	7706	2007-06-25	E	I	V	5.1	4.6
Zwicky 2701	12903	2011-02-03	E	S	V	95.8	92.1
Zwicky 3146	909	2000-05-10	C	I	F	46.0	41.2

Cluster	ObsID	Date	B	D	M	exp.	gti
Zwicky 3146	9371	2008-01-18	E	I	V	40.2	34.5
Zwicky 5029	4184	2003-07-28	D	I	V	12.1	9.7
Zwicky 5247	539	2000-03-23	C	I	V⋆	9.3	8.2
Zwicky 5247	11727	2009-11-20	E	I	V	20.9	19.6
Zwicky 7160	543	2000-05-19	C	I	F	9.9	7.9
Zwicky 7160	4192	2003-09-05	D	I	V	91.9	71.6
Zwicky 7160	7709	2007-03-23	E	I	V	7.1	6.8
Zwicky 808	12253	2010-10-06	E	I	V	18.8	17.0
1E 0657−56	554	2000-10-16	C	I	F	25.8	22.3
1E 0657−56	3184	2002-07-12	D	I	V	87.5	72.1
1E 0657−56	5355	2004-08-10	D	I	V	27.4	19.0
1E 0657−56	5356	2004-08-11	D	I	V	97.2	87.2
1E 0657−56	5357	2004-08-14	D	I	V	79.1	69.8
1E 0657−56	5358	2004-08-15	D	I	V	32.0	27.9
1E 0657−56	5361	2004-08-17	D	I	V	82.6	72.1
1E 0657−56	4984	2004-08-19	D	I	V	76.1	64.9
1E 0657−56	4985	2004-08-23	D	I	V	27.5	21.7
1E 0657−56	4986	2004-08-25	D	I	V	41.5	36.4
Abell 1650	4178	2003-08-03	D	S	V	27.3	23.5
Abell 1650	6356	2005-08-10	D	I	V	36.6	29.4
Abell 1650	6357	2005-08-11	D	I	V	32.7	29.4
Abell 1650	6358	2005-08-13	D	I	V	31.8	28.7
Abell 1650	5823	2005-11-28	E	I	V	39.6	34.7
Abell 1650	5822	2005-11-29	E	I	V	19.9	17.6
Abell 1650	7242	2006-03-01	E	I	V	37.2	34.3
Abell 1650	7691	2007-02-24	E	I	V	5.0	5.0
Abell 1651	4185	2003-03-02	D	I	V	9.6	9.1
Abell 1664	1648	2001-06-08	D	S	V	9.8	9.8
Abell 1664	7901	2006-12-04	E	S	V	36.6	36.6
Abell 1689	540	2000-04-15	C	I	F	10.3	9.8
Abell 1689	1663	2001-01-07	D	I	F	10.7	10.5
Abell 1689	5004	2004-02-28	D	I	V	19.9	18.8
Abell 1689	6930	2006-03-06	E	I	V	76.1	66.5
Abell 1689	7289	2006-03-09	E	I	V	75.1	69.0
Abell 1689	7701	2007-03-07	E	I	V	5.0	5.0
Abell 209	522	2000-09-09	C	I	V⋆	10.0	9.2
Abell 209	3579	2003-08-03	D	I	V	10.0	9.0
Abell 2104	895	2000-05-25	C	S	F	49.2	47.1
Abell 2163	545	2000-07-29	C	I	V⋆	9.4	7.9
Abell 2163	1653	2001-06-16	D	I	V	71.1	54.5
Abell 2420	8271	2007-07-03	E	I	V	8.1	7.8
Abell 2426	12279	2010-09-20	E	I	V	9.6	9.4
Abell 2485	10439	2009-07-04	E	I	V	19.8	19.0
Abell 2537	4962	2004-09-09	D	S	V	36.2	35.2
Abell 2537	9372	2008-08-11	E	I	V	38.5	34.8
Abell 2597	922	2000-07-28	C	S	F	39.3	E
Abell 2597	6934	2006-05-01	E	S	V	52.2	52.2
Abell 2597	7329	2006-05-04	E	S	V	60.1	56.3
Abell 2645	11769	2009-08-18	E	S	V	5.0	5.0
Abell 2667	2214	2001-06-19	D	S	V	9.6	9.6
Abell 3112	2216	2001-05-24	D	S	V	7.3	5.1
Abell 3112	2516	2001-09-15	D	S	V	16.9	11.3
Abell 3112	6972	2006-04-18	E	I	V	29.8	12.3
Abell 3112	7323	2006-04-21	E	I	V	28.4	21.0
Abell 3112	7324	2006-04-23	E	I	V	25.4	23.5
Abell 3112	13135	2011-03-14	E	I	V	42.2	39.9
Abell 3158	3712	2002-06-19	D	I	V	31.0	28.7
Abell 3158	3201	2002-06-21	D	I	V	24.8	23.5
Abell 3158	7688	2007-09-16	E	I	V	5.0	5.0
Abell 3444	9400	2008-02-11	E	S	V	36.7	35.7
Abell 3695	12274	2010-08-17	E	I	V	9.9	9.9
Abell 3827	7920	2007-08-20	E	S	V	45.6	45.6
Abell 383	524	2000-09-08	C	I	V⋆	10.0	8.9
Abell 383	2320	2000-11-16	C	I	V⋆	19.3	18.7
Abell 383	2321	2000-11-16	C	S	F	19.5	17.4
Abell 3921	4973	2004-08-20	D	I	V	29.4	26.1
Abell 521	901	1999-12-23	B	I	V⋆	38.7	36.3
Abell 521	430	2000-10-13	C	S	V⋆	39.1	7.4
Abell 521	12880	2010-11-25	E	I	V	49.4	46.3
Abell 521	13190	2010-11-26	E	I	V	39.2	35.3

Table 2: continued

Cluster	ObsID	Date	B	D	M	exp.	gti
Abell 545	13998	2011-12-16	E	S	F	29.6	29.6
Abell 754	577	1999-10-30	B	I	F	44.2	25.6
Abell 754	6794	2006-01-27	E	I	V	9.9	9.1
Abell 754	10743	2009-02-17	E	I	V	94.1	88.0
Abell 907	535	2000-06-29	C	I	V⋆	11.0	10.2
Abell 907	3185	2002-06-14	D	I	V	48.0	41.9
Abell 907	3205	2002-10-30	D	I	V	47.1	31.5
Hydra	575	1999-10-30	B	I	F	23.9	9.5
Hydra	576	1999-11-02	B	S	F	19.5	17.4
Hydra	4969	2004-01-13	D	S	V	96.9	52.9
Hydra	4970	2004-10-22	D	S	V	98.8	92.7
RX J0043.4−2037	9409	2008-02-02	E	I	V	19.9	18.9
RX J0055.9−3732	9883	2008-07-08	E	S	V	10.1	10.1
RX J0105.5−2439	9410	2008-08-11	E	I	V	19.9	19.1
RX J0118.1−2658	9429	2008-08-30	E	I	V	19.7	17.4
RX J0220.9−3829	9411	2008-02-29	E	I	V	19.9	17.4
RX J0232.2−4420	4993	2004-06-08	D	I	V	23.4	4.9
RX J0237.4−2630	9412	2008-03-03	E	I	V	18.4	10.0
RX J0304.1−3656	9413	2008-03-16	E	I	V	19.9	17.8
RX J0307.0−2840	9414	2008-03-13	E	I	V	18.9	17.6
RX J0331.1−2100	9415	2008-10-09	E	I	V	9.9	9.4
RX J0331.1−2100	10790	2008-10-11	E	I	V	10.0	9.3
RX J0336.3−4037	9416	2009-04-08	E	I	V	20.1	19.5
RX J0449.9−4440	9417	2008-09-23	E	I	V	19.8	18.2
RX J0516.6−5430	9331	2009-03-05	E	I	V	9.5	8.5
RX J0528.9−3927	4994	2004-03-10	D	I	V	22.5	12.0
RX J0547.6−3152	9419	2008-07-04	E	I	V	19.8	17.9
RX J0638.7−5358	9420	2008-04-11	E	I	V	19.9	17.6
RX J1333.6−2317	12835	2011-02-08	E	I	V	5.0	5.0
RX J1459.4−1811	9428	2008-06-16	E	S	V	39.6	39.6
RX J1504.1−0248	4935	2004-01-07	D	I	F	13.3	9.2
RX J1504.1−0248	5793	2005-03-20	D	I	V	39.2	30.7
RX J1524.2−3154	9401	2008-01-07	E	S	V	40.9	40.9
RX J1558.3−1410	9402	2008-04-09	E	S	V	40.1	37.0
RX J2011.3−5725	4995	2004-06-08	D	I	V	24.0	19.2
RX J2014.8−2430	11757	2009-08-25	E	S	V	19.9	19.9
3C 196	12729	2011-02-11	E	S	V	7.9	7.9
Abell 2319	3231	2002-03-15	D	I	V	14.4	12.9
Abell 3628	13377	2011-12-18	E	I	V	8.9	8.2
Abell 644	2211	2001-03-26	D	I	V	29.7	26.4
PKS 0745−191	508	2000-08-28	C	S	F	28.0	E
PKS 0745−191	2427	2001-06-16	D	S	V	17.9	17.9
PKS 0745−191	6103	2004-09-24	D	I	V	10.3	9.2
PKS 0745−191	7694	2007-01-25	E	I	V	5.0	4.7
PKS 0745−191	12881	2011-01-27	E	S	V	118.1	117.0
3C 295	578	1999-08-30	A	S	F	18.8	15.4
3C 295	2254	2001-05-18	D	I	V	91.0	75.5
Abell 1576	7938	2007-08-22	E	I	V	15.0	13.7
Abell 1995	906_obi1	2000-05-08	C	S	F	45.6	42.5
Abell 1995	906_obi2	2000-07-29	C	S	F	11.9	11.9
Abell 1995	7021	2006-08-30	E	I	V	48.5	42.9
Abell 1995	7713	2008-01-24	E	I	V	7.1	6.7
Abell 2552	3288	2002-09-07	D	I	V	13.6	E
Abell 2552	11730	2009-08-06	E	I	V	22.7	20.9
Abell 2744	2212	2001-09-03	D	S	V	24.8	23.8
Abell 2744	7915	2006-11-08	E	I	V	18.6	17.9
Abell 2744	8477	2007-06-10	E	I	V	45.9	42.6
Abell 2744	8557	2007-06-14	E	I	V	27.8	25.5
Abell 2744	7712	2007-09-10	E	I	V	8.1	7.7
IRAS 09104+4109	509	1999-11-03	B	S	F	9.0	E
IRAS 09104+4109	10445	2009-01-06	E	I	V	76.2	69.0
MACS J0011.7−1523	3261	2002-11-20	D	I	V	21.6	17.8
MACS J0011.7−1523	6105	2005-06-28	D	I	V	37.3	32.4
MACS J0025.4−1222	3251	2002-11-11	D	I	V	19.3	18.1
MACS J0025.4−1222	5010	2004-08-09	D	I	V	24.8	20.0
MACS J0025.4−1222	10413	2008-10-16	E	I	V	75.6	71.3
MACS J0025.4−1222	10786	2008-10-18	E	I	V	14.1	13.4
MACS J0025.4−1222	10797	2008-10-21	E	I	V	23.9	22.8
MACS J0035.4−2015	3262	2003-01-22	D	I	V	21.4	18.5
MACS J0111.5+0855	3256	2002-11-20	D	I	V	19.4	14.5

Table 2: continued

Cluster	ObsID	Date	B	D	M	exp.	gti
MACS J0140.0−0555	5013	2004-06-04	D	I	V	10.2	8.9
MACS J0140.0−0555	12243	2010-09-15	E	I	V	19.3	18.4
MACS J0150.3−1005	11711	2009-09-14	E	I	V	26.8	26.1
MACS J0152.5−2852	3264	2002-09-17	D	I	V	17.5	14.7
MACS J0159.0−3412	5818	2006-02-19	E	I	V	9.4	8.7
MACS J0159.8−0849	3265	2002-10-02	D	I	V	17.9	14.6
MACS J0159.8−0849	6106	2004-12-04	D	I	V	35.3	31.0
MACS J0159.8−0849	9376	2008-10-03	E	I	V	19.5	17.2
MACS J0242.5−2132	3266	2002-02-07	D	I	V	11.9	7.7
MACS J0257.1−2325	1654	2000-10-03	C	I	F	19.8	18.8
MACS J0257.1−2325	3581	2003-08-23	D	I	V	18.5	15.9
MACS J0257.6−2209	3267	2001-11-12	D	I	V	20.5	18.4
MACS J0308.9+2645	3268	2002-03-10	D	I	V	24.4	20.2
MACS J0326.8−0043	5810	2005-10-30	E	I	V	9.9	8.9
MACS J0329.6−0211	3257	2001-11-25	D	I	V	9.9	E
MACS J0329.6−0211	3582	2002-12-24	D	I	V	19.8	16.6
MACS J0329.6−0211	6108	2004-12-06	D	I	V	39.6	E
MACS J0329.6−0211	7719	2006-12-03	E	I	V	7.1	5.0
MACS J0358.8−2955	11719	2009-10-18	E	I	V	9.6	9.6
MACS J0358.8−2955	12300	2010-11-26	E	I	V	29.7	27.1
MACS J0358.8−2955	13194	2010-11-28	E	I	V	20.0	12.8
MACS J0404.2−2703	10448	2009-05-13	E	I	V	22.7	20.2
MACS J0404.6+1109	3269	2002-02-20	D	I	V	21.8	18.0
MACS J0416.1−2403	10446	2009-06-07	E	I	V	15.8	14.6
MACS J0417.5−1154	3270	2002-03-10	D	I	V	12.0	10.0
MACS J0417.5−1154	11759	2009-10-28	E	I	V	51.4	47.5
MACS J0417.5−1154	12010	2009-10-29	E	I	V	25.8	24.5
MACS J0429.6−0253	3271	2002-02-07	D	I	V	23.2	19.3
MACS J0451.9+0006	5815	2005-01-08	D	I	V	10.2	9.7
MACS J0455.2+0657	5812	2005-01-08	D	I	V	9.9	8.9
MACS J0520.7−1328	3272	2002-02-10	D	I	V	19.2	16.4
MACS J0547.0−3904	3273	2002-10-20	D	I	V	21.7	18.7
MACS J0553.4−3342	5813	2005-01-08	D	I	V	9.9	9.2
MACS J0553.4−3342	12244	2011-06-23	E	I	V	74.1	64.5
MACS J0647.7+7015	3196	2002-10-31	D	I	V	19.3	16.6
MACS J0647.7+7015	3584	2003-10-07	D	I	V	20.0	16.6
MACS J0712.3+5931	11709	2010-12-27	E	I	V	25.7	23.2
MACS J0717.5+3745	1655	2001-01-29	D	I	F	19.9	16.3
MACS J0717.5+3745	4200	2003-01-08	D	I	V	59.2	48.4
MACS J0744.8+3927	3197	2001-11-12	D	I	V	20.2	17.1
MACS J0744.8+3927	3585	2003-01-04	D	I	V	19.9	15.6
MACS J0744.8+3927	6111	2004-12-03	D	I	V	49.5	41.4
MACS J0911.2+1746	3587	2003-02-23	D	I	V	17.9	15.8
MACS J0911.2+1746	5012	2004-03-08	D	I	V	23.8	21.2
MACS J0940.9+0744	11712	2010-01-07	E	I	V	26.9	25.1
MACS J0947.2+7623	2202	2000-10-20	C	I	V⋆	11.7	10.5
MACS J0947.2+7623	7902	2007-07-09	E	S	V	38.3	38.3
MACS J0949.8+1708	3274	2002-11-06	D	I	V	14.3	12.0
MACS J1006.9+3200	5819	2005-01-24	D	I	V	10.9	10.2
MACS J1105.7−1014	5817	2005-01-03	D	I	V	10.3	9.6
MACS J1108.8+0906	3252	2002-11-17	D	I	V	9.9	8.7
MACS J1108.8+0906	5009	2004-02-20	D	I	V	24.5	18.4
MACS J1115.2+5320	3253	2002-03-23	D	I	V	8.8	7.4
MACS J1115.2+5320	5008	2004-06-22	D	I	V	18.0	15.2
MACS J1115.2+5320	5350	2004-07-28	D	I	V	6.9	E
MACS J1115.8+0129	3275	2003-01-23	D	I	V	15.9	9.5
MACS J1115.8+0129	9375	2008-02-03	E	I	V	39.6	35.0
MACS J1131.8−1955	3276	2002-06-14	D	I	V	13.9	5.9
MACS J1149.5+2223	1656	2001-06-01	D	I	V	18.5	15.6
MACS J1149.5+2223	3589	2003-02-07	D	I	V	20.0	16.7
MACS J1206.2−0847	3277	2002-12-15	D	I	V	23.5	20.4
MACS J1218.4+4012	10447	2009-02-28	E	I	V	18.9	17.6
MACS J1226.8+2153	3590	2003-12-13	D	I	V	19.0	13.9
MACS J1226.8+2153	12878	2011-04-11	E	I	V	130.2	112.6
MACS J1311.0−0310	3258	2002-12-15	D	I	V	14.9	E
MACS J1311.0−0310	6110	2005-04-20	D	I	V	63.2	55.8
MACS J1311.0−0310	7721	2007-03-03	E	I	V	7.1	6.5
MACS J1311.0−0310	9381	2007-12-09	E	I	V	29.7	26.9
MACS J1319.9+7003	3278	2002-09-15	D	I	V	21.6	E
MACS J1354.6+7715	11754	2010-06-26	E	I	V	32.6	30.3

Table 2: continued

Cluster	ObsID	Date	B	D	M	exp.	gti
MACS J1359.1−1929	5811	2005-03-17	D	I	V	9.9	8.9
MACS J1359.1−1929	9378	2008-03-21	E	I	V	49.4	45.5
MACS J1423.8+2404	1657	2001-06-01	D	I	V	18.5	16.2
MACS J1423.8+2404	4195	2003-08-18	D	S	V	115.6	106.5
MACS J1427.2+4407	6112	2005-02-12	D	I	V	9.4	8.4
MACS J1427.2+4407	9380	2008-01-14	E	I	V	25.8	23.3
MACS J1427.2+4407	9808	2008-01-15	E	I	V	14.9	13.1
MACS J1427.2+4407	11694	2010-10-09	E	S	F	6.0	6.0
MACS J1427.6−2521	3279	2002-06-29	D	I	V	16.9	14.1
MACS J1427.6−2521	9373	2008-06-11	E	I	V	28.4	27.1
MACS J1532.8+3021	1649	2001-08-26	D	S	V	9.4	9.2
MACS J1532.8+3021	1665	2001-09-06	D	I	V	10.0	8.2
MACS J1532.8+3021	14009	2011-11-16	E	S	V	88.9	84.8
MACS J1621.3+3810	3254	2002-10-18	D	I	V	9.8	8.3
MACS J1621.3+3810	3594	2003-08-22	D	I	V	19.7	E
MACS J1621.3+3810	6109	2004-12-11	D	I	V	37.5	32.7
MACS J1621.3+3810	6172	2004-12-25	D	I	V	29.8	26.4
MACS J1621.3+3810	7720	2007-11-08	E	I	V	7.1	5.8
MACS J1621.3+3810	9379	2008-10-17	E	I	V	29.9	28.9
MACS J1621.3+3810	10785	2008-10-18	E	I	V	29.8	27.4
MACS J1720.2+3536	3280	2002-11-03	D	I	V	20.8	18.0
MACS J1720.2+3536	6107	2005-11-22	E	I	V	33.9	27.5
MACS J1720.2+3536	7225	2005-11-27	E	I	V	2.0	E
MACS J1720.2+3536	7718	2007-09-28	E	I	V	7.0	5.9
MACS J1731.6+2252	3281	2002-11-03	D	I	V	20.5	18.7
MACS J1931.8−2634	3282	2002-10-20	D	I	V	13.6	11.8
MACS J1931.8−2634	9382	2008-08-21	E	I	V	98.9	91.8
MACS J2046.0−3430	5816	2005-06-28	D	I	V	10.0	8.4
MACS J2046.0−3430	9377	2008-06-27	E	I	V	39.2	34.9
MACS J2049.9−3217	3283	2002-12-08	D	I	V	23.8	19.7
MACS J2129.4−0741	3199	2002-12-23	D	I	V	19.9	9.2
MACS J2129.4−0741	3595	2003-10-18	D	I	V	19.9	16.5
MACS J2135.2−0102	11710	2009-09-09	E	I	V	26.7	24.4
MACS J2211.7−0349	3284	2002-10-08	D	I	V	17.7	12.9
MACS J2214.9−1359	3259	2002-12-22	D	I	V	19.5	13.8
MACS J2214.9−1359	5011	2003-11-17	D	I	V	18.5	11.6
MACS J2228.5+2036	3285	2003-01-22	D	I	V	19.9	16.3
MACS J2229.7−2755	3286	2002-11-13	D	I	V	16.4	11.5
MACS J2229.7−2755	9374	2007-12-09	E	I	V	14.8	13.8
MACS J2243.3−0935	3260	2002-12-23	D	I	V	20.5	15.4
MACS J2245.0+2637	3287	2002-11-24	D	I	V	16.9	12.3
MS 0015.9+1609	520	2000-08-18	C	I	V⋆	67.4	61.0
MS 0451.6−0305	529	2000-01-14	B	I	V⋆	14.0	12.7
MS 0451.6−0305	902	2000-10-08	C	S	F	44.2	33.8
MS 2137.3−2353	928	1999-11-18	B	S	V⋆	43.6	23.3
MS 2137.3−2353	4974	2003-11-13	D	S	V	57.4	E
MS 2137.3−2353	5250	2003-11-18	D	S	V	40.5	27.6
RX J0027.6+2616	3249	2002-06-26	D	I	V	10.0	8.7
RX J1347.5−1145	506	2000-03-05	C	S	V⋆	8.9	8.2
RX J1347.5−1145	507	2000-04-29	C	S	F	10.0	10.0
RX J1347.5−1145	3592	2003-09-03	D	I	V	57.7	48.9
RX J2003.5−2323	7916	2007-09-02	E	I	V	49.5	44.4
Zwicky 1358	516	2000-09-03	C	S	F	54.1	23.6
Zwicky 1358	7714	2007-08-25	E	I	V	7.0	7.0
Zwicky 1953	1659	2000-10-22	C	I	F	24.9	15.6
Zwicky 1953	7716	2006-12-20	E	I	V	7.0	6.5
3C 288	9275	2008-04-13	E	S	V	39.6	38.6
3C 88	9391	2008-06-30	E	I	V	11.1	10.1
3C 88	11977	2009-10-06	E	S	V	49.6	49.6
3C 88	11751	2009-10-14	E	S	V	19.9	19.9
3C 88	12007	2009-10-15	E	S	V	34.6	34.6
Abell 1775	12891	2011-07-31	E	S	V	39.5	39.5
Abell 1775	13510	2011-08-12	E	S	V	59.3	58.2
Abell 744	6947	2006-10-22	E	I	V	39.5	32.5
CL J0030+2618	1190	1999-08-17	A	S	F	24.4	E
CL J0030+2618	1226	1999-08-17	A	S	F	24.4	E
CL J0030+2618	1268	1999-08-17	A	S	F	3.4	E
CL J0030+2618	5762	2005-05-28	D	I	V	17.9	11.0
CL J0057−2616	9427	2008-06-22	E	I	V	10.0	9.5
CL J0106+3209	2147	2000-11-06	C	S	F	44.4	39.3

Cluster	ObsID	Date	B	D	M	exp.	gti
CL J0106+3209	3555	2003-08-06	D	S	F	5.1	5.1
CL J0124+0932	6778	2006-08-29	E	S	V	13.7	8.1
CL J0141−3034	5778	2005-06-04	D	I	V	29.7	25.3
CL J0152−1357	913	2000-09-08	C	I	F	36.5	31.9
CL J0159+0030	5777	2005-09-02	E	I	V	19.9	18.1
CL J0216−1747	5760	2005-09-07	E	I	V	40.0	8.7
CL J0216−1747	6393	2005-10-04	E	I	V	26.6	21.8
CL J0230+1836	5754	2004-11-05	D	I	V	67.8	61.4
CL J0237−5224	9392	2008-02-28	E	I	V	13.9	12.9
CL J0245+0936	9394	2007-12-02	E	I	V	15.0	14.1
CL J0302−0423	5782	2005-12-07	E	I	V	10.0	9.0
CL J0306−0943	9389	2007-11-18	E	I	V	10.0	8.8
CL J0318−0302	5775	2005-03-15	D	I	V	14.6	11.8
CL J0328−2140	5755	2005-03-15	D	I	V	43.3	39.4
CL J0328−2140	6258	2005-03-18	D	I	V	13.1	7.9
CL J0333−2456	5764	2005-04-05	D	I	V	43.6	26.1
CL J0334−3900	9393	2009-05-07	E	I	V	15.6	14.3
CL J0336−2804	9390	2008-08-30	E	I	V	10.6	9.4
CL J0340−2823	5780	2006-01-15	E	I	V	24.7	21.8
CL J0340−2840	9385	2008-10-28	E	I	V	9.6	9.6
CL J0350−3801	7227	2006-03-19	E	I	V	24.7	20.7
CL J0355−3741	5761	2006-01-12	E	I	V	27.7	24.3
CL J0405−4100	5756	2005-10-27	E	I	V	7.9	6.9
CL J0405−4100	7191	2006-05-19	E	I	V	69.2	61.8
CL J0422−5009	11866	2010-02-22	E	S	V	14.9	14.9
CL J0521−2530	3432	2002-01-30	D	S	F	14.9	12.3
CL J0521−2530	6173	2004-12-18	D	I	V	4.9	4.9
CL J0521−2530	4928	2004-12-19	D	I	V	14.0	12.4
CL J0521−2530	5758	2005-01-07	D	I	V	15.0	13.7
CL J0522−3624	4926	2004-06-17	D	I	V	18.5	16.4
CL J0522−3624	5837	2006-02-02	E	I	V	27.7	25.6
CL J0542−4100	914	2000-07-26	C	I	F	50.4	44.8
CL J0809+2811	5774	2004-11-30	D	I	V	19.7	5.4
CL J0838+1948	9397	2007-12-22	E	I	V	19.9	17.6
CL J0853+5759	4925	2004-09-19	D	I	V	17.8	13.8
CL J0853+5759	5765	2005-02-19	D	I	V	24.6	22.8
CL J0900+3920	6862	2006-01-26	E	S	F	14.9	13.9
CL J0900+3920	11299	2009-12-18	E	S	V	4.8	4.8
CL J0926+1242	4929	2004-02-06	D	I	V	18.6	15.0
CL J0926+1242	5838	2005-02-21	D	I	V	31.4	28.4
CL J0953+6947	361	1999-09-20	B	I	V⋆	33.2	31.3
CL J0953+6947	1302	1999-09-20	B	I	V⋆	15.5	15.1
CL J0953+6947	379	2000-03-11	C	I	V⋆	8.9	8.4
CL J0953+6947	10544	2009-07-07	E	S	V	73.5	72.5
CL J0953+6947	10925	2009-07-07	E	S	V	44.5	44.5
CL J0956+4107	4930	2003-12-29	D	I	V	1.7	1.7
CL J0956+4107	5294	2003-12-30	D	I	V	17.3	15.4
CL J0956+4107	5759	2005-01-28	D	I	V	40.2	34.0
CL J0958+4702	5779	2005-02-19	D	I	V	25.2	21.1
CL J1002+6858	5773	2005-01-05	D	I	V	19.8	17.4
CL J1003+3253	5776	2005-03-11	D	I	V	19.9	18.6
CL J1058+0136	9387	2008-03-28	E	I	V	10.1	9.5
CL J1116+1803	2073	2001-06-12	D	I	V	38.5	32.4
CL J1117+1744	4933	2004-06-18	D	I	V	18.8	16.5
CL J1117+1744	5836	2005-02-15	D	I	V	45.2	38.4
CL J1120+2326	1660	2001-04-23	D	I	V	71.2	58.5
CL J1120+4318	5771	2005-01-11	D	I	V	19.8	18.0
CL J1202+5751	4975	2004-09-29	D	S	V	58.4	52.2
CL J1202+5751	5757	2005-09-02	E	I	V	59.0	43.4
CL J1202+5751	7893	2007-07-29	E	I	V	5.0	5.0
CL J1206−0744	9388	2007-11-15	E	I	V	10.0	9.7
CL J1212+2733	5767	2005-03-17	D	I	V	14.6	12.0
CL J1213+0253	4934	2004-07-17	D	I	V	18.9	16.1
CL J1217+4729	350	2000-04-17	C	S	F	14.0	12.3
CL J1220+7522	11778	2010-12-11	E	S	F	29.8	28.8
CL J1221+4918	1662	2001-08-05	D	I	V	79.1	62.9
CL J1222+2709	5766	2005-03-12	D	I	V	49.1	41.7
CL J1226+3332	932	2000-07-31	C	S	V⋆	9.8	7.8
CL J1226+3332	3180	2003-01-27	D	I	V	31.7	28.4
CL J1226+3332	5014	2004-08-07	D	I	V	32.7	28.4

Cluster	ObsID	Date	B	D	M	exp.	gti
CL J1231+4137	4726	2004-11-20	D	S	V	39.6	36.6
CL J1236+1224	8098	2008-02-24	E	S	F	5.1	5.1
CL J1248−0548	784	2000-01-15	B	S	F	39.3	38.2
CL J1248−0548	4727	2003-12-26	D	S	V	39.9	35.8
CL J1248−0548	4728	2004-01-06	D	S	V	35.7	17.3
CL J1248−0548	4729	2004-02-12	D	S	V	38.1	E
CL J1248−0548	4730	2004-08-18	D	S	V	40.0	33.9
CL J1259+3120	9395	2008-03-24	E	I	V	17.9	15.9
CL J1312+3900	5781	2005-04-08	D	I	V	26.4	12.0
CL J1329+1143	3216	2002-12-10	D	S	V	34.7	31.6
CL J1334+5031	5772	2005-08-05	D	I	V	19.5	9.5
CL J1349+4918	9396	2009-03-03	E	I	V	18.4	17.3
CL J1354−0221	4932	2004-12-07	D	I	V	17.4	15.6
CL J1354−0221	5835	2005-05-17	D	I	V	37.7	32.8
CL J1416+4446	541	1999-12-02	B	I	V⋆	31.2	25.8
CL J1524+0957	1664	2002-04-01	D	I	V	50.9	42.2
CL J1533+3108	9384	2007-11-13	E	I	V	10.0	8.2
CL J1537+1200	5591	2005-04-10	D	S	V	35.6	32.8
CL J1630+2434	9386	2007-12-22	E	I	V	9.6	8.9
CL J1641+4001	3575	2003-09-24	D	I	V	46.5	38.1
CL J1701+6414	547	2000-10-31	C	I	V⋆	49.5	45.7
CL J1701+6414	8032	2007-11-12	E	I	V	31.0	27.4
CL J1701+6414	9757	2007-11-13	E	I	V	20.8	16.1
CL J1701+6414	9756	2007-11-14	E	I	V	32.3	28.2
CL J1701+6414	9758	2007-11-16	E	I	V	23.4	22.3
CL J1701+6414	9759	2007-11-17	E	I	V	31.2	29.4
CL J1701+6414	9760	2007-11-19	E	I	V	17.0	15.1
CL J1701+6414	8033	2007-11-20	E	I	V	29.7	26.4
CL J1701+6414	9767	2007-11-21	E	I	V	9.0	7.0
CL J1807+6946	841	2000-03-21	C	S	F	10.1	10.1
CL J2137+0027	11796	2009-09-16	E	S	V	24.8	24.8
CL J2220−5228	9383	2008-08-19	E	I	V	10.0	9.2
CL J2318−4235	436	2000-10-14	C	S	V⋆	13.4	0.0
CL J2318−4235	2319	2000-10-15	C	S	V⋆	5.9	3.8
RX J1159+5531	910	1999-12-06	B	I	V⋆	18.9	13.8
RX J1159+5531	4964	2004-02-11	D	S	V	75.1	66.9
RX J1340+4018	3223	2002-08-28	D	S	V	47.0	34.7
RX J1552+2013	3214	2002-05-18	D	S	V	14.9	14.9
RX J1552+2013	10242	2009-05-07	E	I	V	18.3	18.3
RX J1552+2013	10908	2009-05-10	E	I	V	27.5	24.8
RX J2247+0337	911	2000-05-11	C	I	F	49.0	44.6
SPT-CL J0000−5748	9335	2009-03-16	E	I	V	30.1	28.4
SPT-CL J0013−4906	13462	2011-10-18	E	I	V	14.1	13.0
SPT-CL J0014−4952	13471	2012-08-11	E	I	V	55.2	48.1
SPT-CL J0037−5047	13493	2012-08-20	E	I	V	73.0	63.5
SPT-CL J0040−4407	13395	2011-09-08	E	I	V	7.9	7.7
SPT-CL J0058−6145	13479	2012-01-05	E	I	V	50.6	46.7
SPT-CL J0102−4603	13485	2012-02-24	E	I	V	60.7	54.0
SPT-CL J0106−5943	13468	2012-10-20	E	I	V	17.6	14.6
SPT-CL J0123−4821	13491	2012-09-15	E	I	V	71.1	58.8
SPT-CL J0142−5032	13467	2012-12-29	E	I	V	29.1	24.3
SPT-CL J0151−5954	13480	2012-01-07	E	I	V	49.4	45.3
SPT-CL J0151−5954	14380	2012-01-14	E	I	V	31.6	28.3
SPT-CL J0156−5541	13489	2012-03-03	E	I	V	77.6	67.7
SPT-CL J0200−4852	13487	2013-01-04	E	I	V	23.5	20.4
SPT-CL J0212−4656	13464	2013-01-14	E	I	V	28.0	24.4
SPT-CL J0256−5617	13481	2012-06-24	E	I	V	21.8	18.4
SPT-CL J0256−5617	14448	2012-06-25	E	I	V	25.6	22.6
SPT-CL J0307−5042	13476	2012-09-28	E	I	V	39.6	24.5
SPT-CL J0307−6225	12191	2010-08-07	E	I	V	24.7	21.9
SPT-CL J0324−6236	12181	2010-09-04	E	I	V	19.5	16.9
SPT-CL J0324−6236	13137	2011-01-10	E	I	V	23.7	22.2
SPT-CL J0324−6236	13213	2011-01-12	E	I	V	11.7	10.9
SPT-CL J0334−4659	13470	2012-12-19	E	I	V	25.7	23.2
SPT-CL J0352−5647	13490	2012-10-24	E	I	V	35.2	31.9
SPT-CL J0352−5647	15571	2012-10-26	E	I	V	9.9	7.2
SPT-CL J0411−4819	13396	2011-10-28	E	I	V	8.0	5.9
SPT-CL J0426−5455	13472	2012-12-21	E	I	V	32.4	28.3
SPT-CL J0441−4854	14371	2011-12-09	E	I	V	20.8	18.0
SPT-CL J0441−4854	14372	2011-12-09	E	I	V	23.8	21.2

Cluster	ObsID	Date	B	D	M	exp.	gti
SPT-CL J0441−4854	13475	2011-12-10	E	I	V	24.7	21.5
SPT-CL J0446−5849	13482	2012-10-11	E	I	V	32.9	29.4
SPT-CL J0446−5849	15560	2012-10-14	E	I	V	20.7	17.1
SPT-CL J0449−4901	13473	2012-06-29	E	I	V	51.0	44.8
SPT-CL J0456−5116	13474	2012-05-08	E	I	V	50.2	44.6
SPT-CL J0509−5342	9432	2009-06-03	E	I	V	28.8	26.7
SPT-CL J0528−5300	9341	2009-01-26	E	I	V	14.8	14.3
SPT-CL J0528−5300	10862	2009-02-14	E	I	V	12.6	11.8
SPT-CL J0528−5300	11996	2010-01-12	E	I	V	9.9	9.2
SPT-CL J0528−5300	11874	2010-07-01	E	I	V	29.7	27.6
SPT-CL J0528−5300	12092	2010-08-08	E	I	V	19.8	18.5
SPT-CL J0528−5300	11747	2010-09-18	E	I	V	19.1	17.8
SPT-CL J0528−5300	13126	2010-09-18	E	I	V	18.3	16.0
SPT-CL J0547−5345	9332	2009-01-09	E	I	V	14.9	13.8
SPT-CL J0547−5345	10851	2009-02-01	E	I	V	8.5	8.2
SPT-CL J0547−5345	10864	2009-02-04	E	I	V	5.8	5.5
SPT-CL J0547−5345	9336	2009-05-04	E	I	V	28.2	27.4
SPT-CL J0547−5345	11739	2010-07-04	E	I	V	12.8	11.5
SPT-CL J0552−5709	11871	2009-11-10	E	I	V	19.8	18.7
SPT-CL J0552−5709	11743	2010-08-25	E	I	V	16.4	15.6
SPT-CL J0559−5249	12264	2010-08-31	E	I	V	40.0	35.4
SPT-CL J0559−5249	13116	2010-09-01	E	I	V	24.5	22.9
SPT-CL J0559−5249	13117	2010-09-03	E	I	V	44.0	39.2
SPT-CL J0655−5234	13486	2012-02-25	E	I	V	20.2	16.4
SPT-CL J2034−5936	12182	2011-08-16	E	I	V	58.9	51.7
SPT-CL J2035−5251	13466	2011-11-24	E	I	V	18.6	17.1
SPT-CL J2043−5035	13478	2011-08-10	E	I	V	79.4	73.8
SPT-CL J2106−5844	12180	2010-11-20	E	I	V	24.7	22.7
SPT-CL J2145−5644	13398	2011-07-12	E	I	V	14.9	12.3
SPT-CL J2146−4632	13469	2011-12-12	E	I	V	81.0	68.8
SPT-CL J2218−4519	13501	2012-09-01	E	I	V	34.8	28.7
SPT-CL J2222−4834	13497	2012-12-26	E	I	V	32.5	26.9
SPT-CL J2232−6000	13502	2012-01-05	E	I	V	31.8	28.0
SPT-CL J2233−5339	13504	2012-01-06	E	I	V	17.0	14.2
SPT-CL J2236−4555	15266	2012-08-15	E	I	V	35.6	30.5
SPT-CL J2236−4555	13507	2012-08-19	E	I	V	47.7	40.2
SPT-CL J2258−4044	13495	2012-08-22	E	I	V	54.4	47.7
SPT-CL J2259−6057	13498	2011-12-31	E	I	V	64.5	55.8
SPT-CL J2301−4023	13505	2012-08-17	E	I	V	59.0	47.7
SPT-CL J2325−4111	13405	2011-08-14	E	I	V	8.9	7.7
SPT-CL J2331−5051	9333	2009-08-12	E	I	V	28.7	26.4
SPT-CL J2331−5051	11738	2009-08-30	E	I	V	5.9	5.4
SPT-CL J2335−4544	13496	2013-01-15	E	I	V	20.7	18.1
SPT-CL J2337−5942	11859	2010-01-10	E	I	V	19.8	18.9
SPT-CL J2341−5119	11799	2009-08-01	E	I	V	50.3	48.0
SPT-CL J2341−5119	9345	2009-08-02	E	I	V	29.6	27.8
SPT-CL J2343−5411	11741	2009-08-31	E	I	V	62.7	58.1
SPT-CL J2343−5411	11870	2009-10-20	E	I	V	19.8	18.8
SPT-CL J2343−5411	12014	2010-01-21	E	I	V	54.3	50.5
SPT-CL J2343−5411	12091	2010-03-12	E	I	V	37.7	34.9
SPT-CL J2344−4242	13401	2011-09-19	E	I	V	11.9	10.7
SPT-CL J2345−6406	13500	2012-08-15	E	I	V	65.2	55.7
SPT-CL J2352−4657	13506	2012-08-30	E	I	V	79.4	66.0
SPT-CL J2356−5056	11746	2009-09-06	E	I	V	11.5	11.2
SPT-CL J2356−5056	11998	2010-01-26	E	I	V	10.0	9.2
SPT-CL J2359−5009	9334	2009-03-12	E	I	V	29.8	19.8
SPT-CL J2359−5009	11742	2009-08-29	E	I	V	22.5	20.7
SPT-CL J2359−5009	11864	2009-09-07	E	I	V	19.7	17.4
SPT-CL J2359−5009	11997	2010-08-26	E	I	V	63.2	55.8
3C 186	3098	2002-05-16	D	S	V	34.4	16.9
3C 186	9407	2007-12-03	E	S	V	66.3	66.3
3C 186	9774	2007-12-06	E	S	V	75.1	75.1
3C 186	9775	2007-12-08	E	S	V	15.9	15.9
3C 186	9408	2007-12-11	E	S	V	39.6	39.6
CL J1415+3612	4163	2003-09-16	D	I	V	89.2	73.8
CL J1415+3612	12256	2010-08-28	E	S	V	118.5	115.4
CL J1415+3612	12255	2010-08-30	E	S	V	60.4	60.4
CL J1415+3612	13118	2010-09-01	E	S	V	44.6	44.6
CL J1415+3612	13119	2010-09-05	E	S	V	54.3	54.3
MS 1137.5+6625	536	1999-09-30	B	I	V⋆	117.3	110.0

Table 3: ROSAT data used in this work: [1] cluster name [2] observation ID; [3] date of observation; [4] nominal exposure length, ks.

Cluster	ObsID	Date	exp.
Abell 119	rp800251n00	1992-07-11	14.7
Abell 133	rp800319n00	1992-07-05	18.7
Abell 1651	rp800353n00	1992-07-18	7.2
Abell 1795	rp700145a00	1991-07-01	17.7
Abell 1795	rp800055n00	1991-07-01	25.0
Abell 1795	rp800105n00	1992-01-04	35.1
Abell 1795	rp700145a01	1992-01-06	1.9
Abell 2029	rp800249n00	1992-08-10	12.1
Abell 2063	rp800376n00	1992-08-14	6.8
Abell 2063	rp800128n00	1992-08-15	9.6
Abell 2063	rp800184a01	1992-08-16	9.4
Abell 2142	rp150084n00	1990-07-20	7.5
Abell 2142	rp800415n00	1992-08-21	18.6
Abell 2142	rp800096n00	1992-08-25	6.0
Abell 2142	rp800233n00	1992-08-26	4.8
Abell 2142	rp800551n00	1993-07-23	5.8
Abell 2199	rp150083n00	1990-07-18	10.2
Abell 2199	rp800644n00	1993-07-25	39.5
Abell 2199	rp701507n00	1993-07-30	5.0
Abell 2244	rp200527n00	1992-01-29	1.7
Abell 2244	rp201079n00	1992-09-02	6.1
Abell 2244	rp800265n00	1992-09-21	2.9
Abell 2255	rp800512n00	1993-08-24	14.0
Abell 2256	rp100110n00	1990-06-17	16.6
Abell 2256	rp800162a00	1991-10-15	4.1
Abell 2256	rp800163n00	1991-11-25	10.3
Abell 2256	rp800162a01	1992-04-15	4.6
Abell 2256	rp800339n00	1992-07-22	4.8
Abell 2256	rp800341n00	1992-07-23	10.1
Abell 2256	rp800340n00	1992-07-25	9.1
Abell 2319	rp800073a01	1992-11-02	3.1
Abell 2597	rp800112n00	1991-11-27	6.9
Abell 2734	rp600426n00	1992-12-20	4.6
Abell 3112	rp800302n00	1992-12-17	7.4
Abell 3158	rp800310n00	1992-08-26	2.9
Abell 3266	rp800211n00	1992-04-30	7.1
Abell 3266	rp800552n00	1993-08-19	13.2
Abell 3376	rp800154n00	1992-02-28	11.7
Abell 3391	rp800079n00	1991-04-24	2.6
Abell 3391	rp800080n00	1992-04-03	6.5
Abell 3530	rp701155n00	1993-01-28	8.3
Abell 3558	rp800076n00	1991-07-17	28.5
Abell 3558	rp800416a01	1993-01-18	14.1
Abell 3562	rp800237n00	1993-01-19	19.5
Abell 3571	rp800287n00	1992-08-12	5.8
Abell 3627	rp800382n00	1992-09-23	1.6
Abell 3627	rp800382a01	1993-03-13	10.9
Abell 3667	rp800234n00	1992-10-09	12.1
Abell 3921	rp800378n00	1992-11-15	11.6
Abell 3921	rp800467n00	1993-10-11	11.2
Abell 3921	rp800467a01	1994-05-01	4.6
Abell 399, 401	rp800182n00	1992-01-23	6.5
Abell 399, 401	rp800235n00	1992-07-30	7.2
Abell 401	rp180248n00	1998-02-18	2.6
Abell 401	rp180249n00	1998-02-19	1.9
Abell 401	rp180250n00	1998-02-19	1.3
Abell 4059	rp800175n00	1991-11-21	5.3
Abell 478	rp800193n00	1991-08-31	21.4
Abell 496	rp800024n00	1991-03-06	8.6
Abell 644	rp800379n00	1993-04-27	9.9
Abell 754	rp800160n00	1991-11-19	2.2
Abell 754	rp600451n00	1992-11-03	13.0
Abell 754	rp800232n00	1992-11-10	6.2
Abell 754	rp800550n00	1993-11-06	7.9
Abell 780	rp800318n00	1992-11-08	17.8

Table 3: continued

Cluster	ObsID	Date	exp.
Abell 85	rp800174a00	1991-12-20	2.1
Abell 85	rp800174a01	1992-06-11	3.3
Abell 85	rp800250n00	1992-07-01	9.9
AWM 7	rp800168n00	1992-01-28	12.7
Coma	rp800006n00	1991-06-16	20.8
Coma	rp800009n00	1991-06-16	19.7
Coma	rp800005n00	1991-06-17	20.4
Coma	rp800013n00	1991-06-18	20.7
Cygnus A	rp701152n00	1992-11-06	3.9
Cygnus A	rp800622n00	1993-10-10	9.1
Hydra A	rp800318n00	1992-11-08	17.8
Ophiuchus	rp300214n00	1992-09-20	13.5
Ophiuchus	rp800279n00	1992-09-20	3.8
Perseus	rp800033n00	1991-02-09	14.6
Perseus	rp800034a00	1991-02-09	9.9
Perseus	rp800035a00	1991-02-09	5.8
Perseus	rp800035a01	1991-08-18	23.7
Perseus	rp800034a01	1991-08-19	23.3
Perseus	rp800032a01	1991-09-02	29.6
Perseus	rp800186n00	1992-02-02	4.5
PKS 0745−191	rp800623n00	1993-10-15	10.1
RX J2344.2−0422	rp800333n00	1992-06-17	4.8
RX J2344.2−0422	rp800333a01	1992-12-09	9.8
Triangulum	rp800280n00	1992-09-26	7.1
Zwicky 5029	rp600166n00	1991-12-14	12.3

Table 4: Continuation of Table 1.

Cat.	Name	Obs.	flags	s	p	a	Rel.	ellip.	RA$_X$	Dec$_X$	RA$_{BCG}$	Dec$_{BCG}$
B	Abell 1763	C	l	0.686±0.097	−1.223±0.076	0.83±0.05		0.361±0.015	203.8230	41.0011	203.8337	41.0011
B	Abell 1795	C	a	0.780±0.008	−0.856±0.004	1.39±0.02		0.247±0.003	207.2192	26.5913	207.2188	26.5929
B	Abell 1835	C	alp$f$	1.160±0.020	−0.636±0.010	1.56±0.04	√	0.122±0.007	210.2583	2.8783	210.2586	2.8785
B	Abell 1914	C		0.518±0.029	−1.070±0.018	1.26±0.10		0.171±0.013	216.5121	37.8245	216.4861	37.8165
B	Abell 2009	C	l	1.078±0.061	−0.895±0.029	1.21±0.10		0.236±0.013	225.0817	21.3695	225.0813	21.3694
B	Abell 2029	C	af	1.200±0.098	−0.790±0.005	1.19±0.14	√	0.198±0.014	227.7333	5.7445	227.7338	5.7448
B	Abell 2034	C		1.029±0.072	−1.653±0.366	1.07±0.04		0.145±0.008	227.5532	33.5120	227.5488	33.4865
B	Abell 2065	C		0.514±0.029	−1.119±0.020	0.70±0.09		0.294±0.015	230.6219	27.7071	230.6216	27.7076
B	Abell 2069	C			−1.866				231.0326	29.8845	231.0309	29.8890
B	Abell 2111	C		0.583±0.131	−1.535±0.359	0.65±0.22		0.376±0.035	234.9242	34.4167	234.9187	34.4242
B	Abell 2142	C		0.906±0.015	−1.003±0.011	0.82±0.02		0.351±0.006	239.5855	27.2303	239.5833	27.2334
B	Abell 2204	C	alp$f$	1.638±0.063	−0.607±0.012	1.55±0.06	√	0.179±0.006	248.1951	5.5757	248.1956	5.5758
B	Abell 2218	C		0.834±0.098	−1.356±0.174	1.34±0.06		0.213±0.012	248.9625	66.2105		
B	Abell 2219	C		0.931±0.081	−1.079±0.010	1.46±0.15		0.260±0.014	250.0827	46.7109	250.0826	46.7115
B	Abell 2244	C		1.197±0.097	−0.996±0.006	1.15±0.13		0.133±0.014	255.6773	34.0609	255.6770	34.0600
B	Abell 2255	C		1.006±0.186	−1.911±0.551	1.32±0.16		0.171±0.012	258.2055	64.0654	258.1199	64.0607
B	Abell 2256	C		0.636±0.058	−1.513±0.395	1.10±0.03		0.301±0.018	256.0256	78.6514	256.1132	78.6404
B	Abell 2259	C		0.991±0.141	−1.194±0.032	1.09±0.08		0.250±0.024	260.0345	27.6698	260.0402	27.6689
B	Abell 2261	C	clp	1.025±0.063	−0.895±0.013	1.20±0.12		0.170±0.017	260.6136	32.1331	260.6133	32.1326
B	Abell 2294	C		0.715±0.083	−1.163±0.041	0.95±0.09		0.124±0.028	261.0594	85.8868		
B	Abell 2390	C	alp	0.946±0.015	−0.827±0.014	1.34±0.03		0.262±0.005	328.4034	17.6952	328.4034	17.6955
B	Abell 2409	C		0.710±0.148	−1.157±0.043	1.18±0.08		0.123±0.018	330.2200	20.9695	330.2190	20.9693
B	Abell 2631	C		0.579±0.063	−1.566±0.163	0.88±0.06		0.287±0.024	354.4064	0.2680	354.4156	0.2714
B	Abell 267	C		0.754±0.119	−1.120±0.020	1.05±0.06		0.294±0.015	28.1764	1.0125	28.1748	1.0071
B	Abell 399	R		1.022±0.072	−1.507±0.282	0.92±0.06		0.102±0.031	44.4572	13.0478		
B	Abell 401	C		0.946±0.136	−1.244±0.029	1.08±0.04		0.250±0.007	44.7380	13.5827		
B	Abell 478	C	af	0.958±0.017	−0.817±0.010	1.29±0.04	√	0.177±0.009	63.3537	10.4650		
B	Abell 520	C		0.346±0.157	−1.625±0.209	1.19±0.03		0.169±0.008	73.5354	2.9098		
B	Abell 586	C		0.996±0.094	−1.077±0.026	1.07±0.11		0.131±0.023	113.0840	31.6325	113.0845	31.6335
B	Abell 611	C	aclp	0.876±0.039	−0.918±0.014	1.19±0.04		0.140±0.017	120.2371	36.0560	120.2367	36.0566
B	Abell 646	C			−1.389				125.5496	47.1059	125.5398	47.0980
B	Abell 665	C		0.213±0.008	−1.360±0.074	0.76±0.03		0.211±0.014	127.7479	65.8405	127.7387	65.8418
B	Abell 68	C		0.882±0.177	−1.185±0.075	1.34±0.16		0.344±0.032	9.2769	9.1581	9.2785	9.1567
B	Abell 697	C	l	1.164±0.130	−1.143±0.028	1.33±0.09		0.235±0.016	130.7395	36.3662	130.7398	36.3665
B	Abell 750	C		0.802±0.052	−1.093±0.026	0.87±0.05		0.213±0.015	137.3031	10.9747	137.3031	10.9747
B	Abell 773	C		1.031±0.133	−1.190±0.047	1.26±0.08		0.215±0.017	139.4695	51.7273	139.4726	51.7270
B	Abell 781	C			−1.714				140.1090	30.4996	140.1075	30.4941
B	Abell 795	C		0.840±0.024	−0.944±0.029	0.93±0.04		0.239±0.012	141.0239	14.1737	141.0221	14.1726
B	Abell 963	C	alp	1.147±0.037	−0.921±0.018	1.32±0.04		0.111±0.011	154.2651	39.0476	154.2651	39.0471
B	Coma	R		0.993±0.045	−1.539±0.014	1.21±0.04		0.218±0.004	194.9309	27.9301	194.8988	27.9593
B	Hercules	C		1.268±0.181	−0.915±0.038	1.29±0.27		0.263±0.019	252.7838	4.9925		
B	RX J0439.0+0520	C	af	1.249±0.104	−0.717±0.036	1.31±0.10	√	0.092±0.024	69.7592	5.3455		
B	RX J0439.0+0715	C		0.873±0.056	−0.994±0.033	1.38±0.11		0.216±0.020	69.7529	7.2684		
B	RX J1720.1+2638	C	l	0.905±0.027	−0.672±0.016	1.07±0.03	√	0.161±0.008	260.0414	26.6257	260.0418	26.6256
B	RX J1750.2+3505	C		1.041±0.108	−0.775±0.042	0.95±0.13		0.168±0.026	267.5705	35.0829		
B	RX J2129.6+0005	C	acl$f$	1.201±0.082	−0.788±0.021	1.29±0.09	√	0.249±0.015	322.4158	0.0895	322.4165	0.0892
B	Zwicky 2089	C	lf	1.447±0.083	−0.577±0.027	1.43±0.09	√	0.285±0.012	135.1537	20.8943	135.1536	20.8946
B	Zwicky 2701	C	lf	1.481±0.112	−0.768±0.018	1.58±0.14	√	0.276±0.009	148.2050	51.8848	148.2048	51.8847
B	Zwicky 3146	C	al	0.816±0.023	−0.555±0.009	1.35±0.05		0.108±0.017	155.9151	4.1865	155.9151	4.1863
B	Zwicky 5029	C		1.021±0.117	−1.470±0.342	1.27±0.07		0.245±0.011	184.4280	3.6610	184.4214	3.6558
B	Zwicky 5247	C			−1.936				188.5789	9.7700	188.5728	9.7662
B	Zwicky 7160	C	lp	1.005±0.038	−0.524±0.015	1.25±0.06	√	0.191±0.012	224.3128	22.3429	224.3129	22.3429
B	Zwicky 808	C		1.216±0.146	−0.842±0.027	1.31±0.21		0.080±0.030	45.4091	1.9205	45.4092	1.9207
B⋆	Abell 2063	R		1.235±0.064	−1.418±0.032	1.22±0.09		0.219±0.023	230.7763	8.6058	230.7721	8.6092
B⋆	Abell 2199	R		1.394±0.038	−0.904±0.002	1.48±0.05		0.143±0.023	247.1532	39.5521	247.1593	39.5513
R	1E 0657−56	C		0.688±0.025	−1.248±0.085	1.11±0.02		0.179±0.009	104.6250	−55.9411		
R	Abell 1650	C		0.857±0.021	−1.034±0.017	1.15±0.02		0.304±0.003	194.6728	−1.7623	194.6729	−1.7615
R	Abell 1651	C		0.982±0.049	−1.133±0.028	1.15±0.06		0.161±0.014	194.8427	−4.1966		
R	Abell 1664	C		0.670±0.048	−0.717±0.017	0.81±0.03		0.320±0.011	195.9270	−24.2455		
R	Abell 1689	C	l	1.298±0.029	−0.836±0.007	1.40±0.03		0.130±0.004	197.8731	−1.3416	197.8730	−1.3411
R	Abell 209	C	cl	0.738±0.091	−1.320±0.163	0.99±0.11		0.280±0.022	22.9711	−13.6110	22.9689	−13.6113
R	Abell 2104	C		1.462±0.189	−1.261±0.064	1.63±0.13		0.150±0.015	235.0333	−3.3049		
R	Abell 2163	C		0.649±0.049	−1.163±0.027	1.00±0.02		0.238±0.006	243.9406	−6.1489		
R	Abell 2420	C		0.757±0.061	−1.441±0.207	1.17±0.11		0.195±0.018	332.5791	−12.1732		
R	Abell 2426	C		0.543±0.030	−1.157±0.041	1.11±0.10		0.150±0.023	333.6400	−10.3691		
R	Abell 2485	C	cl	1.078±0.144	−1.142±0.032	1.11±0.13		0.178±0.034	342.1290	−16.1079		
R	Abell 2537	C	al	1.122±0.061	−1.011±0.022	1.29±0.06		0.169±0.015	347.0922	−2.1910	347.0926	−2.1921
R	Abell 2597	C		1.446±0.042	−0.630±0.006	1.99±0.09	√	0.185±0.007	351.3321	−12.1237		
R	Abell 2645	C		0.596±0.281	−1.309±0.219	1.02±0.31		0.391±0.063	355.3211	−9.0210	355.3209	−9.0199
R	Abell 2667	C		0.936±0.037	−0.729±0.026	1.35±0.10	√	0.190±0.014	357.9142	−26.0842		

Cat.	Name	Obs.	flags	s	p	a	Rel.	ellip.	RA$_X$	Dec$_X$	RA$_{BCG}$	Dec$_{BCG}$
R	Abell 3112	C		0.933±0.023	−0.844±0.014	1.13±0.04		0.283±0.006	49.4899	−44.2384		
R	Abell 3158	C		1.092±0.143	−1.362±0.185	1.03±0.06		0.189±0.010	55.7225	−53.6296		
R	Abell 3266	R		0.843±0.055	−1.546±0.234	1.07±0.05		0.226±0.015	67.8061	−61.4545		
R	Abell 3444	C	f	1.206±0.040	−0.653±0.014	1.41±0.07	√	0.302±0.009	155.9592	−27.2563		
R	Abell 3558	R		0.756±0.074	−1.223±0.032	0.68±0.09		0.332±0.065	201.9867	−31.4955		
R	Abell 3571	R		1.167±0.097	−1.108±0.011	1.27±0.08		0.258±0.013	206.8683	−32.8660		
R	Abell 3667	R		0.383±0.049	−1.399±0.155	0.69±0.09		0.412±0.051	303.1311	−56.8422		
R	Abell 3695	C		0.628±0.092	−1.491±1.151	1.04±0.16		0.169±0.027	308.7049	−35.8230		
R	Abell 3827	C		1.203±0.052	−1.133±0.008	1.40±0.07		0.084±0.006	330.4726	−59.9461		
R	Abell 383	C	aclp	1.325±0.058	−0.716±0.019	1.48±0.08	√	0.063±0.010	42.0142	−3.5293	42.0141	−3.5291
R	Abell 3921	C		0.883±0.072	−1.214±0.068	0.87±0.04		0.284±0.012	342.4893	−64.4294		
R	Abell 521	C		0.420±0.290	−1.528±0.270	1.03±0.16		0.267±0.020	73.5276	−10.2211	73.5287	−10.2235
R	Abell 545	C			−1.222				83.1057	−11.5428		
R	Abell 754	C		0.145	−1.474±0.295	0.94		0.291±0.025	137.3333	−9.6820		
R	Abell 780	R		1.315±0.077	−0.756±0.004	1.46±0.12	√	0.146±0.021	139.5265	−12.0962		
R	Abell 85	R		0.799±0.040	−0.918±0.005	0.80±0.11		0.232±0.016	10.4603	−9.3033	10.4602	−9.3036
R	Abell 907	C	l	1.057±0.045	−0.859±0.013	1.24±0.04		0.344±0.007	149.5915	−11.0638		
R	Hydra	R		1.425±0.035	−0.745±0.006	1.42±0.05	√	0.165±0.006	139.5245	−12.0949		
R	J0043.4−2037	C		0.901±0.160	−1.135±0.062	1.32±0.11		0.174±0.022	10.8523	−20.6247	10.8547	−20.6171
R	J0055.9−3732	C			−1.756				14.0133	−37.5454		
R	J0105.5−2439	C			−1.589				16.3978	−24.6801		
R	J0118.1−2658	C		0.553±0.066	−1.259±0.141	0.86±0.05		0.266±0.033	19.5472	−26.9662		
R	J0220.9−3829	C		0.256±0.054	−0.877±0.055	0.69±0.17		0.636±0.055	35.2357	−38.4802		
R	J0232.2−4420	C		0.535±0.047	−0.830±0.013	0.94±0.16		0.212±0.049	38.0774	−44.3467		
R	J0237.4−2630	C		1.055±0.121	−0.850±0.022	1.33±0.14		0.235±0.028	39.3651	−26.5079		
R	J0304.1−3656	C		0.964±0.089	−1.283±0.172	0.99±0.08		0.196±0.029	46.0131	−36.9425		
R	J0307.0−2840	C		1.438±0.108	−0.940±0.042	1.46±0.12		0.134±0.019	46.7582	−28.6657		
R	J0331.1−2100	C		0.957±0.040	−0.706±0.021	0.99±0.04		0.171±0.017	52.7747	−21.0087		
R	J0336.3−4037	C		0.731±0.066	−1.098±0.024	1.32±0.11		0.145±0.022	54.0644	−40.6291		
R	J0449.9−4440	C		0.819±0.136	−1.333±0.112	0.85±0.09		0.194±0.024	72.4830	−44.6730		
R	J0516.6−5430	C			−1.628				79.1512	−54.5046		
R	J0528.9−3927	C		0.767±0.038	−0.963±0.042	0.76±0.04		0.162±0.028	82.2207	−39.4717		
R	J0547.6−3152	C		0.574±0.094	−1.267±0.076	1.09±0.07		0.132±0.018	86.9058	−31.8688		
R	J0638.7−5358	C		0.981±0.053	−0.973±0.016	1.14±0.08		0.295±0.017	99.7019	−53.9739		
R	J1333.6−2317	C		0.487±0.157	−1.202±0.054	0.89±0.13		0.206±0.043	203.4228	−23.2986		
R	J1459.4−1811	C	f	0.944±0.031	−0.612±0.023	1.12±0.06	√	0.142±0.014	224.8706	−18.1793		
R	J1504.1−0248	C	al$f$	1.222±0.046	−0.456±0.021	1.57±0.08	√	0.176±0.009	226.0308	−2.8041	226.0313	−2.8046
R	J1524.2−3154	C	f	1.214±0.038	−0.627±0.011	1.24±0.04	√	0.223±0.009	231.0534	−31.9061		
R	J1558.3−1410	C		1.214±0.037	−0.837±0.013	1.60±0.08		0.199±0.008	239.5908	−14.1666		
R	J2011.3−5725	C		1.095±0.105	−0.854±0.031	1.26±0.12		0.220±0.027	302.8627	−57.4197		
R	J2014.8−2430	C		1.142±0.046	−0.629±0.012	1.30±0.07	√	0.054±0.012	303.7156	−24.5062		
R★	Abell 119	R		1.021±0.097	−1.982±0.234	1.17±0.15		0.141±0.027	14.0596	−1.2562	14.0672	−1.2554
R★	Abell 133	R		1.258±0.169	−0.806±0.011	1.37±0.15	√	0.187±0.029	15.6726	−21.8821		
R★	Abell 3376	R			−1.816±0.238				90.4719	−39.9738		
R★	Abell 3391	R		0.999±0.120	−1.654±0.343	1.01±0.15		0.311±0.038	96.5964	−53.6962		
R★	Abell 3532	R		1.228±0.165	−1.573±0.211	1.34±0.18		0.179±0.050	194.3404	−30.3696		
R★	Abell 3562	R		0.905±0.143	−1.175±0.122	0.68±0.23		0.147±0.050	203.3985	−31.6721		
R★	Abell 4059	R		1.208±0.154	−1.000±0.032	1.31±0.12		0.232±0.031	359.2534	−34.7578		
R★	Abell 496	R		1.075±0.085	−0.866±0.024	1.27±0.11		0.176±0.022	68.4080	−13.2579		
R★	J2344.2−0422	R		1.127±0.083	−1.337±0.140	1.21±0.09		0.228±0.040	356.0721	−4.3762	356.0759	−4.3803
C	3C 196	C		0.847±0.066	−0.704±0.018	0.98±0.10		0.212±0.037	123.8663	−3.1408		
C	Abell 2319	C		1.109±0.068	−1.372±0.064	1.00±0.07		0.194±0.014	290.2853	43.9729		
C	Abell 3628	C		0.629±0.105	−1.686±0.347	0.64±0.08		0.335±0.027	247.8701	−75.1242		
C	Abell 644	C		0.549±0.026	−1.080±0.014	1.14±0.02		0.257±0.005	124.3564	−7.5082	124.3568	−7.5127
C	Cygnus A	R		0.266±0.071	−1.069±0.061	0.76±0.26		0.493±0.088	299.8576	40.7487		
C	Ophiuchus	R		1.479±0.097	−1.081±0.017	1.53±0.09		0.129±0.011	258.1160	−23.3696		
C	PKS 0745−191	C	af	1.059±0.024	−0.667±0.003	1.18±0.04	√	0.163±0.007	116.8798	−19.2946		
C	Perseus	R		1.100±0.006	−0.689±0.015	1.21±0.03	√	0.187±0.005	49.9486	41.5121	49.9507	41.5117
C	Triangulum	R		1.176±0.090	−1.248±0.053	1.36±0.12		0.167±0.024	249.5710	−64.3579		
C★	AWM 7	R		0.986±0.041	−1.119±0.005	1.60±0.10		0.271±0.009	43.6197	41.5796		
M	3C 295	C	ap$f$	1.006±0.095	−0.517±0.036	1.39±0.16	√	0.088±0.031	212.8354	52.2030		
M	Abell 1576	C			−1.133				189.2387	63.1895	189.2443	63.1872
M	Abell 1995	C		0.974±0.210	−1.083±0.054	1.45±0.18		0.288±0.041	223.2394	58.0483	223.2395	58.0487
M	Abell 2552	C	l		−0.998				347.8884	3.6351	347.8888	3.6350
M	Abell 2744	C		0.404±0.036	−1.224±0.076	0.91±0.15		0.273±0.021	3.5797	−30.3908		
M	IRAS 09104+4109	C	pf	1.202±0.075	−0.462±0.020	1.44±0.08	√	0.109±0.018	138.4397	40.9415	138.4396	40.9412
M	J0011.7−1523	C	af	1.273±0.081	−0.805±0.029	1.30±0.08	√	0.231±0.017	2.9285	−15.3890		
M	J0025.4−1222	C		0.907±0.107	−1.238±0.273	1.24±0.08		0.314±0.022	6.3732	−12.3778	6.3642	−12.3730
M	J0035.4−2015	C		1.164±0.184	−0.969±0.023	1.43±0.12		0.339±0.017	8.8604	−20.2632	8.8590	−20.2623
M	J0111.5+0855	C			−0.918				17.8812	8.9281	17.8812	8.9282

Cat.	Name	Obs.	flags	s	p	a	Rel.	ellip.	RA$_{\rm X}$	Dec$_{\rm X}$	RA$_{\rm BCG}$	Dec$_{\rm BCG}$
M	J0140.0−0555	C		0.656±0.072	−1.079±0.076	0.85±0.08		0.301±0.033	25.0067	−5.9188	25.0033	−5.9174
M	J0150.3−1005	C	f	1.146±0.103	−0.695±0.035	1.33±0.13	√	0.198±0.036	27.5887	−10.0915	27.5887	−10.0918
M	J0152.5−2852	C		0.703±0.064	−0.918±0.044	0.90±0.08		0.274±0.031	28.1436	−28.8937		
M	J0159.0−3412	C			−1.558				29.7589	−34.2159		
M	J0159.8−0849	C	af	1.118±0.048	−0.728±0.023	1.27±0.06	√	0.088±0.016	29.9554	−8.8333	29.9556	−8.8330
M	J0242.5−2132	C	af	1.327±0.145	−0.485±0.017	1.40±0.20	√	0.117±0.034	40.6495	−21.5407		
M	J0257.1−2325	C		1.061±0.098	−0.881±0.023	1.21±0.09		0.247±0.020	44.2873	−23.4348	44.2865	−23.4348
M	J0257.6−2209	C		0.915±0.065	−0.950±0.046	1.25±0.10		0.166±0.025	44.4223	−22.1549		
M	J0308.9+2645	C		0.954±0.064	−1.024±0.035	1.06±0.07		0.127±0.022	47.2329	26.7611		
M	J0326.8−0043	C		1.189±0.192	−0.415±0.015	1.24±0.25	√	0.135±0.053	51.7084	−0.7310	51.7081	−0.7310
M	J0329.6−0211	C	ac	0.851±0.084	−0.605±0.046	1.08±0.13		0.147±0.037	52.4234	−2.1965	52.4232	−2.1962
M	J0358.8−2955	C		0.669±0.210	−0.989±0.021	1.29±0.13		0.268±0.019	59.7247	−29.9277		
M	J0404.2−2703	C			−1.440				61.0788	−27.0517		
M	J0404.6+1109	C		0.353±0.144	−1.606±0.391	0.02±0.07		0.353±0.060	61.1376	11.1350		
M	J0416.1−2403	C		0.462±0.058	−1.153±0.181	1.34±0.19		0.494±0.030	64.0392	−24.0668		
M	J0417.5−1154	C		0.372±0.026	−0.651±0.037	1.19±0.09		0.503±0.023	64.3945	−11.9092	64.3946	−11.9089
M	J0429.6−0253	C	acf	0.932±0.075	−0.617±0.039	1.31±0.10	√	0.205±0.027	67.4000	−2.8853	67.4001	−2.8852
M	J0451.9+0006	C		0.905±0.155	−1.005±0.097	0.90±0.18		0.454±0.042	72.9773	0.1058	72.9777	0.1051
M	J0455.2+0657	C		0.979±0.188	−0.814±0.051	1.20±0.21		0.255±0.047	73.8219	6.9636		
M	J0520.7−1328	C		1.089±0.103	−0.921±0.033	1.34±0.13		0.137±0.028	80.1750	−13.4799		
M	J0547.0−3904	C		0.797±0.081	−0.635±0.026	0.81±0.11		0.298±0.036	86.7561	−39.0738		
M	J0553.4−3342	C		0.492±0.103	−1.180±0.133	1.09±0.12		0.361±0.019	88.3568	−33.7088		
M	J0647.7+7015	C		1.024±0.094	−0.964±0.022	1.17±0.08		0.368±0.020	101.9603	70.2483	101.9611	70.2484
M	J0712.3+5931	C		1.098±0.131	−1.018±0.064	1.15±0.12		0.335±0.031	108.0861	59.5388		
M	J0717.5+3745	C		0.758±0.038	−1.131±0.102	1.00±0.05		0.317±0.013	109.3816	37.7580	109.3982	37.7457
M	J0744.8+3927	C	ac	0.645±0.031	−0.766±0.041	1.08±0.05		0.125±0.021	116.2201	39.4576	116.2200	39.4574
M	J0911.2+1746	C		0.809±0.186	−1.317±0.278	0.85±0.14		0.196±0.064	137.7961	17.7761	137.7980	17.7747
M	J0940.9+0744	C		1.064±0.141	−1.126±0.265	1.12±0.14		0.135±0.054	145.2242	7.7403	145.2238	7.7404
M	J0949.8+1708	C		1.134±0.120	−1.062±0.033	1.19±0.11		0.142±0.031	147.4658	17.1189	147.4658	17.1195
M	J1006.9+3200	C			−1.000				151.7244	32.0304	151.7278	32.0255
M	J1105.7−1014	C		0.738±0.127	−1.085±0.066	0.77±0.11		0.169±0.046	166.4430	−10.2435		
M	J1108.8+0906	C		0.925±0.140	−1.099±0.067	1.03±0.12		0.249±0.039	167.2302	9.0993	167.2307	9.1004
M	J1115.2+5320	C		0.720±0.094	−1.292±0.385	0.75±0.10		0.230±0.044	168.8154	53.3326	168.8119	53.3318
M	J1115.8+0129	C	acf	1.346±0.094	−0.676±0.034	1.61±0.12	√	0.244±0.015	168.9661	1.4990	168.9663	1.4986
M	J1131.8−1955	C		0.398±0.054	−0.975±0.055	0.50±0.09		0.319±0.057	172.9770	−19.9290		
M	J1149.5+2223	C		0.808±0.060	−1.128±0.129	0.87±0.05		0.302±0.021	177.3970	22.4027	177.3986	22.3984
M	J1206.2−0847	C		0.867±0.040	−0.872±0.022	1.36±0.08		0.174±0.021	181.5511	−8.8006	181.5506	−8.8009
M	J1218.4+4012	C		0.441±0.065	−1.178±0.059	0.89±0.11		0.220±0.048	184.6205	40.2083	184.6100	40.2247
M	J1226.8+2153	C			−1.000				186.7126	21.8323	186.7130	21.8312
M	J1311.0−0310	C	ac	1.287±0.091	−0.747±0.023	1.54±0.10	√	0.058±0.018	197.7565	−3.1771	197.7575	−3.1777
M	J1319.9+7003	C		0.871±0.125	−1.065±0.089	0.86±0.17		0.241±0.067	200.0347	70.0770		
M	J1354.6+7715	C		0.253±0.021	−0.903±0.073	1.21±0.19		0.445±0.021	208.6774	77.2547		
M	J1359.1−1929	C	af	0.943±0.080	−0.726±0.026	1.25±0.08	√	0.155±0.030	209.7928	−19.4902		
M	J1423.8+2404	C	acf	1.364±0.088	−0.422±0.018	1.48±0.08	√	0.168±0.017	215.9496	24.0784	215.9495	24.0784
M	J1427.2+4407	C	af	0.977±0.066	−0.578±0.034	1.26±0.10	√	0.233±0.025	216.8174	44.1251	216.8172	44.1252
M	J1427.6−2521	C	af	1.297±0.107	−0.759±0.030	1.39±0.10	√	0.146±0.024	216.9143	−25.3508		
M	J1532.8+3021	C	acf	1.251±0.078	−0.500±0.008	1.39±0.10	√	0.196±0.017	233.2244	30.3498	233.2241	30.3498
M	J1621.3+3810	C	af	1.030±0.045	−0.706±0.021	1.29±0.06	√	0.127±0.017	245.3536	38.1690	245.3531	38.1691
M	J1720.2+3536	C	acf	0.931±0.046	−0.734±0.028	1.34±0.08	√	0.185±0.017	260.0700	35.6071	260.0698	35.6073
M	J1731.6+2252	C		0.711±0.252	−1.585±0.248	1.03±0.17		0.281±0.029	262.9150	22.8651	262.9164	22.8663
M	J1931.8−2634	C	acf	1.419±0.078	−0.545±0.020	1.63±0.12	√	0.279±0.010	292.9569	−26.5760	292.9568	−26.5757
M	J2046.0−3430	C	af	1.359±0.119	−0.585±0.042	1.40±0.13	√	0.084±0.022	311.5022	−34.5049		
M	J2049.9−3217	C		0.839±0.071	−1.108±0.031	1.04±0.06		0.221±0.026	312.4830	−32.2803		
M	J2129.4−0741	C		0.742±0.082	−1.070±0.058	0.79±0.05		0.166±0.043	322.3591	−7.6908	322.3588	−7.6910
M	J2135.2−0102	C		0.843±0.163	−1.273±0.293	0.89±0.23		0.259±0.053	323.7976	−1.0479	323.8009	−1.0488
M	J2211.7−0349	C		0.664±0.036	−0.767±0.020	1.18±0.07		0.266±0.018	332.9413	−3.8301	332.9413	−3.8290
M	J2214.9−1359	C		1.045±0.110	−1.055±0.083	1.09±0.08		0.323±0.048	333.7385	−14.0030	333.7387	−14.0036
M	J2228.5+2036	C		0.500±0.048	−1.048±0.050	0.73±0.11		0.182±0.039	337.1400	20.6203	337.1405	20.6212
M	J2229.7−2755	C	af	1.340±0.126	−0.438±0.031	1.51±0.14	√	0.210±0.022	337.4382	−27.9264		
M	J2243.3−0935	C		1.052±0.203	−1.372±0.186	1.30±0.18		0.362±0.053	340.8393	−9.5958	340.8325	−9.5919
M	J2245.0+2637	C		1.310±0.120	−0.805±0.012	1.28±0.12	√	0.251±0.029	341.2695	26.6345	341.2694	26.6346
M	J0947.2+7623	C	af	1.335±0.066	−0.450±0.016	1.42±0.07	√	0.287±0.010	146.8029	76.3874		
M	MS 0015.9+1609	C		0.919±0.056	−1.031±0.034	1.18±0.06		0.165±0.022	4.6396	16.4358	4.6399	16.4378
M	MS 0451.6−0305	C		0.702±0.031	−0.998±0.016	1.15±0.04		0.248±0.013	73.5459	−3.0152	73.5452	−3.0144
M	MS 2137.3−2353	C	acf	1.539±0.079	−0.489±0.015	1.53±0.08	√	0.128±0.013	325.0633	−23.6612	325.0632	−23.6612
M	RX J0027.6+2616	C			−1.519				6.9396	26.2723	6.9407	26.2740
M	RX J1347.5−1145	C	acpf	0.881±0.027	−0.464±0.015	1.28±0.06	√	0.205±0.013	206.8778	−11.7524	206.8776	−11.7527
M	RX J2003.5−2323	C		0.895±0.303	−1.518±1.247	1.38±0.24		0.159±0.022	300.8703	−23.3907		
M	Zwicky 1358	C	p	0.917±0.047	−0.817±0.051	1.19±0.08		0.212±0.018	209.9605	62.5179	209.9607	62.5181
M	Zwicky 1953	C		0.639±0.054	−1.071±0.031	1.02±0.07		0.180±0.026	132.5261	36.0713	132.5330	36.0705

Cat.	Name	Obs. flags	s	p	a	Rel.	ellip.	RA_X	Dec_X	RA_{BCG}	Dec_{BCG}
4	3C 288	C	1.175±0.093	−0.800±0.048	1.25±0.09	√	0.126±0.028	204.7078	38.8531		
4	3C 88	C	0.554±0.199	−1.014±0.060	0.58±0.28		0.331±0.155	51.9757	2.5617		
4	Abell 1775	C	0.291±0.012	−1.192±0.024	0.92±0.03		0.116±0.010	205.4527	26.3732	205.4548	26.3735
4	Abell 744	C	0.859±0.099	−0.989±0.113	0.99±0.13		0.110±0.033	136.8359	16.6519	136.8354	16.6519
4	J0030+2618	C		−1.621				7.6402	26.3026	7.6418	26.3025
4	J0057−2616	C		−1.281				14.3451	−26.2809		
4	J0106+3209	C		−0.836				16.7457	32.1576	16.7455	32.1579
4	J0124+0932	C						21.1991	9.5389	21.1989	9.5388
4	J0141−3034	C						25.3864	−30.5775		
4	J0152−1357	C		−1.650				28.1839	−13.9563		
4	J0159+0030	C	1.086±0.138	−0.924±0.066	1.17±0.16		0.106±0.048	29.8215	0.5038	29.8217	0.5034
4	J0216−1747	C						34.1355	−17.7935		
4	J0230+1836	C	0.332±0.158	−1.750±0.262	0.66±0.29		0.473±0.069	37.6211	18.6041		
4	J0237−5224	C		−1.850				39.4976	−52.4128		
4	J0245+0936	C	0.899±0.255	−0.929±0.360	1.20±0.31		0.054±0.043	41.4537	9.6105		
4	J0302−0423	C		−0.522				45.5880	−4.3903	45.5877	−4.3899
4	J0306−0943	C		−0.818				46.6187	−9.7313		
4	J0318−0302	C	0.405	−1.257±0.403	0.91		0.356±0.062	49.6425	−3.0491		
4	J0328−2140	C	1.031±0.132	−1.136±0.177	1.13±0.16		0.198±0.040	52.0563	−21.6722		
4	J0333−2456	C		−1.811				53.2944	−24.9422		
4	J0334−3900	C						53.5107	−39.0237		
4	J0336−2804	C						54.2085	−28.0762		
4	J0340−2823	C	0.742±0.165	−1.143±0.277	0.94±0.24		0.371±0.075	55.2193	−28.3853		
4	J0340−2840	C		−2.235				55.1065	−28.6730		
4	J0350−3801	C		−1.592				57.6696	−38.0368		
4	J0355−3741	C	0.977±0.162	−1.141±0.275	1.20±0.17		0.170±0.060	58.9970	−37.6960		
4	J0405−4100	C	1.148±0.198	−1.199±0.297	1.31±0.18		0.243±0.054	61.3517	−41.0058		
4	J0422−5009	C						65.6184	−50.1493		
4	J0521−2530	C						80.3376	−25.5270		
4	J0522−3624	C		−1.449				80.5640	−36.4167		
4	J0542−4100	C	0.552±0.094	−1.454±0.270	0.78±0.16		0.295±0.050	85.7068	−40.9996		
4	J0809+2811	C		−1.682				122.4240	28.2004	122.4285	28.2048
4	J0838+1948	C	0.798±0.166	−0.999±0.248	0.78±0.18		0.249±0.072	129.6289	19.8057	129.6291	19.8057
4	J0853+5759	C						133.3224	57.9973	133.3319	57.9965
4	J0900+3920	C						135.0016	39.3479	135.0215	39.3312
4	J0926+1242	C	1.036±0.159	−1.254±0.928	0.97±0.22		0.179±0.063	141.6525	12.7182	141.6528	12.7178
4	J0953+6947	C						148.6741	69.7811	148.4300	69.7941
4	J0956+4107	C		−1.566				149.0129	41.1208	149.0169	41.1158
4	J0958+4702	C	1.041±0.190	−1.053±0.179	1.16±0.19		0.223±0.077	149.5800	47.0343	149.5806	47.0334
4	J1002+6858	C		−1.583				150.5395	68.9769	150.5372	68.9776
4	J1003+3253	C	0.927±0.152	−0.799±0.119	1.14±0.19		0.140±0.073	150.7696	32.8944	150.7693	32.8947
4	J1058+0136	C		−2.308				164.5540	1.6067	164.5458	1.6046
4	J1116+1803	C						169.2279	18.0517	169.2276	18.0518
4	J1117+1744	C		−1.959				169.3761	17.7463	169.3755	17.7484
4	J1120+2326	C	0.633±0.132	−1.732±0.240	1.14±0.24		0.196±0.066	170.2390	23.4439	170.2453	23.4541
4	J1120+4318	C	0.737±0.141	−0.989±0.067	0.86±0.10		0.305±0.052	170.0282	43.3026	170.0234	43.3025
4	J1202+5751	C		−1.971				180.5766	57.8664	180.5496	57.8620
4	J1206−0744	C	0.794±0.223	−1.088±0.430	0.61±0.28		0.196±0.091	181.6325	−7.7413		
4	J1212+2733	C	0.717±0.153	−1.246±0.286	0.90±0.14		0.222±0.056	183.0776	27.5482	183.0770	27.5486
4	J1213+0253	C		−1.791				183.3960	2.8959	183.3937	2.8989
4	J1217+4729	C						184.4941	47.4747	184.4154	47.4897
4	J1220+7522	C						185.0761	75.3712		
4	J1221+4918	C	0.791±0.166	−1.557±0.373	1.16±0.16		0.328±0.044	185.3575	49.3080	185.3595	49.3145
4	J1222+2709	C	0.840±0.146	−1.073±0.437	1.17±0.17		0.134±0.062	185.5073	27.1593	185.5040	27.1561
4	J1226+3332	C	ac	1.014±0.097	−1.039±0.132	1.17±0.12	0.126±0.037	186.7417	33.5465	186.7427	33.5468
4	J1231+4137	C		−2.149				187.9393	41.6244	187.9329	41.6261
4	J1236+1224	C						189.1134	12.4041	189.1160	12.4052
4	J1248−0548	C						192.1499	−5.8002	192.1496	−5.8008
4	J1259+3120	C		−1.937				194.9655	31.3520	194.9666	31.3517
4	J1312+3900	C						198.0817	39.0133	198.0816	39.0141
4	J1329+1143	C		−2.035				202.3528	11.7508	202.3398	11.7351
4	J1334+5031	C		−1.142				203.5834	50.5170	203.5858	50.5177
4	J1349+4918	C	0.837±0.132	−1.099±0.178	0.83±0.12		0.316±0.056	207.2528	49.3118	207.2521	49.3112
4	J1354−0221	C		−1.909				208.5718	−2.3651	208.5717	−2.3664
4	J1416+4446	C	0.924±0.114	−0.906±0.052	1.05±0.11		0.237±0.046	214.1164	44.7794	214.1162	44.7790
4	J1524+0957	C	0.535±0.224	−1.663±0.344	1.19±0.33		0.256±0.052	231.1625	9.9622	231.1598	9.9621
4	J1533+3108	C		−2.037				233.3195	31.1442	233.3140	31.1452
4	J1537+1200	C		−1.747				234.4315	12.0053	234.4305	12.0063
4	J1630+2434	C		−1.023				247.5665	24.5741	247.5661	24.5744
4	J1641+4001	C		−0.960				250.4731	40.0288	250.4735	40.0293

Cat.	Name	Obs.	flags	s	p	a	Rel.	ellip.	RA_X	Dec_X	RA_{BCG}	Dec_{BCG}
4	J1701+6414	C		0.877±0.150	−0.996±0.113	0.86±0.24		0.118±0.045	255.1738	64.2166	255.1740	64.2163
4	J1807+6946	C							271.7308	69.7967		
4	J2137+0027	C		0.647±0.188	−0.524±0.137	0.68±0.30		0.210±0.060	324.2849	0.4464	324.2849	0.4464
4	J2220−5228	C		0.507±0.326	−0.611±0.247	−0.08±0.10		0.083±0.046	335.0362	−52.4642		
4	J2318−4235	C							349.5275	−42.5885		
4	RX J1159+5531	C		1.226±0.158	−0.576±0.032	1.14±0.19	√	0.082±0.030	179.9675	55.5352	179.9674	55.5349
4	RX J1340+4018	C		0.927±0.141	−1.067±0.074	0.96±0.17		0.264±0.058	205.1369	40.2939	205.1367	40.2944
4	RX J1552+2013	C			−2.032				238.0524	20.2282	238.0577	20.2289
4	RX J2247+0337	C		0.807±0.183	−1.699±0.546	0.76±0.23		0.202±0.070	341.8663	3.6167	341.8661	3.6166
S	J0000−5748	C	f	0.901±0.139	−0.689±0.087	1.17±0.14	√	0.231±0.043	0.2499	−57.8095	0.2503	−57.8093
S	J0013−4906	C		0.285±0.050	−1.042±0.079	0.91±0.16		0.181±0.055	3.3276	−49.1108		
S	J0014−4952	C		0.464±0.270	−1.583±0.424	0.89±0.16		0.239±0.052	3.6977	−49.8815		
S	J0037−5047	C							9.4442	−50.7913		
S	J0040−4407	C		0.836±0.186	−0.998±0.045	0.99±0.15		0.194±0.052	10.2078	−44.1309		
S	J0058−6145	C		0.782±0.179	−1.118±0.363	0.76±0.20		0.244±0.083	14.5874	−61.7676		
S	J0102−4603	C			−1.312				15.6772	−46.0715		
S	J0106−5943	C		0.882±0.172	−1.081±0.065	1.01±0.15		0.347±0.048	16.6181	−59.7202		
S	J0123−4821	C		0.664±0.150	−1.758±0.180	0.71±0.19		0.167±0.061	20.7986	−48.3567		
S	J0142−5032	C			−1.659				25.5422	−50.5402		
S	J0151−5954	C			−1.912				27.8577	−59.9078		
S	J0156−5541	C			−1.321				29.0426	−55.6984		
S	J0200−4852	C			−1.582				30.1434	−48.8715		
S	J0212−4656	C			−1.334				33.1035	−46.9540		
S	J0256−5617	C			−1.826				44.1078	−56.2971	44.0880	−56.3031
S	J0307−5042	C		0.603±0.136	−1.378±0.589	0.93±0.20		0.140±0.069	46.9599	−50.7017		
S	J0307−6225	C			−1.844				46.8254	−62.4358	46.8495	−62.4028
S	J0324−6236	C			−1.419				51.0519	−62.5990	51.0511	−62.5988
S	J0334−4659	C		0.977±0.101	−0.912±0.062	1.05±0.10		0.299±0.036	53.5458	−46.9960		
S	J0352−5647	C			−1.474				58.2386	−56.7972	58.2759	−56.7608
S	J0411−4819	C		0.296±0.179	−0.692±0.217	0.15±0.32		0.270±0.116	62.8179	−48.3154		
S	J0426−5455	C			−0.904				66.5203	−54.9208	66.5171	−54.9253
S	J0441−4854	C		1.111±0.182	−1.037±0.198	1.00±0.17		0.112±0.049	70.4506	−48.9231		
S	J0446−5849	C							71.5140	−58.8275		
S	J0449−4901	C			−1.401				72.2758	−49.0272		
S	J0456−5116	C		0.729±0.150	−1.328±0.876	0.79±0.14		0.109±0.041	74.1170	−51.2806		
S	J0509−5342	C		0.830±0.130	−0.884±0.055	0.98±0.12		0.351±0.047	77.3384	−53.7030	77.3392	−53.7036
S	J0528−5300	C							82.0213	−52.9963	82.0221	−52.9982
S	J0547−5345	C		0.956±0.217	−1.074±0.210	0.90±0.31		0.281±0.085	86.6556	−53.7593	86.6569	−53.7587
S	J0552−5709	C			−1.844				87.8927	−57.1448	87.8981	−57.1414
S	J0559−5249	C		0.616±0.149	−1.558±0.261	0.70±0.16		0.342±0.052	89.9314	−52.8291	89.9301	−52.8242
S	J0655−5234	C			−1.754				103.9762	−52.5669		
S	J2034−5936	C			−1.517				308.5394	−59.6055		
S	J2035−5251	C			−2.004				308.7987	−52.8536		
S	J2043−5035	C	f	1.196±0.118	−0.611±0.039	1.31±0.10	√	0.285±0.029	310.8234	−50.5921		
S	J2106−5844	C		0.878±0.198	−1.090±0.402	0.97±0.26		0.336±0.080	316.5191	−58.7417	316.5194	−58.7412
S	J2145−5644	C		0.867±0.192	−1.056±0.131	0.99±0.23		0.220±0.077	326.4666	−56.7490	326.5298	−56.7422
S	J2146−4632	C		0.831±0.196	−1.733±0.217	0.90±0.31		0.247±0.061	326.6458	−46.5482		
S	J2218−4519	C		0.716±0.233	−1.605±0.476	0.75±0.29		0.226±0.103	334.7462	−45.3167		
S	J2222−4834	C		0.808±0.135	−0.899±0.086	0.77±0.14		0.304±0.074	335.7120	−48.5769		
S	J2232−6000	C		1.002±0.118	−0.895±0.060	1.14±0.13		0.202±0.053	338.1415	−59.9981		
S	J2233−5339	C		0.925±0.234	−1.360±0.131	1.08±0.23		0.185±0.075	338.3194	−53.6545		
S	J2236−4555	C			−1.128				339.2173	−45.9306		
S	J2258−4044	C		0.700±0.133	−1.376±0.179	0.78±0.15		0.126±0.063	344.7037	−40.7381		
S	J2259−6057	C		0.875±0.104	−1.019±0.093	0.98±0.10		0.176±0.049	344.7543	−60.9607		
S	J2301−4023	C		0.636±0.111	−1.022±0.050	1.04±0.12		0.340±0.048	345.4714	−40.3872		
S	J2325−4111	C			−1.410				351.2980	−41.2009		
S	J2331−5051	C	f	1.211±0.134	−0.757±0.053	1.24±0.14	√	0.247±0.039	352.9637	−50.8650	352.9631	−50.8650
S	J2335−4544	C		0.659±0.236	−1.203±0.464	0.56±0.35		0.357±0.085	353.7841	−45.7397		
S	J2337−5942	C		0.845±0.199	−1.060±0.097	1.22±0.19		0.180±0.063	354.3537	−59.7055	354.3651	−59.7013
S	J2341−5119	C		0.970±0.163	−0.942±0.072	1.10±0.17		0.213±0.063	355.3018	−51.3290	355.3015	−51.3290
S	J2343−5411	C		1.062±0.172	−1.145±0.614	0.94±0.18		0.220±0.065	355.6915	−54.1850	355.6913	−54.1848
S	J2344−4242	C	f	1.344±0.169	−0.293±0.015	1.48±0.17	√	0.092±0.033	356.1834	−42.7202		
S	J2345−6406	C		0.681±0.131	−1.627±0.238	0.90±0.15		0.174±0.060	356.2466	−64.0974		
S	J2352−4657	C		0.888±0.163	−1.423±0.212	0.94±0.16		0.175±0.069	358.0676	−46.9596		
S	J2356−5056	C		1.053±0.169	−0.965±0.183	0.97±0.19		0.128±0.074	358.9472	−50.9273	358.9477	−50.9280
S	J2359−5009	C			−1.760				359.9294	−50.1698		
⋆	3C 186	C	af	0.939±0.046	−0.694±0.023	1.14±0.06	√	0.233±0.028	116.0728	37.8882		
⋆	Abell 3627	R		1.194±0.171	−1.798±0.220	1.34±0.18		0.376±0.016	243.6243	−60.8887		
⋆	CL J1415+3612	C	af	0.896±0.068	−0.703±0.036	1.05±0.09	√	0.166±0.029	213.7963	36.2010		
⋆	MS 1137.5+6625	C	a	1.061±0.092	−0.922±0.031	1.22±0.08		0.122±0.029	175.0943	66.1377	175.0924	66.1375